DISSERTATION

Electron Emission and Nanodefects due to Slow Ion Induced on Solid Surfaces

ausgeführt zum Zwecke der Erlangung des akademischen Grades eines

Doktors der technischen Wissenschaften

unter der Leitung von

a.o.Univ.-Prof. Dr. Friedrich Aumayr

E134

Institut für Allgemeine Physik

eingereicht an der Technischen Universtität Wien

Technisch-Naturwissenschaftliche Fakultät

von

Dipl.-Ing. Stefan Cernusca

9225643

Luis-Zuegg-Str. 10, 6020 Innsbruck

Wien, Juni 2003

Kurzfassung

In dieser Arbeit werden die Ergebnisse der Messungen der totalen Elektronenausbeute induziert durch den Beschuss mit verschiedenen einfach und mehrfach geladenen Ionensorten (H^+, H_2^+, H_3^+, D^+, D_2^+, D_3^+, N^+, Ar^+, Xe^+, C^{q+}, N^{q+} and O^{q+}) dargestellt. Als Targets wurden hoch orientierter pyrolytischer Graphit (HOPG) und auch ein Graphitziegel vom Tokamak Experiment TORE SUPRA in CEA-Cadarache/France verwendet. Bis zu diesen Messungen waren für diese Ionen-Target-Systeme noch keine Messdaten vorhanden. HOPG ist ein gut charakterisierbares Standardtarget in der Oberflächenphysik. Die Graphitziegel sind von technischem Interesse, da sie ein weit verbreitetes Wandmaterial für Kernfusionsexperimente sind. Diese Messungen erforschen den Einfluss der verschiedenen Targeteigenschaften, wie z.B. Fermienergie und Leitfähigkeit, auf die kinetische Elektronenemission. Dadurch wurde ein besseres Verständnis für die zugrundeliegenden Mechanismen, die zur Elektronenemission führen, erreicht. In weiterer Folge wurde der Einfluss einer erhöhten Elektronenemission auf die Potentialverteilung nahe der „ersten" Wand einer Fusionsanlage untersucht. Diese Verteilung beeinflusst die Intensität der Plasma-Wand-Wechselwirkung.

In dieser Arbeit werden auch Untersuchungen von Nanodefekten mittels eines Rastertunnel (STM) - bzw. Rasterkraftmikroskop (AFM) an LiF, Mica, SiO_2, Al_2O_3 und HOPG präsentiert, die durch den Beschuss mit langsamen (kinetische Energie < 1 keV) einfach und mehrfach geladenen Ionen entstanden sind. Diese Messungen erfolgten unter UHV-Bedingungen. Durch eine kombinierte AFM- und STM-Untersuchung kann gezeigt werden, dass die Ionen induzierten Defekte auf einem HOPG-Target auf Störungen in der Elektronenkonfiguration zurückzuführen sind, aber nicht zu sichtbaren topographischen Veränderungen an der Targetoberfläche führen. Andererseits zeigt sich, dass auf monokristallinen Isolatoren durch den Beschuss nm große topographische Defekte erzeugt werden. Für Al_2O_3 und HOPG kann man auch zeigen, dass die Defektgröße vom Ladungszustand der Projektile abhängt („potential sputtering"). Dieser Effekt könnte für die Nanostrukturierung- und Modifikation von Oberflächen von Interesse sein, da er ohne hohe kinetische Projektilenergie erreichbar ist.

Abstract

Within this work we have obtained experimental results for total electron emission from graphite and carbon-composite targets due to impact of various singly and multiply charged ions (H^+, H_2^+, H_3^+, D^+, D_2^+, D_3^+, N^+, Ar^+, Xe^+, C^{q+}, N^{q+} and O^{q+}). For most of the systems studied such data have not been available in the literature so far. Highly oriented pyrolytic graphite (HOPG) has been used as target surface as well as graphite tiles from the Tokamak experiment TORE SUPRA in CEA-Cadarache/France. While HOPG is a well-defined standard target in surface science the graphite tiles are of practical interest since they are widely used as plasma facing in magnetically confined fusion devices. The measurements allowed to study the influence of different target properties (like Fermi energy and conductivity) on electron transport and therefore on the kinetic electron emission. New insights into the underlying mechanisms for electron emission have been obtained. In addition we have investigated to what extend electron emission from first wall elements in fusion devices can influence the potential distribution in the plasma sheath and consequently the intensity of plasma wall interaction.

This work also presents systematic STM/AFM investigations on nanoscopic defect production on atomically clean surfaces of LiF, muscovite mica, SiO_2, Al_2O_3 and highly-oriented pyrolytic graphite (HOPG) after bombardment by slow (impact energy < 1 keV) singly and multiply charged ions under strict UHV conditions. Combined STM- and AFM studies show that on HOPG only "electronic" but no visible topographic defects are created by such ion bombardment. On the monocrystalline insulator surfaces well defined topographic features of typically nm extensions are produced ("potential sputtering"). For Al_2O_3 and HOPG a clear dependence of the defect size on the projectile ion charge is demonstrated. These results are discussed in view to possible new nanoscopic surface structuring and -modification methods for which the kinetic projectile energy plays a minor role only.

Contents

Motivation

The interaction of energetic ions (atoms) with surfaces leads to a variety of emission phenomena (emission of electrons, photons, atoms, ions, clusters, see fig. I.1) and results in pronounced modification of the surface and near surface regions (change in composition and structure, defect production, removal of atoms, etc.) [1]. The technological relevance of low energy ion - surface interactions in such diverse fields as surface analysis, implantation, sputter cleaning of surfaces, thin film deposition, etc. [2] has provided the stimulus for ongoing investigations into the responsible basic mechanisms.
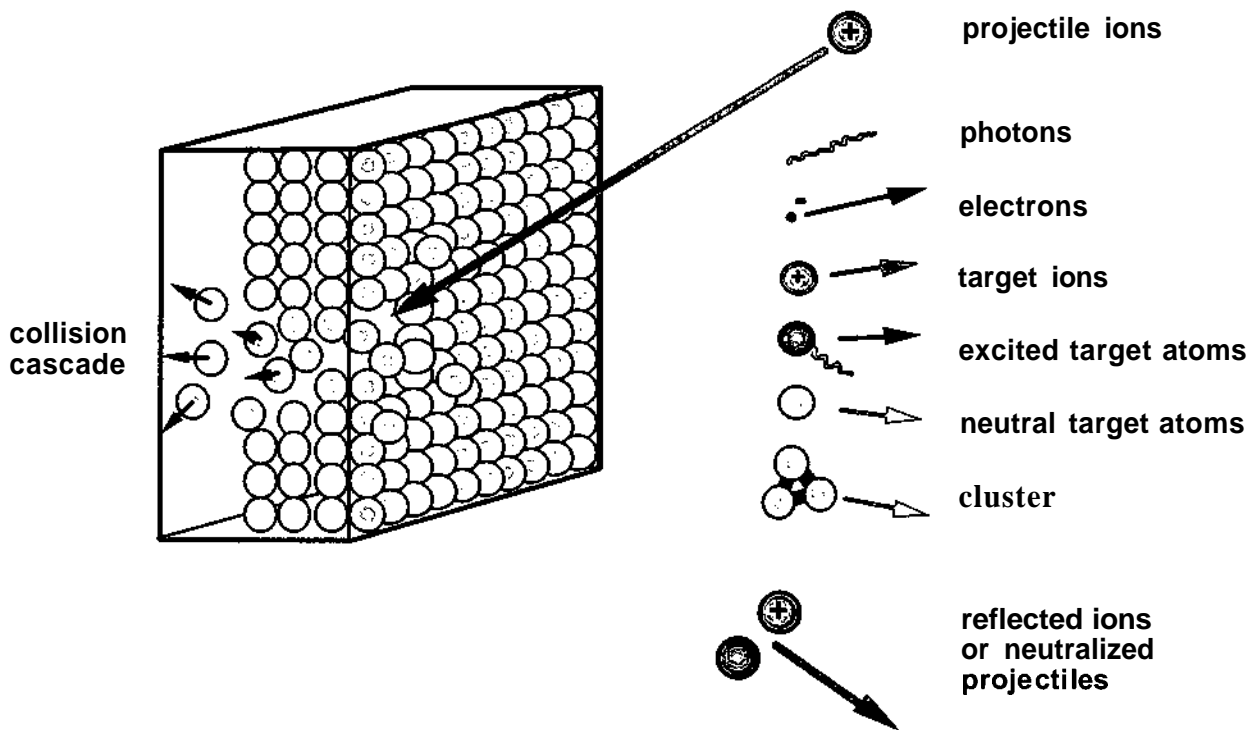
Fig. I.1: Ion impact on solid surfaces induces a variety of physical phenomena (c.f. text).

Electron emission from solid surfaces under ion impact is the basis of important technical applications and has therefore been studied for almost 100 years [3-5]. According to a simplified distinction ion-induced electron emission can be related either to the kinetic energy of the projectiles, termed kinetic emission (KE), or to their potential energy, e.g. the sum of ionization potentials to produce the respective ion: termed potential emission (PE), see also tab. I.1. PE arises already at the lowest impact velocities if the ion potential energy surpasses twice the surface work function, and for a given impact velocity it increases strongly with the ion charge [6]. KE arises irrespective of the projectile charge but only above some impact velocity threshold which is not well defined because of different possible contributions [7, 8].

In kinetic sputtering (termed - KS) usually the decelerated primary projectiles transfer (kinetic) energy and momentum to the target atoms, displacing them from their original position and eventually causing their emission into vacuum [9]. Singly charged ions with kinetic energies of typically some keV mainly interact by means of a few direct collisions with the target atoms (nuclear stopping) [10]. For faster ions and especially swift heavy ions (typ. MeV/amu) the electronic energy loss (electronic stopping) dominates [11, 12], leading to electronic excitation and ionization in a track of a few nm diameter. While the energy dissipation of the fast projectile is well understood, the conversion of electronic excitations into atomic motion of (eventually sputtered) surface atoms is still a matter of debate.

	E_{kin}: 0 - 150 keV $q = 0, 1, ...$	W_{pot}: 0 - 1000 eV $q = 1 - 28$
electron emission	KE	PE
sputtering	KS	PS

Tab. I.1: Ion impact on solid surfaces causes different physical phenomena, e.g. potential electron emission (PE), potential sputtering (PS), kinetic electron emission (KE) and kinetic sputtering (KS) depending on the ions charge state q and impact energy E_{kin} (c.f. text).

In addition to their kinetic energy, ions can also carry internal (= potential) energy, particularly if the ions carry a high charge. In a highly charged ion (HCI), potential energy will be stored according to its production where q electrons (q ... ion charge state) have to be removed from an originally neutral atom, and this potential energy becomes rather large for high values of q. Upon surface impact this potential energy is available for inducing various inelastic processes while the HCI will regain its q missing electrons to become again fully neutralized [13-17].

The HCI deposits its potential energy in a short time (typically about hundred femtoseconds) within a small area (typically less than one nm^2). This can lead to strong nonlinear excitation processes, exotic phenomena such as "hollow atom" formation (see fig. I.2) [13, 15, 17, 18] and eventually to the removal of atoms and ions from the target surface [19]. Since the energy for ejection of target atoms and ions results from the potential energy of the ion, this new form of sputtering has been termed "potential sputtering" (PS) [19-21].

image charge   "hollow atom"   potential energy
acceleration   formation & decay   deposition

Z^{q+}

e^- e^-

surface

e^-

q^-

resonant   ; electron   ! desorption +
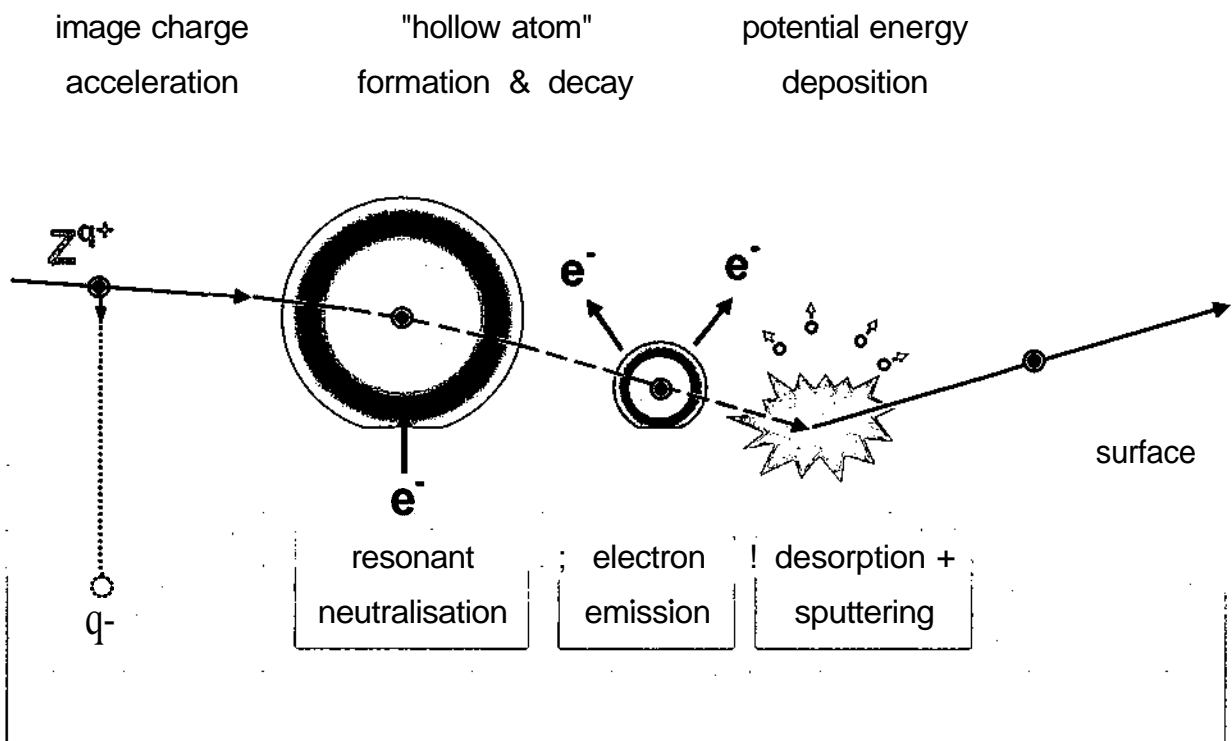neutralisation | emission | sputtering

Fig. I.2: Scenario for a multiply charged ion penetrating a solid surface.

In part I of this work some novel aspects of ion induced electron emission are investigated. There are well established theories to describe kinetic electron emission for medium and high impact energies [5], whereas for the very low ion velocity regime close to the threshold (projectile velocity v of serveral hundred eV/amu) the mechanisms of kinetic electron emission and their relative importance are not fully understood. In view to a better understanding of the respectively relevant mechanisms we have measured the mean number of electrons emitted per projectile ion (total electron yield y) from a graphite target surfaces with different crystal structures. In our studies we have used various projectile species with different charge states and impact energies.

Chapter I 1 will give an overview of the different mechanisms for kinetic electron and in chapter I 2 the used experimental methods will be presented. Experimental results for electron yield from graphite tiles and highly orientated pyrolytic graphite (HOPG) under impact of singly charged ions can be found in chapter I 3. The Molecular and isotopie effects for KE will be investigated in chapter I 4. The influence of electron emission on the sheath potential of fusion plasmas will be discussed in chapter I 5, where also results for multiply charged ion impact on graphite are presented. In chapter I 6 HOPG surfaces of different conductivities are studied.

In part II of this work a systematic STM/AFM investigations on nanoscopic defect production at atomically clean surfaces of SiO_2, Al_2O_3 and highly-oriented pyrolytic graphite (HOPG) after bombardment by slow (impact energy < 1 keV) singly and multiply charged ions under strict UHV conditions is presented.

Chapter II 1 will give an introduction to potential sputtering. The experimental setup is presented in chapter II 2 and in chapter II 3 and II 4 the results are discussed in view to possible new nanoscopic surface structuring and -modification methods for which the kinetic projectile energy plays a minor role only.

Some parts of the here presented work, have already been published in scientific journals or are awaiting publication, respectively:

S. Cernusca, A. Diem, HP. Winter, F. Aumayr, J. Lörincik, Z. Sroubek,
Kinetic electron emission from highly oriented pyrolytic graphite surfaces induced by singly charged ions.
Nuclear Instruments and Methods in Physics Research B 193 (2002) 616 - 620

J. Lörincik, Z. Sroubek, S. Cernusca, A. Diem, HP. Winter and F. Aumayr
Ion induced kinetic electron emission from highly oriented pyrolytic graphite by impact of H^+, C^+, N^+ and O^+.
Surface Science 504 (2002) 59 - 65

S. Cernusca, HP. Winter, F. Aumayr, R. Díez Muiño, J.I. Juaristi
Molecular projectile effects for kinetic electron emission from carbon- and metal surfaces bombarded by slow hydrogen ions
Nuclear Instruments and Methods in Physics Research B 203, 1 (2003)

S. Cernusca, HP. Winter, F. Aumayr, A. Qayyum, W. Schustereder, C. Mair, P. Scheier, and T.D. Märk
Edge Plasma relevant ion-surface collision processes
International Journal of Mass Spectrometry and Ion Processes 223, 21 (2003)

C. Gebeshuber, S. Cernusca, F. Aumayr, and HP. Winter,
AFM search for slow MCI-produced nanodefectson atomically clean monocrystalline insulator surfaces
Nuclear Instruments and Methods in Physics Research B 205, 751 (2003)

A. Qayyum, W. Schustereder, C. Mair, P. Scheier, T. D. Märk, S. Cernusca, HP. Winter, and F. Aumayr
Electron emission and molecular fragmentation during hydrogen and deuterium ion impact on carbon surfaces
Journal of Nuclear Materials 313 -316, 670 (2003)

I. C. Gebeshuber, S. Cernusca, F. Aumayr, and HP. Winter, (in print)
Nanoscopic surface modification by slow ion bombardment

PART I

Measurements of the Total Electron Yield from different Graphite Targets under Ion Impact

I.1 Introduction

Electron emission induced by ion impact on solid surfaces is a fundamental process in inelastic ion-surface collisions and of interest for various technical applications as, e.g., single particle counting and plasma-wall interaction (for recent reviews see, e.g., [4, 5, 13]). In a simple approach ion-induced electron emission can result from the kinetic (kinetic emission - KE) as well as the potential energy (potential emission - PE) of the projectile ions. KE requires a certain impact velocity threshold whereas PE only needs a minimum potential energy deposited upon impact, i.e. a total ion recombination energy surpassing twice the surface work function W_ϕ. There are several ways in which slow ions can excite electrons at the expense of their kinetic energy. The two most prominent mechanisms involve direct binary collisions with target electrons and electron promotion in quasi-molecular collisions of projectile ions with target atom cores. The latter process strongly depends on details of the electronic structure of projectile and target atoms. The situation is further complicated by the fact that the amount of electrons emitted not only depends on the primary electron excitation mechanism but also on other properties of the solid surface, e.g. the mean free path for low energy electrons inside the target bulk and their escape probability through the surface barrier [5].

In a series of recent studies on clean gold surfaces some of the contributions to the total electron yield could be disentangled. With very slow ions in higher charge states the domain of exclusive PE can be investigated [22, 23]. Coincidence measurements between emitted electrons and projectiles scattered under grazing angles from a mono crystalline surface can separate PE and KE contributions [24]. Exclusive KE mechanisms have been studied at the KE velocity threshold for various singly charged ions on polycrystalline Au [25].

To further clarify the role of target properties for the KE mechanisms and to test the recent theories [26, 27] for the ion-induced kinetic electron emission (KE) we have chosen a different target material, namely highly oriented pyrolytic graphite (HOPG). On the one hand graphite is very similar to gold: Both target materials are good conductors and the work function W_ϕ is almost the same (5.1 eV for gold and 5.0 eV for graphite). On the other hand, their Fermi energies E_F (approx. 7.6 eV for gold [28, 29] and 21.3 eV for graphite [30]) are quite different and this influence might therefore be investigated from a direct comparison of the two targets.

As the potential energy of the projectiles used in these investigations is relatively low (13.6 eV (H⁺), 11.3 eV (C⁺⁾, 14.5 eV (O⁺) and 13.6 eV (N⁺) , respectively) we assume that the electron emission is mainly due to the kinetic energy of the projectile. Lörincik et al. showed in ref [27], that at least three non-adiabatic one-electron KE models can be distinguished:

A) By the first one (electronic KE - eKE) the valence electrons of the solid become excited in the binary collisions with the projectile moving in an idealized Fermi electron gas and ejected into the vacuum [27]. This process is characterized by an impact velocity threshold $v_{th,A}$, below which no electron emission should be possible [31]:

$$v_{th,A} = \frac{1}{2} v_F \left(\sqrt{1 + \frac{W_\Phi}{E_F}} - 1 \right)$$

(1.1)

where v_F is the Fermi velocity of the target electrons (graphite - EF — 21,3 eV, $W_\phi = 5.0$ eV). According to eq. (1.1) this "classical" threshold for graphite is 1.5×10^5 m/s. This process yields a very narrow excitation spectrum which means that for the emission of several-tens-eV electrons into the vacuum much higher impact velocities than $v_{th,A}$ (by more than one order of magnitude) are required. Therefore for keV-impact energies only the lightest projectiles (H, He) may have sufficient impact velocity for this mechanism to be relevant.

B) If we assume that target valence electrons are partially localized or the particle does not move along a straight trajectory with a constant speed (i.e., the break-down of the idealized concept of plane-wave-like free electrons), a smearing-out of the threshold takes place and electrons may also be emitted for impact velocities below $v_{th,A}$. Several causes for the localization of the valence- band electrons have been proposed:

(1) the surface proximity [26],
(2) the atomic-like character of the d-band levels [32],
(3) the orthogonality of the valence-band-electron wave functions to the inner-shell-electron wave functions [33].

Only the model from [26] (the surface-assisted KE - sKE) provides analytical formulae which are convenient when comparing the theory with experimental data. It is a model based on a time-dependent perturbation of the projectile-target electronic system by a passing-by

projectile. It is assumed that the target valence-electron wave functions are semilocalized at the surface and decay exponentially into the vacuum. This decay is described by a parameter a, which is the inverse decay length at which the amplitude of the wave function decreases to 1/e. It is further assumed that the T-matrix of this process is also responsible for the electronic stopping and that the time-dependent transition between the value of the electronic stopping power in the bulk and the zero stopping power outside the target is also exponential and spatially localized at the surface region. These assumptions lead to the suggestion of a proper time-dependent T-matrix which enabled analytical solution of the problem.

In [26] an expression for the KE yield has been derived. It has the form

$$\gamma_B = 2\xi\rho^2 V^2 \left\{ \ln\left(e^{-\frac{\pi W_\Phi}{2\alpha v}} + 1 \right) - \pi^{1/2} \left(\frac{\pi W_\Phi}{2\alpha v} \right)^{1/2} I\left[\left(\frac{\pi W_\Phi}{2\alpha v} \right)^{1/2} \right] \right\}$$ (1.2)

where

$$I(x) = 2\pi^{-1/2} \int_x^{+\infty} \frac{dy}{e^{y^2} + 1}$$ (1.3)

p is the electronic density of states at the Fermi energy, V is the scattering matrix element, ξ is a correction factor to the value $\rho^2 V^2$ parameter and a is the inverse decay length of the valence-electron wave function at the surface. The product $\rho^2 V^2$ is proportional to the electronic stopping power dE/dx according to [34]:

$$\frac{dE}{dx} = \frac{\pi}{3} \rho^2 V^2 k_F^2 v$$ (1.4)

where k_F is the Fermi vector. For small velocities, when $e^{\pi W_\Phi/(2\alpha v)} \gg 1$, $I(x) = erfc(x)$ and eq. (1.2) can be approximated by an expression

$$\gamma_B = 2\xi\rho^2 V^2 \left\{ e^{-\frac{\pi W_\Phi}{2\alpha v}} - \pi^{1/2} \left(\frac{\pi W_\Phi}{2\alpha v} \right)^{1/2} erfc\left[\left(\frac{\pi W_\Phi}{2\alpha v} \right)^{1/2} \right] \right\}$$ (1.5)

where $erfc(x)$ is the complementary error function.

C) Besides valence electrons also localized semicore or core electrons can be perturbed by the moving projectile in a close-distance binary collision (promotion KE - pKE). Such a collision can be looked upon as a temporary creation of a quasimolecule, in which some electronic levels may be sufficiently strongly promoted to higher orbital energies and thus give rise to electron emission in subsequent de-excitation steps (so called Fano-Lichten process [35]). Two possible de-excitation processes can be distinguished. In the first one the collision partners are separated in an excited state with inner-shell vacancies. Such species can then be de-excited by the Auger process and give rise to atomic-like features in the electron emission spectra. This process can be characterized as an electron promotion followed by Auger emission (EPAE). In the second case the electrons are promoted/excited sufficiently high above the Fermi level and then directly emitted into the vacuum. This process has been labelled as the electron promotion followed by molecular autoionization (EPMA). These process is specific to the types of collision partners and is characterized by the existence of a "critical" internuclear collisional distance r_c and the corresponding critical kinetic energy. If the projectile kinetic energy is larger than E_c the electron emission by this promotional mechanism is possible, i.e., an existence of a threshold energy $E_{th,C}$ is assumed. This threshold energy $E_{th,C}$ can be experimentally determined, and it can be theoretically estimated from the analysis of the respective molecular orbital (MO) correlation diagrams.

However, our studies on electron emission from graphite are not only motivated by basic interest, but have also been conducted for some practical applications. Graphite tiles or carbon-coated structures are largely used as wall- or divertor materials in magnetically confined fusion devices. Laboratory work on plasma-wall-interaction has so far mainly focused on obtaining physical and chemical sputtering yields for such materials. Much less is known on electron emission despite the fact that this largely influences the potential distribution in the plasma sheath [36, 37] and, consequently, the intensity of the plasma-wall-interaction [38]. The understanding and control of plasma-surface-interaction (PSI) is not only of great importance for the plasma processing industry, but also rather critical for the future success of fusion energy development [39]. While in early fusion devices the energy content was largely insufficient to destroy the plasma-facing materials, it has nowadays reached such high levels that divertor design including appropriate material selection has become very important for next-step fusion machines (in particular ITER-FEAT). Interaction with the wall material largely influences the performance of magnetically confined plasmas. The use of low Z materials such as carbon, boron and beryllium has been a great success in the present large tokamaks [40]. In ITER design, graphite based low Z material is recommended for divertor

plates and first wall protection for the initial operation phase in order to minimize the risk of plasma contamination.

The available data bases on plasma-surface interaction (PSI) mainly include data on physical and chemical sputtering/erosion, material deposition and hydrogen/deuterium recycling. Much less reliable data are known for electron emission from wall materials under impact of energetic ions, atoms or electrons [41]. However, electron emission can play an important role in PSI by influencing the boundary plasma (e.g. via the sheath potential) and the intensity of plasma wall interaction accordingly. Basically, a large yield of emitted electrons is expected to reduce the sheath potential. This in turn reduces the impact energy of ions and consequently the ion flux to the surface and the related sputtering yield.

Recent studies in the field of thermonuclear fusion based on the magnetic confinement of high temperature plasma have demonstrated that the conditions at the plasma periphery („plasma edge") play an important role for achieving, sustaining and controlling the thermonuclear fusion plasma [42, 43]. In order to understand and elucidate the role of the radiative and collisional processes in this plasma edge region (in particular their (i) influence on the plasma properties and dynamics and their (ii) use for controlling the plasma conditions), it is essential to have available a detailed and quantitative knowledge on (i) these elementary processes in the gas phase [43] (such as cross sections, reaction rate coefficients etc.) and on (ii) the interaction of the gas phase particles with the plasma walls [42]. These data are necessary as input for edge plasma modeling and various diagnostic techniques.

In view of the lack of available data, an important objective of this work was to present measured data for fusion-relevant ion species (e.g. H_n^+, n = 1 - 3) in the eV to keV impact energy region typical for fusion edge plasma conditions. As a fusions relevant target surfaces, graphite tiles from the Tokamak experiment TORE SUPRA in CEA-Cadarache/France have been used. Implications of the experimental results for plasma edge modeling are also discussed.

I.2 Experimental Setup

I.2.1   Determination of the total electron emission yields via current measurements

Total electron yields for impact of slow singly and multiply charged ions on a clean graphite surface have been precisely determined via current measurements for incident ions and emitted electrons.

There are different ways to determine the total electron yield y, i.e. the mean number of electrons emitted per projectile ion from a target surface into the $2 \times \pi$ hemisphere. Since in the impact energy of present interest only electron yields $\gamma \approx 1$ are to be expected (cf. discussion of relevant emission mechanisms below), the electron number statistics technique developed by our group [7, 8, 44, 45] is not well suited, considering the dominant probability for the emission of no electrons. Total electron yields y were therefore determined by means of current measurements for impinging ions and emitted electrons (cf. fig. I.2.1.1), as described in detail in ref. [46]. We used different graphite targets, like highly orientated pyrolytic graphite (HOPG, see chap. I 2.3) and graphite tiles from the Tokamak experiment TORE SUPRA in CEA-Cadarache/France (see chap. I 2.4). The target is surrounded by a highly transparent cage that can be biased by ± 50 V with respect to the target potential, and a shielding cylinder at target potential. When applying the positive bias to the cage with respect to the target, all emitted electrons are removed from the target, while no electrons with up to 50eV ejection energy will be able to leave the target if the negative bias is applied to the cage, as has been checked by ray trace calculations using the MACSIMION program.

For a positive cage bias of +50 V, the total current I_+ which is measured at the target consists of two components, the current of incoming projectile ions I_{ion} and the current of emitted electrons I_e (fig. I.2.1.1):

$$I_+ = I_{ion} + I_e = \gamma \times \frac{I_{ion}}{q} \qquad (2.1)$$

A negative bias voltage leads to a target current I_- being equal to the incident ion current

$$I_- = I_{Ion} \tag{2.2}$$

Therefore, the total electron yield can be derived from

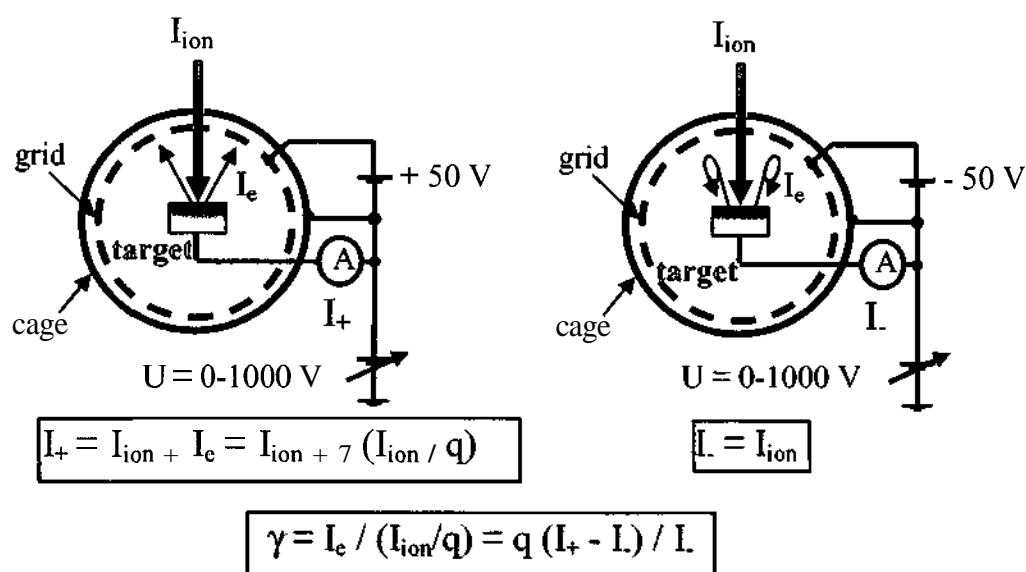$$\gamma = \frac{I_e / q}{I_{ion}} = q\,\frac{I_+ - I_-}{I_-} \tag{2.3}$$

Fig. I.2.1.1: Determination of total electron yields by measuring the currents of incoming ions and emitted electrons. For a positive cage bias of +50 V, the total current I_+ which is measured at the target consists of two components, the current of incoming projectile ions I_{ion} and the current of emitted electrons I_e. A negative bias voltage leads to a target current L being equal to the incident ion current. Therefore, the total electron yield can be derived from I_+ and I_-.
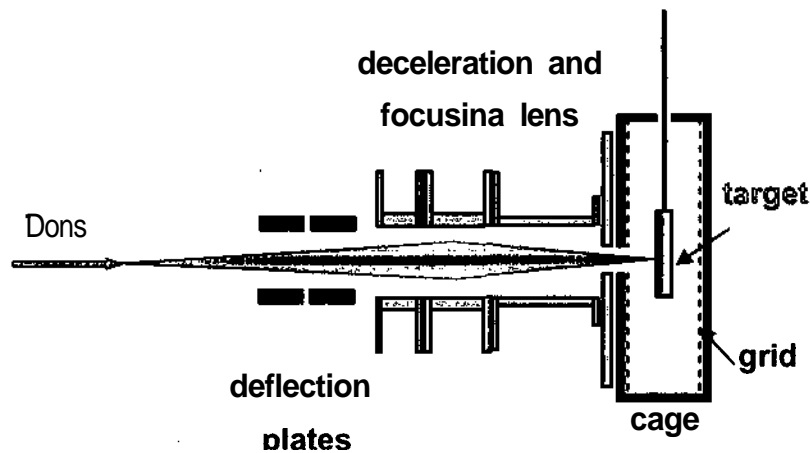
Fig. I.2.1.2: To obtain impact energies typical for the plasma edge (from several eV up to several keV), the ions are decelerated in front of the target by means of a suitable deceleration and focusing lens.

Although quite simple in principle, this method for determining y has some difficulties [5]. Measurements have to be taken consecutively which may be problematic if the primary ion current is not very stable. Moreover, in reality also other currents than I_{ion} and I_e will be present and influence the resulting y, as for example, sputtered secondary ions of both positive and negative charge, reflected ions, secondary electrons from surrounding walls due to impinging electrons, reflected ions or sputtered particles and stray electrons from ion-beam defining slits. By using a highly transparent cage instead of a solid wall, some of these problems can be avoided or at least strongly suppressed. Reflected neutrals will very likely pass the cage and hit the outer shielding cylinder which is at target potential. Electrons produced there will be prevented from reaching the target for both polarities of cage bias voltage, and the same holds for stray electrons from ion beam apertures (fig. I.2.1.1).

In order to obtain sufficiently reproducible results the target was kept in UHV and sputter cleaned at regular intervals. Sufficient cleanliness of the target surface and the reliability of our whole measuring technique have been assured by comparing results obtained for electron emission due to Ar^+ impact on C with earlier data [47]. Generally, the systematic error of y are estimated to about 10%. However, especially for very low electron yields, the statistical error can become much larger due to the subtraction of two almost equal currents (cf. eq. (2.3)).

Typical raw data are shown in fig. I.2.1.3. Data were obtained for normal ion incidence only.
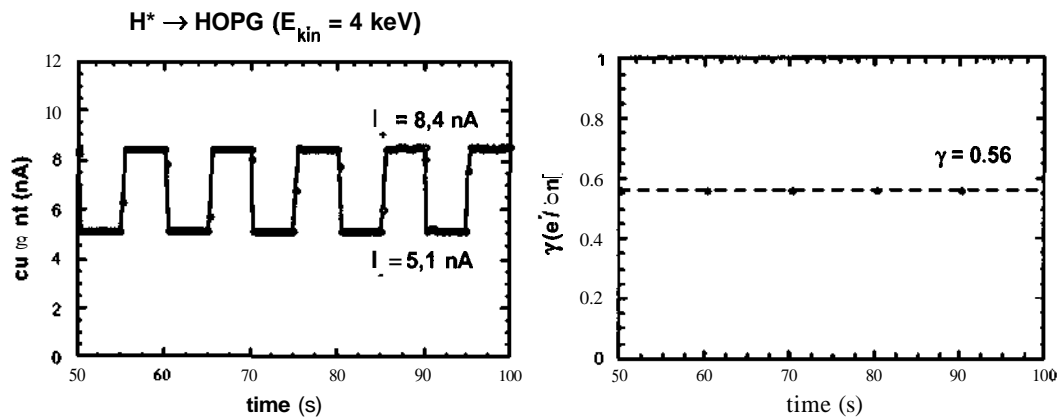
H* → HOPG (E_{kin} = 4 keV)

I_+ = 8,4 nA

I_- = 5,1 nA

γ = 0.56

Fig. I.2.1.3: Raw data as obtained for impact of H^+ on a graphite (HOPG) target.

As projectiles for our studies we have used singly charged ions and kinetic energies characteristic for typical edge plasmas, namely H^+, H_2^+, H_3^+, C^+, N^+ and O^+ and sometimes also multiply charged ions, e.g. C^{2+}, C^{4+}, N^{2+}, O^{2+}. These ions are produced in our 5 GHz ECR ions source [44] (see chap. I 2.2), extracted and accelerated with a few keV, formed to a beam with a magnetic quadrupol doublett, mass-to-charge separated in a 60° sector magnet and directed onto a suitable carbon target situated in an UHV chamber. To obtain impact energies typical for the plasma edge (from several eV up to several keV), the ions are decelerated in front of the target by means of a suitable deceleration and focusing lens (fig. I.2.1.2).

The targets were prepared by cleaving the surface with an adhesive tape just before the targets are introduced into vacuum. Before taking data, the targets were sputter-cleaned by impact of 5 keV Ar^{2+} ions. All investigations were carried out under ultra-high-vacuum (UHV) conditions (typ. 10^{-10} mbar, fig. I.2.1.4). Carbon surfaces inside a fusion device are supposed to be dynamically clean due to heavy bombardment by plasma particles.
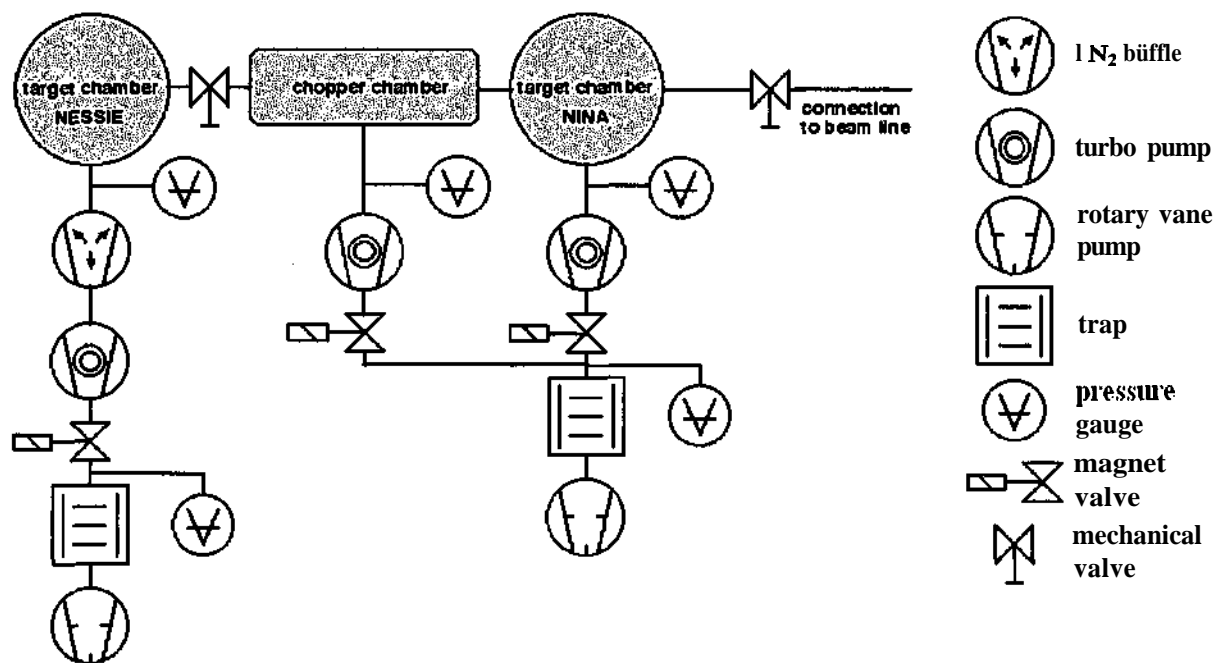
Fig. I.2.1.4: Pumping schema for the beam line of the experiment.

I.2.2   Ion Source

The ions are produced in our 5 GHz ECR ions source, which is capable of producing multiply charged ions [48].

A schematic drawing of the ECR ion source is given in fig. I.2.2.1. The confinement of the plasma is realised by means of a variable axial magnetic mirror field (up to 0.5T) and a radial permanent hexapole field (NdFeB) [49]. A biased disk serves as electron emitter, which enhances the fraction of higher charge states. A microwave power of up to 1 kW is delivered from a 5 GHz klystron driven by a tuneable microwave oscillator.

The ion source was developed for producing multiply charged ions from gas phase atoms or molecules. High purity gases in compressed gas bottles can be mounted on the gas inlet whose gas flux is controlled by an automatic valve. Depending on the desired charge state the gas pressure of in the plasma vessel can be varied from $2 \cdot 10^{-6}$-$5 \cdot 10^{-5}$ mbar.
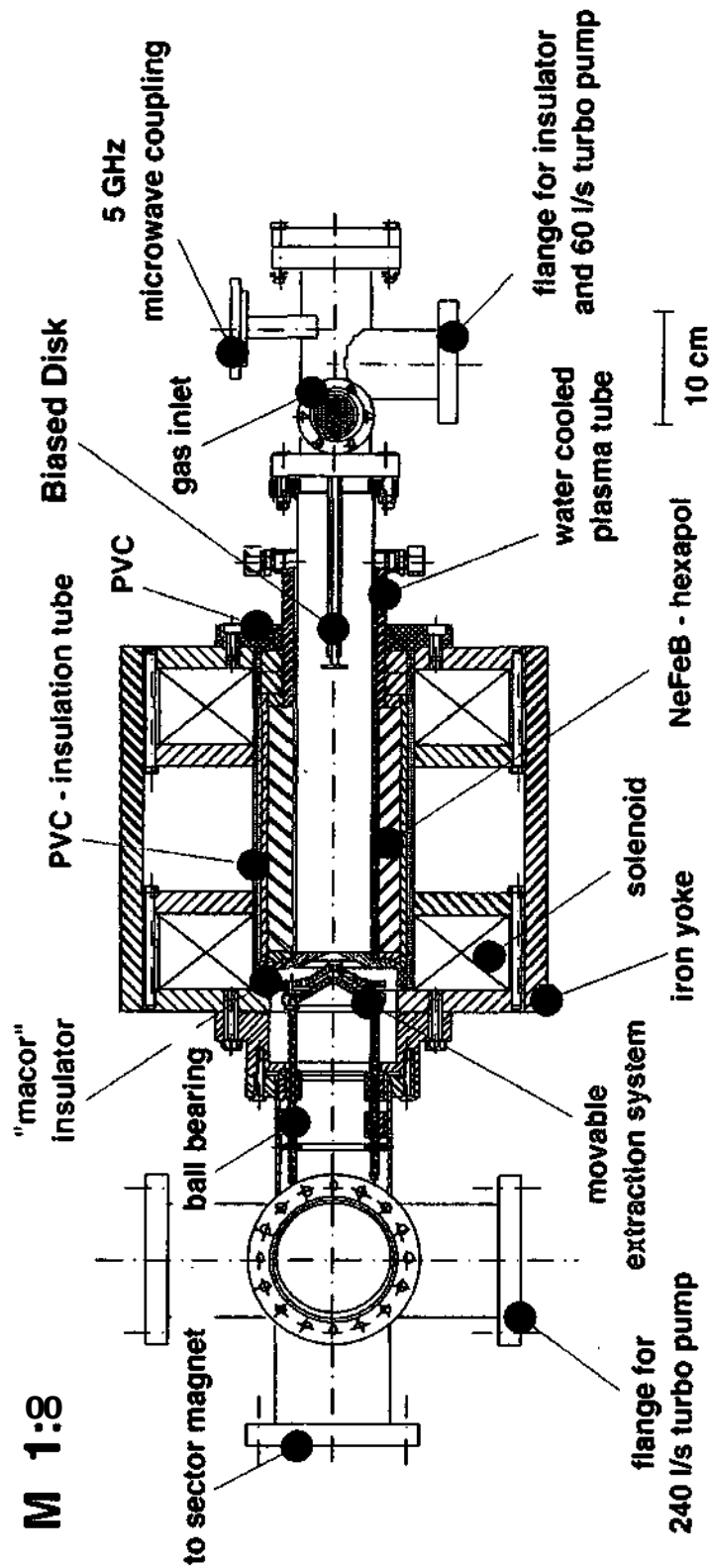
Fig. 1.2.2.1: Schematic drawing of the ECR ion source BERTA. The confinement of the plasma is realised by means of a variable axial magnetic mirror field (up to 0.5 T) and a radial permanent hexapole field (NdFeB).

The ion source insulation allows extraction voltages up to 12 kV. Formation of the extracted ion beam is achieved by an accel-decel configuration and a magnetic quadrupol doublett. The polarity and current through the sector magnet directs the ion beam to the experimental chamber and determines the m/q (mass/charge state) ratio of the selected ions. The potential scheme of the beam line is given in fig. I.2.2.2.

Fig. I.2.2.3 shows schematically the beam line arrangement at the AUGUSTIN Laboratory in Vienna.
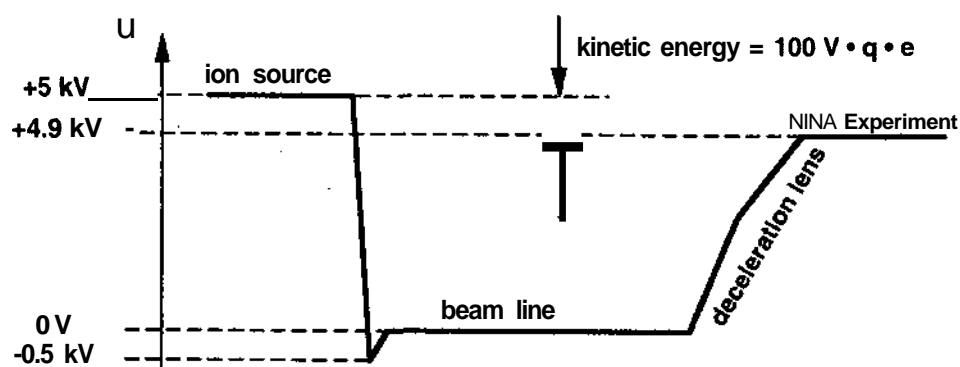

Fig. I.2.2.2: Typical voltage distribution along the beam line at TU Wien.
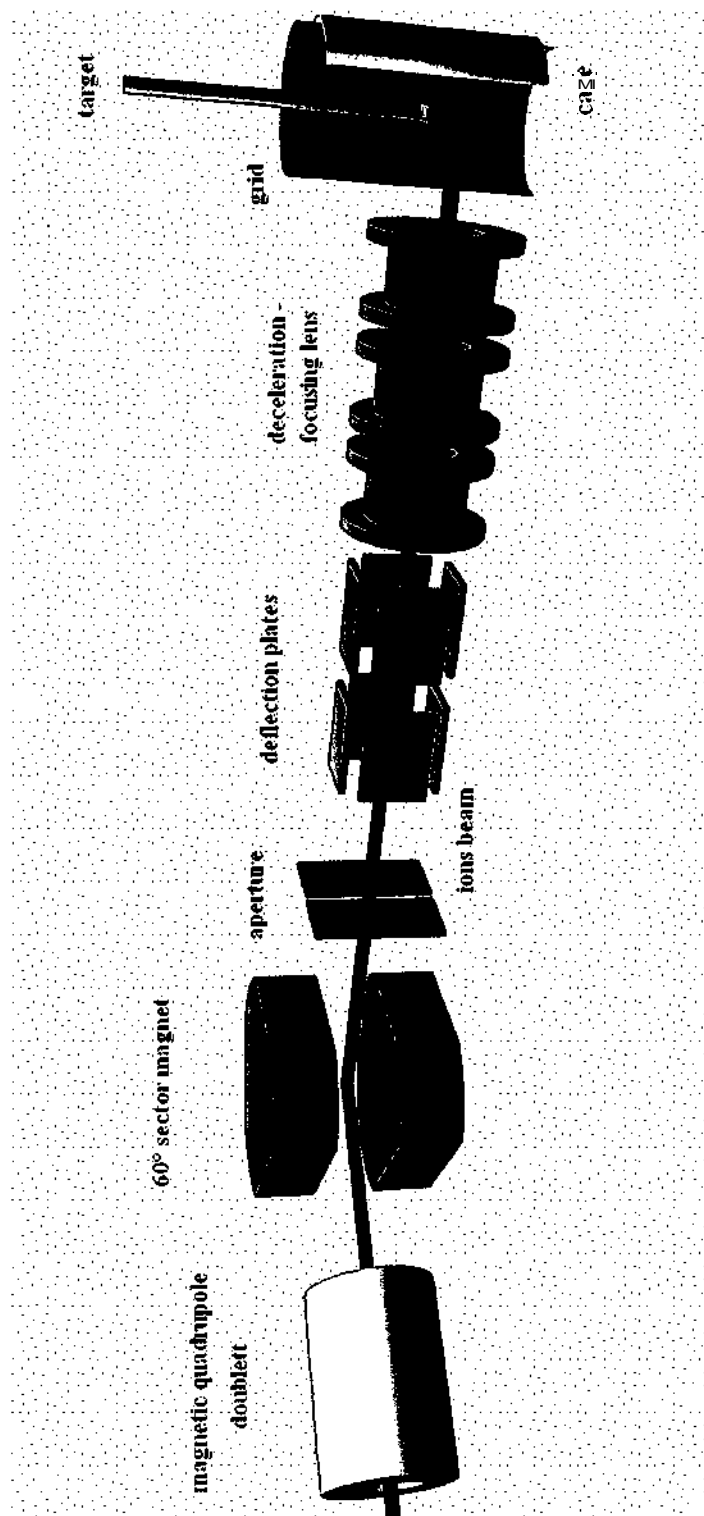
Fig. I.2.2.3: Beam line arrangement at TU-Wien. The ions are produced in our 5 GHz ECR ions source [44], extracted and accelerated with a few keV, formed to a beam with a magnetic quadrupol doublett, mass-to-charge separated in a 60° sector magnet and directed onto a suitable carbon target situated in an UHV chamber.

Fig. I.2.2.4 shows a typical ion mass spectrum with Ar used as the ion source gas. The mass spectrum was obtained by varying the sector magnet current with a Lab-View program and measuring the ion current in the faraday cup shown in fig. I.2.2.3.
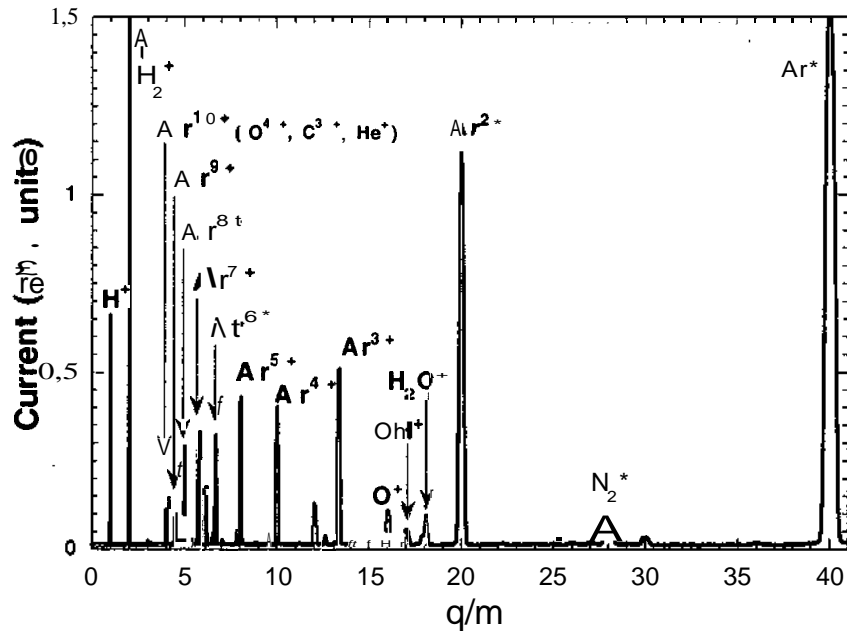

Fig. I.2.2.4: Typical mass spectrum of ions extracted from the 5 GHz ECR ion source BERTA.

I.2.3   Highly-Oriented Pyrolytic Graphite (HOPG)

Chemically, graphite is made up of carbon atoms which are arranged in polynuclear aromatic, hexagonal, ring arrays. Hexagonal arrays are oriented parallel to the "A" crystallographic axes. These arrays form sheets which are stacked parallel to the "C" crystallographic axis [50].

Carbon atoms in the graphite structure are in the sp^2 hybridized state. The sp^2 state is, by convention, illustrated showing carbon with two single bonds and one double bond to adjacent carbon atoms. This convention works well to keep track of the general position of electrons but does not illustrate the true anisotropic bonding nature of carbon in the graphite structure.
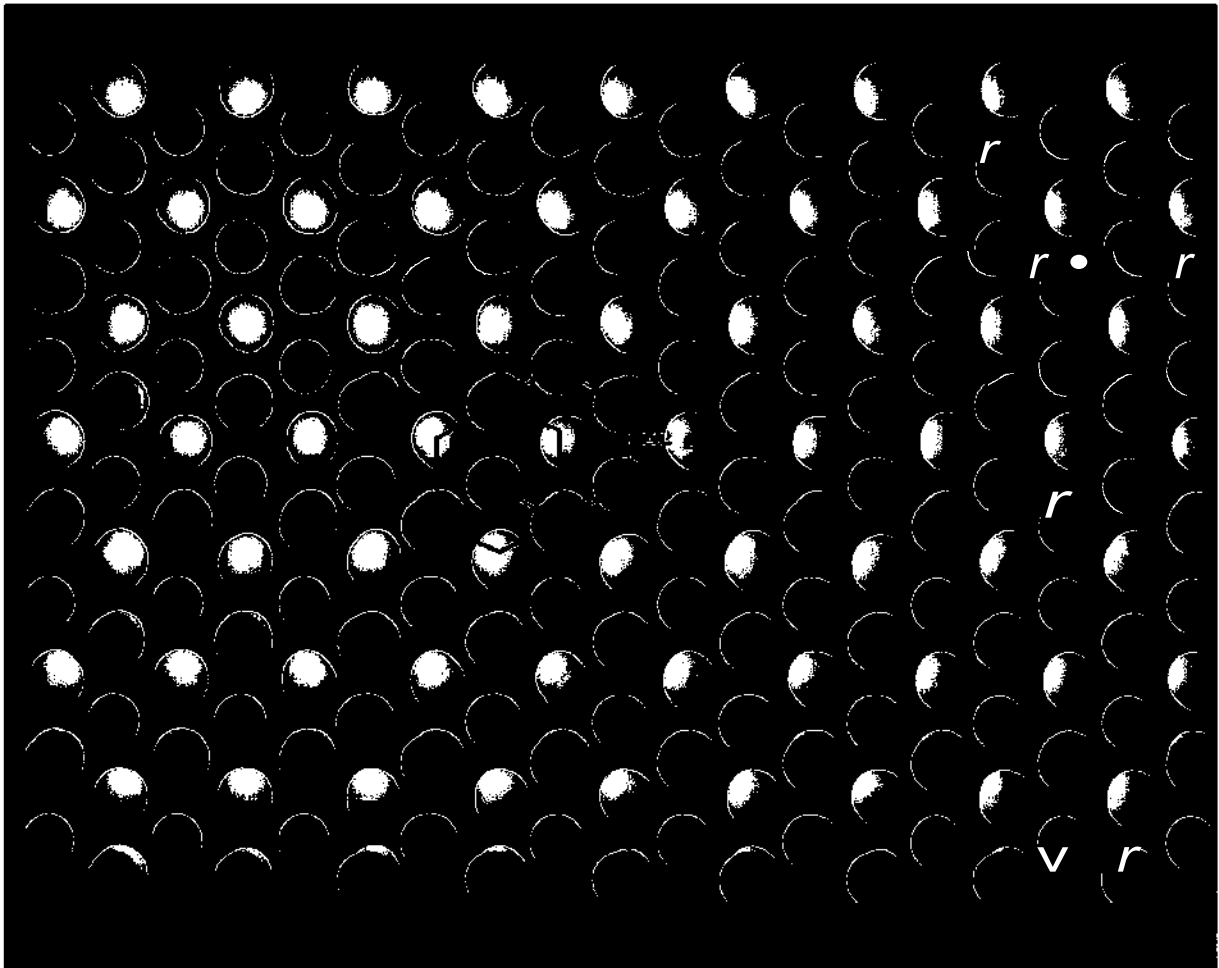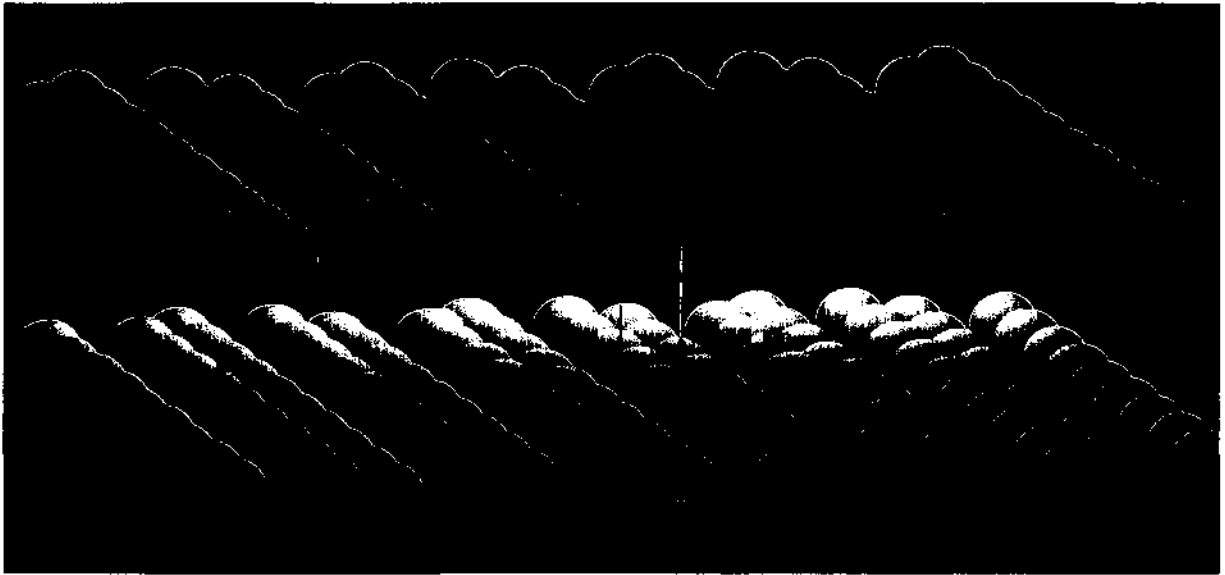

Fig. I.2.3.1: The σ bond length for carbon atoms is 142 pm

Fig. I.2.3.2: The π bond length for carbon atoms is 335 pm

In reality carbon-carbon bonds in the sp^2 state contain two distinct types of bonding orbitals. One, the cr bond, represents a strong "carbon to carbon", primary, covalent, bond. The cr bond length for carbon atoms is 142 pm (fig. I.2.3.1). Each carbon in the graphite structure contains three σ bonds, one to each of three adjacent carbon atoms. The second, the *n* bond, is a "weak" secondary, electrical field-type bond (in the "double bond" convention, the *n* bond is represented by one leg of the double bond). Each carbon atom contains one π-bond-electron which is "coupled" to other *n* electrons in a different layer. The *n* bond length for carbon atoms is 335 pm (fig. 1.2.3.2).

The high degree of anisotropy (directional properties) seen in graphite is the result of two types of bonding, primary covalent-σ and secondary-π, each acting in a different crystallographic direction (fig. I.2.3.3)
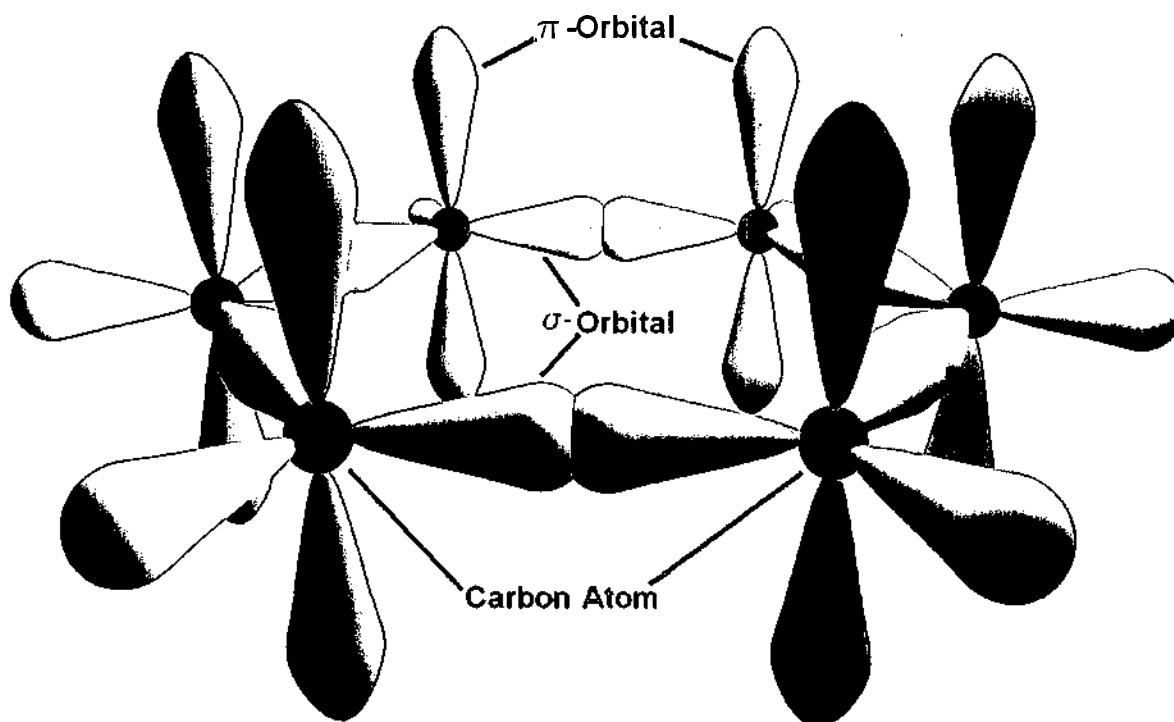
Fig. I 2.3.3: The high degree of anisotropy (directional properties) seen in graphite is the result of two types of bonding, primary covalent-σ and secondary-π, each acting in a different crystallographic direction

The HOPG target used in our experiments (tectra [51], size: 12x12x8 mm) consists of well defined layered carbon sheets. Both, its thermal and its electrical conductivity (see tab. 2.1) are considerably higher in a direction parallel to the graphite layers (so called "HC-HOPG" side) than in the perpendicular direction (so called "LC-HOPG" side) [51, 52]. In our measurements we compare total KE yields for HC-HOPG and LC-HOPG orientation of the HOPG target.

HOPG is a unique form of graphite manufactured by decomposition of a hydrocarbon gas at very high temperature in a vacuum furnace. The result is an ultra-pure product which is close to this theoretical maximum density and extremely anisotropic. This anisotropy results from the layered structure as indicated in fig. I.2.3.4. As an example, HOPG exhibits a thermal

conductivity close to the best conductors in the "AB" plane and lower than alumina brick in the "C" direction. Mechanical, thermal, and electrical properties are generally far superior to conventional graphite. Typical properties are listed in tab. 2.1.

C = 8mm

A = 12 mm

B = 12 mm
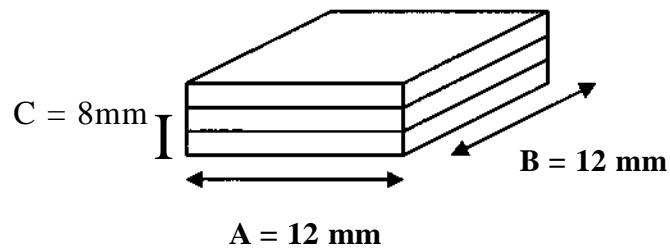
Fig. I.2.3.4: HOPG exhibits a thermal conductivity consistent with the best conductors in the "AB" plane and lower than alumina brick in the "C" direction.

Spacing of Planes	-	3.355 - 3.359Å
Density	-	2255 - 2265 kg/m^3
Thermal Conductivity	Parallel (AB)	1600 – 2000 Watt/m/K
	Perpendicular (C)	ca. 80 Watt/m/K
Electrical Resistivity	Parallel (AB)	3.5 - 4.5 x 10^{-7} Ohm/m
	Perpendicular (C)	1.5 – 2.5 x 10^{-4} Ohm/m

Table 2.1: HOPG - Physical Characteristics (at 300K) [51].

I.2.4   Carbon compound Tile

For our experiments we have also received carbon tiles from Association EURATOM −
CEA/Cadarache which were used there as limiter material in TORE Supra (fig. I.2.4.1).
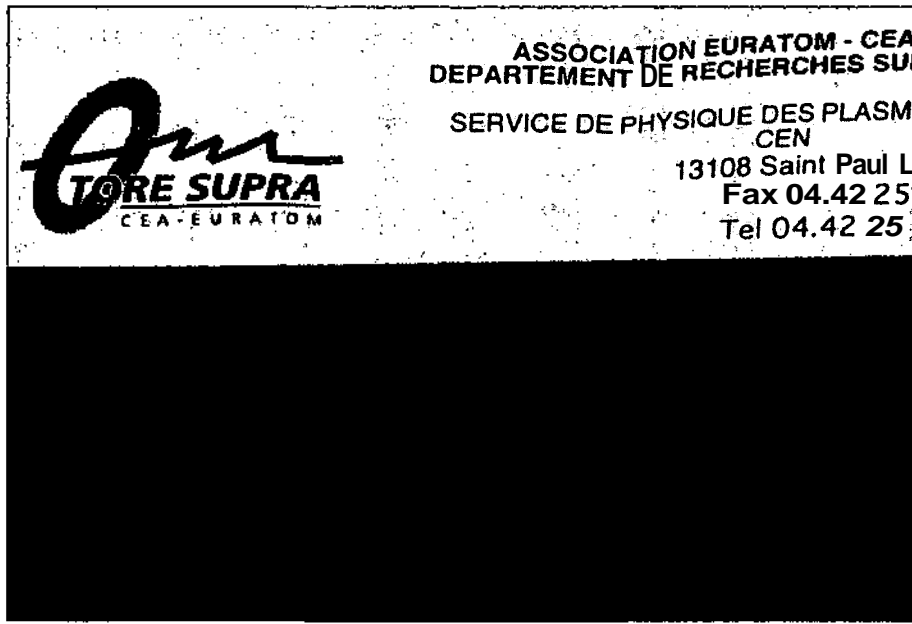

Fig. I.2.4.1: *Carbon tiles from TORE SUPRA have been used as a target material together
with HOPG.*

The surface orientations of these carbon compound tiles exhibit different thermal conductivity
(two high and one low thermal conductivity sides. Since the electron transport in a conductor
is connected to its thermal conductivity, some influence of thermal conductivity on the total
electron yield can be expected. Consequently, we have investigated electron emission from
the high (HC1 und HC2) and low (LC) thermal conductivity sides separately (fig. I.2.4.2).
Results have been compared to those for a highly oriented pyrolytic graphite (HOPG) sample,
a standard material in surface science (see I 2.3).
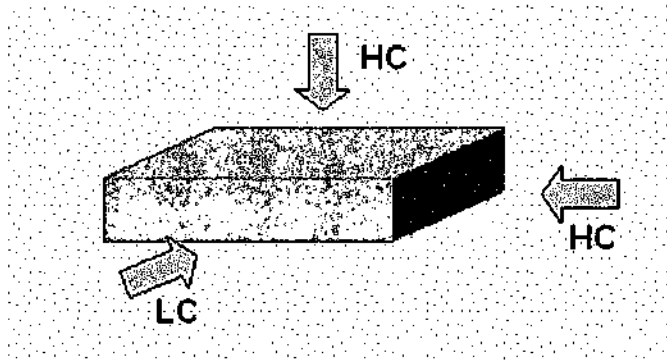
Carbon Tile:

High thermal conductivity:

HC: 230 W/m/K

Low thermal conductivity:

LC: 150 W/m/K

Fig. I.2.4.2: Carbon tiles from TORE SUPRA (which exhibit surface orientations with different thermal conductivity) have been used as a target material together with HOPG.

I.3   Electron Yield from Graphite Tiles and HOPG under Impact of Singly Charged Ions

Abstract

Total electron yields from HOPG have been measured for perpendicular impact of H^+, H_2^+, H_3^+, C^+, N^+, and O^+ projectile ions with kinetic energies from a few hundred eV up to 10 keV. The kinetic energies of the projectiles have been varied from near threshold up to 10 keV. By comparing the results to similar data obtained for a polycrystalline Au surface the role of different target properties for kinetic electron emission can be analysed. The data are interpreted within the models for the kinetic electron emission based on a non-adiabatic perturbation of the valence band electrons by the moving particle. The microscopical parameters describing the electronic excitation processes for the studied systems change in a consistent way when changing the target from HOPG to gold.

I.3.1 Experimental Results

Total electron yields from atomically clean graphite have been measured via current measurements (see chap. I 2.1) for normal impact of H^+, H_2^+, H_3^+, C^+, N^+, and O^+ ions ($E \leq 10\,keV$) on carbon tiles from Association EURATOM - CEA/Cadarache which were used there as limiter material in TORE Supra (see chap. I 2.4). Comparable measurements have also been performed for a clean highly-oriented pyrolytic graphite (HOPG) surface. The kinetic energies of the projectiles have been varied from near threshold up to 10 keV. By comparing the results to similar data obtained for a polycrystalline Au surface the role of different target properties for kinetic electron emission can be analysed. Similarities but also differences between both sets of data can be attributed to electronic properties of the target surfaces.

Fig. I.3.1.1 -. I.3.1.6 show measured total electron yields y induced by impact of H^+, H_2^+, H_3^+, C^+, N^+, and O^+ ions on the different carbon surfaces (C_L and CH denote results for the low - and high conductivity sides of the carbon tiles, HOPG to the highly oriented pyrolytic graphite sample, the layer orientation was normal to the incident beam). As a general trend, about 20% less electrons are emitted from the high conductivity side of the carbon tiles as compared to the low conductivity side (both high conductivity sides denoted as C_{H1} and *Cm* yield identical results within our error limits, as shown for the case of H_2^+ impact in fig. I.3.1.2), whereas results for HOPG are generally situated between the results for CL and C_H. For all projectile species electron emission starts around an ion impact velocity threshold of $10^5\,m/s$, corresponding to an impact energy (per atomic mass unit) of 50 V/amu.

Only for the hydrogen ions data can be compared to literature results. Our data are in very good agreement with measurements performed on bulk carbon samples by Large and Whitlock [53] and Cawthron et al. [47], and somewhat lower than data obtained on self supporting carbon foils [54]. To our knowledge no data for the other systems are available so far.

Electron yields as measured for the same projectile ions on clean polycrystalline gold [55] are shown in figs. 3.1.8 and 3.1.9 compared to the HOPG results. At projectile velocities below approx. 8×10^5 m/s the yields decrease linearly with the projectile velocity. If one extrapolates this trend to zero yield the resulting intersection with the velocity-axis appears at around 1×10^5 m/s in the case of our carbon target, which is considerably lower than the value obtained for Au (3.5×10^5 m/s) [55].

For discussion of our results we will consider the different mechanisms for electron emission and therefore concentrate on KE only since PE due to Auger neutralization [56, 57] can be neglected for the here applied singly charged ion species. In conducting targets the most prominent KE mechanism (at least for sufficiently fast projectiles) is momentum transfer in collisions of the projectile with quasi-free metal electrons („eKE process", see chapter I 1) [5]. In such collisions, however, quasi-free electrons from the Fermi gas can only be ejected into vacuum above the so-called "classical threshold" impact velocity $v_{th,A}$ which depends on the respective work function W_ϕ, and also on the Fermi velocity v_F (Fermi energy E_F) of the electrons in the solid [4, 5, 7, 31, 58] according to equation (1.1) in chapter I 1.

Fig. 3.1.1: Total electron yields vs. impact velocity v for impact ofH⁺ions on different carbon tile surfaces as well as HOPG (see text)[59].

Fig. I.3.1.2: Total electron yields vs. impact velocity v for impact of H_2^+ ions on different carbon tile surfaces as well as HOPG (see text)[59].

Fig. I.3.1.3: Total electron yields vs. impact v elocity v for impact of H_3^+ ions on different carbon tile surfaces as well as HOPG (see text) [59].
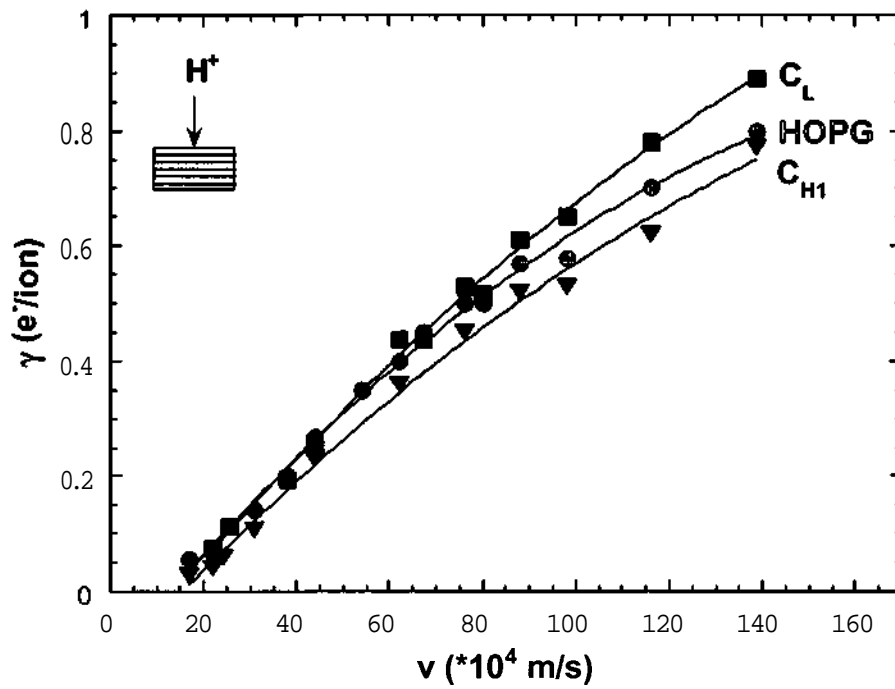

Fig. I.3.1.4: Total electron yields vs. impact velocity v for impact of C^+ ions on different carbon tile surfaces as well as HOPG (see text) [59].

Fig. I.3.1.5: Total electron yields vs. impact velocity v for impact of N⁺ ions on different carbon tile surfaces as well as HOPG (see text) [59].
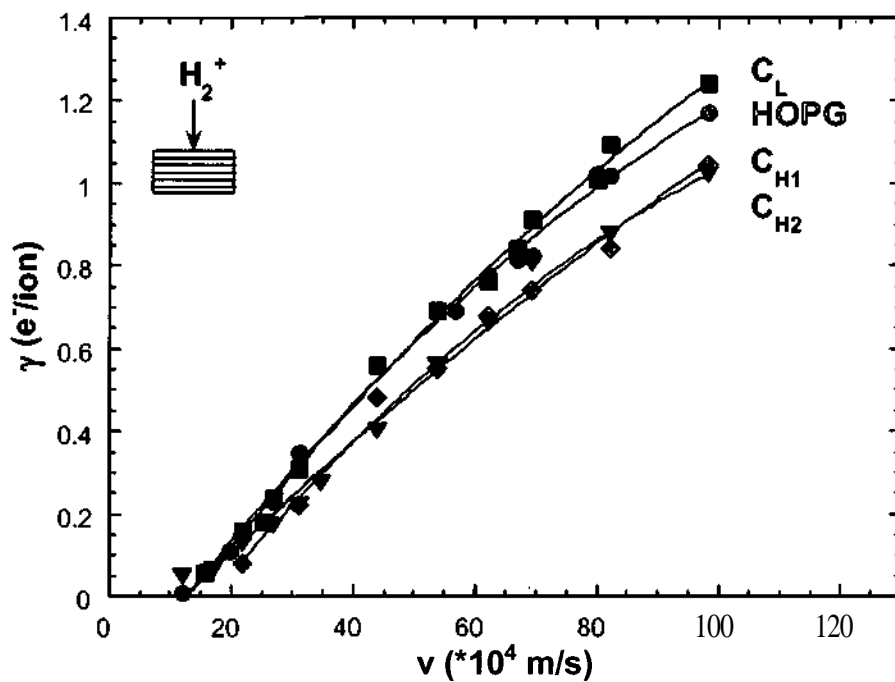

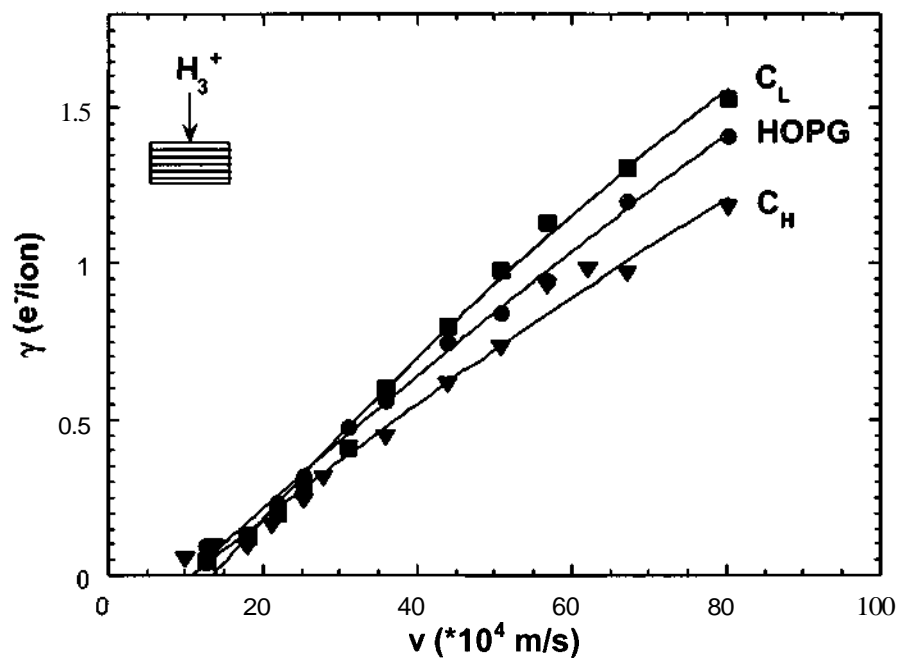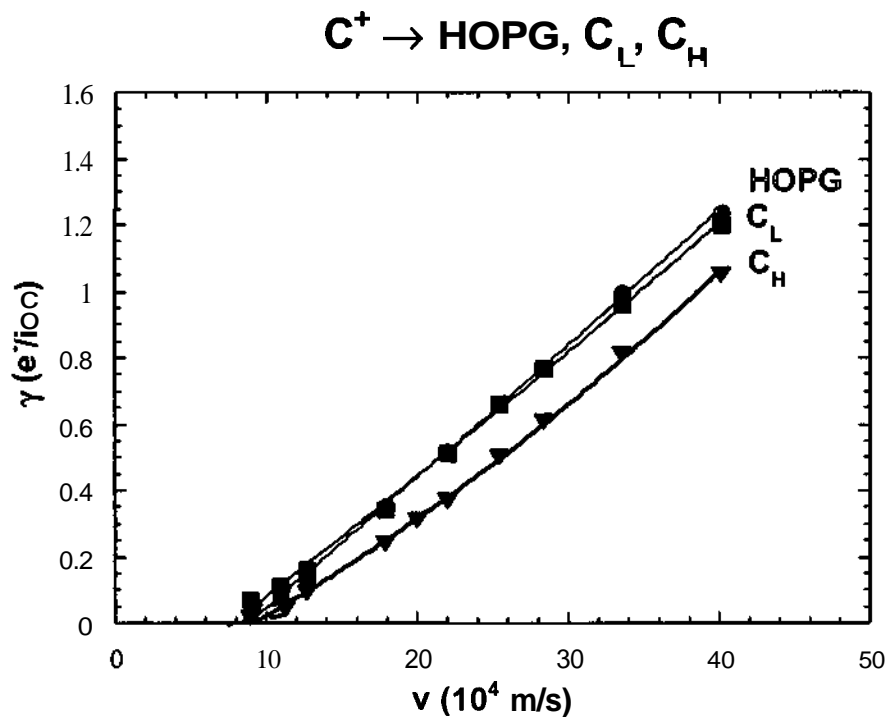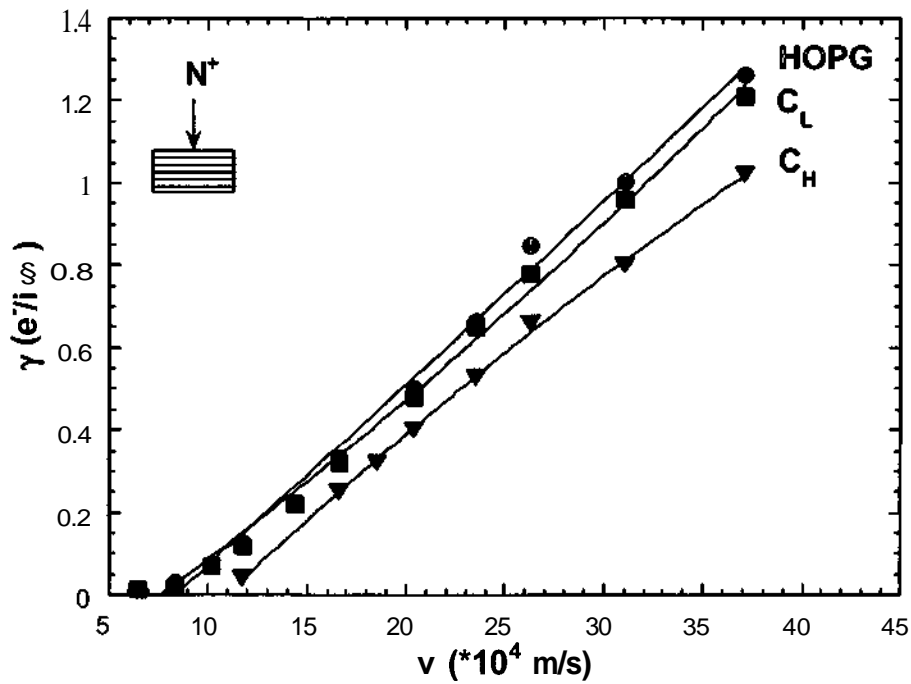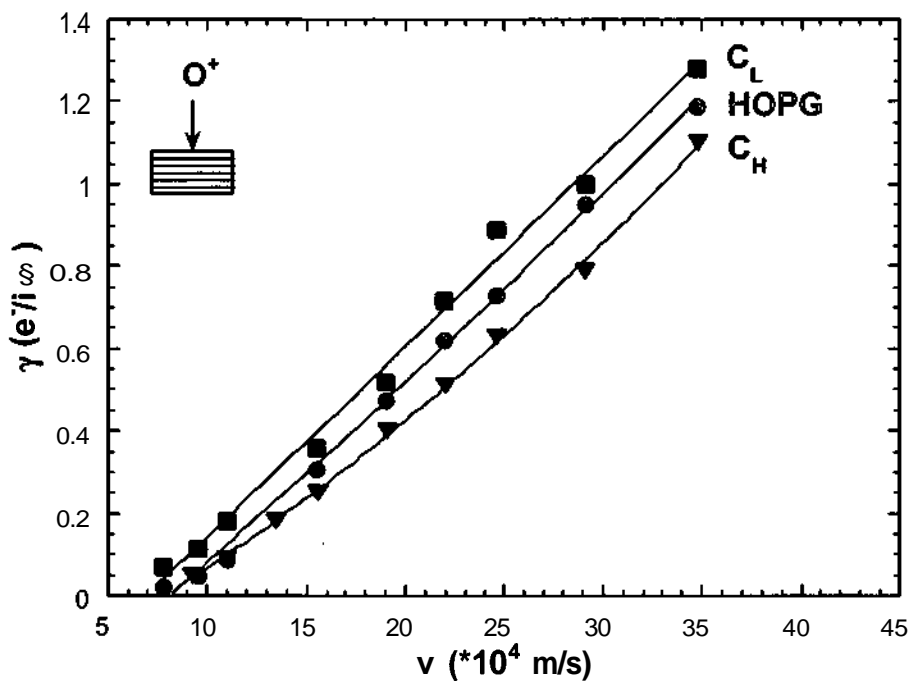*Fig. I.3.1.6: Total electron yields vs. impact velocity v for impact of O⁺ ions on different carbon tile surfaces as well as HOPG (see text) [59].*

While the work functions are almost the same for Au and graphite, their Fermi energies are quite different (fig. I.3.1.7).
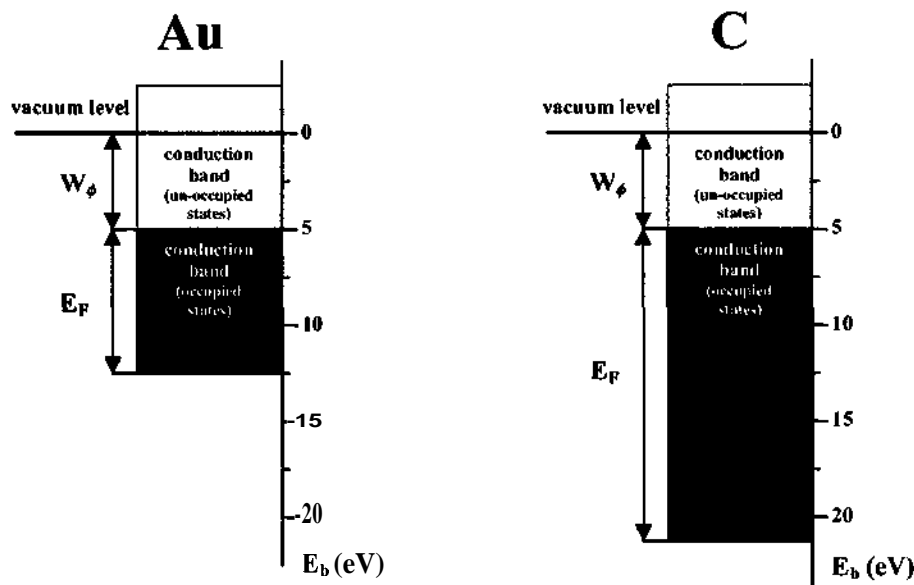
Fig. I.3.1.7: C and Au targets feature similar work function but rather different Fermi energies [60].

This results in an accordingly different value for the "classical threshold" velocity $(v_{th,A}(Au) \sim 2.4 \times 10^5$ m/s or ca. 300 eV/amu; $v_{th,A}(C) \sim 1.5 \times 10^5$ m/s or ca. 120 eV/amu). Experimentally, we observe a correct trend but in a qualitative way only (i.e. $v_{th}(C) < v_{th}(Au)$). With measured $v_{th}(Au) \sim 3.4 \times 10^5$ m/s, electron emission from Au requires higher impact velocities than predicted by eq. (1.1), while for the carbon target electron emission already starts at $v_{th}(C) \sim 1.0 \times 10^5$ m/s and thus clearly lower than calculated by eq. (1.1). This points to the importance of other KE mechanisms like electron promotion into continuum in projectile collisions with individual target atoms [35, 58] and/or a newly proposed "surface assisted KE" process [26]. Recent calculation indeed show that surface assisted KE can explain both the energy dependence and magnitude of the observed electron yields quite well [27] (see fig. I.3.1.8 and fig. I.3.1.9). The reasons for the observed difference between results for HC- and LC- oriented carbon tiles can will be discussed in chap. I 6.3.

Fig. 3.1.8: Comparison between total electron yields vs. impact velocity v for impact of H⁺, H₂⁺, H₃⁺ on HOPG and Au, respectively [59].
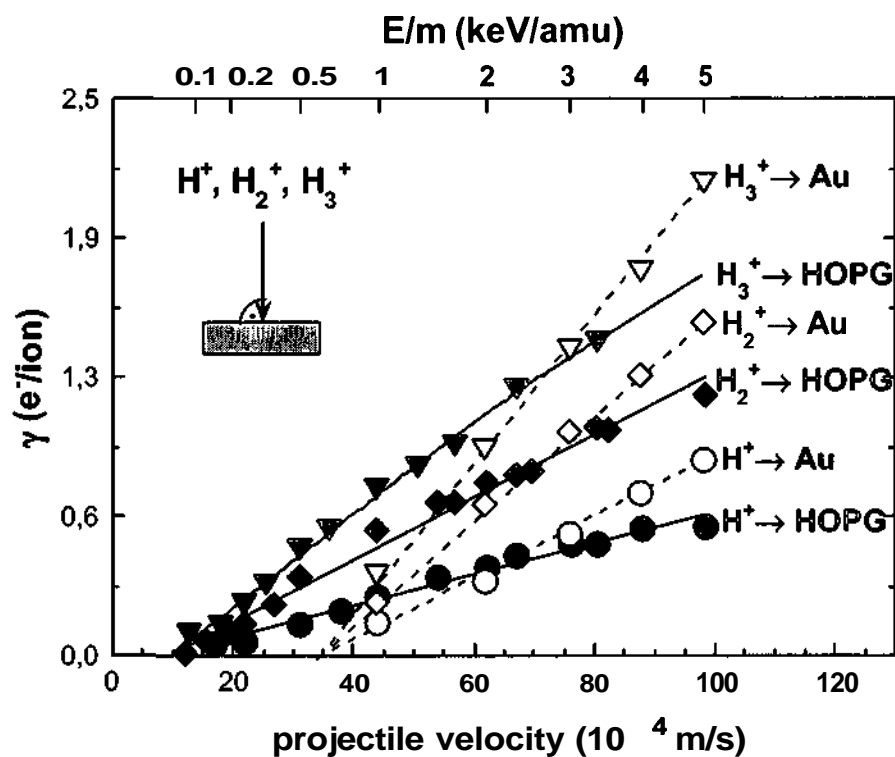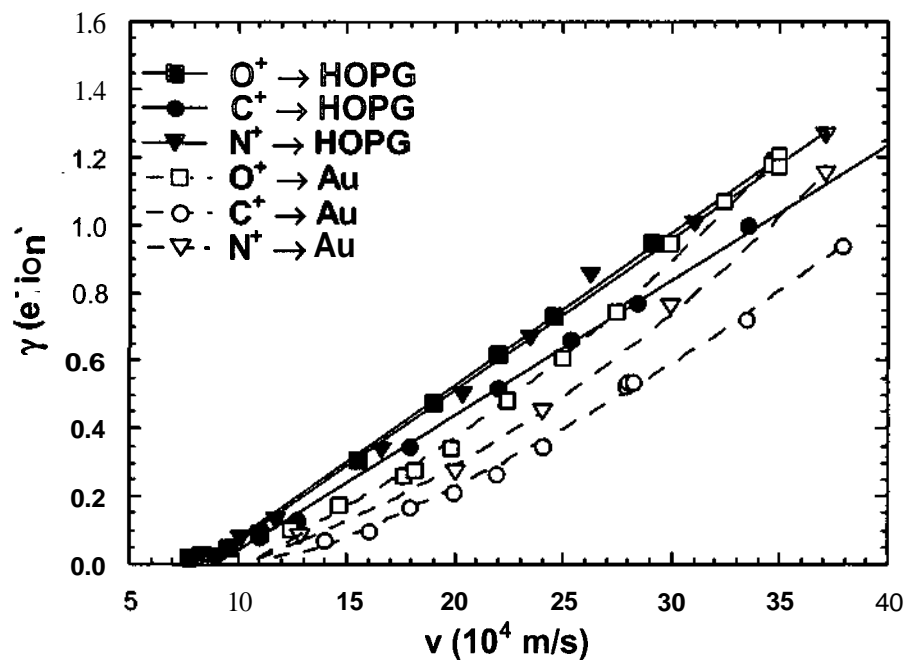

Fig. I.3.1.9: Comparison between total electron yields vs. impact velocity v for impact of C⁺ ' N⁺, O⁺ on HOPG and Au, respectively [59].

I.3.2 Analysis of MO correlation diagrams

MO correlation diagrams for the neutral systems H-C, C-C, N-C, and O-C are shown in fig. I.3.2.1. Atomic units for distance (1 a.u. ≈ 0.053 nm), energy (1.a.u. ~ 27.2 eV) and velocity (l.a.u. ≈ 2.2 x 10^6 m/s) are used. Lörincik et al. (see ref. [27]) calculated these diagrams using the Hartree-Fock method and the computer code Gaussian 98. As a basis set LanL2DZ was used.

Results of the analysis of these MO correlation diagrams (shown in fig. I.3.2.2) are summarized in tab. 3.1. The identified promoted diabatic levels and the corresponding atomic levels in the separated- atom limit are listed in columns 2 and 3 of tab. 3.1. The promoted levels merge into the continuum above the vacuum level at internuclear distances r_c (see column 4). The minimal kinetic energy E_c which is required for reaching these internuclear distances is listed in column 5. These values of E_c are total-energy values taken from the same Hartree-Fock calculations. Such values for $E_{th;C}$ may be underestimated because of two reasons [27].

(1) r_c is the turning point corresponding to the initial energy E_c and therefore the velocity at this point becomes zero, and

(2) E_c was estimated only for head-on collisions.

From our simplified calculation for the H-C system in the gas phase we were not able to estimate the threshold energy because the point at $r_c \sim 2$ a.u. is situated close to the minimum of the total-energy curve.
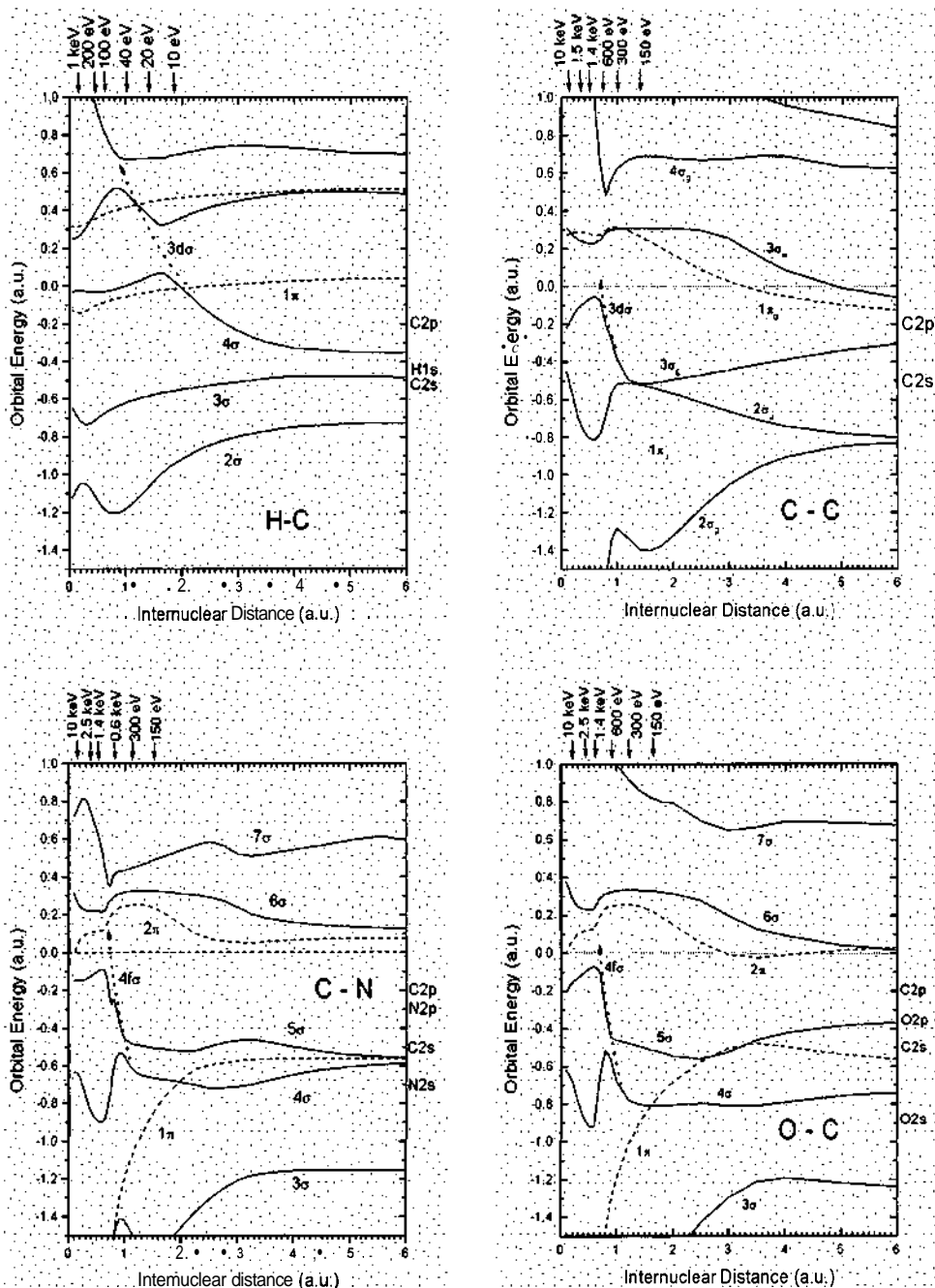
Fig. *I.3.2.1*: *Adiabatic molecular orbital (MO) correlation diagrams for the selected orbitals of (a) H-C, (b) C-C, (c) N-C, and (d) O-C as calculated by the Hartree-Fock method. Solid lines are σ-levels, dashed lines π-levels; the levels for the separated-atom limit are labelled on the right-hand side of the diagram. The dotted heavy curve with an arrow shows the promotion of diabatic levels into the continuum. The adiabatic levels are labelled in the MO notation: The lowest orbital of a given symmetry is numbered 1 and numbering continues in ascending order up to higher energies. In case of C-C an index [g for symmetric ("gerade") and u for asymmetric ("ungerade")] is used to indicate the symmetry of the wave functions. Bars on top of the diagram indicate projectile energies corresponding to the distances of closest approach. Graph taken from Ref. [27].*

System	Promoted diabatic level[1]	SA-limit level	r_c [2] in a.u.	E_c [3] in keV	$E_{th,C}$ [4] in keV	$E_{th,A}$ in keV
H-C	$3d\sigma$	C2p	2.00	-[5]	-[5]	0.1
C-C	$3d\sigma$	C2p	0.70	0.7	>0.7	1.3
N-C	$4f\sigma$	C2s	0.70	0.8	>0.8	1.5
O-C	$4f\sigma$	C2s	0.70	1.0	>1.0	1.8

Tab. 3.1 *Summary of the analysis of MO correlation diagrams*

[1] *According to Barat-Lichten correlation rules [61].*

[2] *Distance of merging of the promoted diabatic level to the continuum.*

[3] *Estimate for the kinetic energy required to just reach r_c, i.e., the velocity at r_c would be zero at this energy.*

[4] *The values for $E_{th,C}$ ore underestimated (cf. text), which is indicated by ">".*

[5] *At $r_c \approx 2$ a.u. the total-energy curve for H-C is close to its minimum and therefore E_c cannot be determined.*

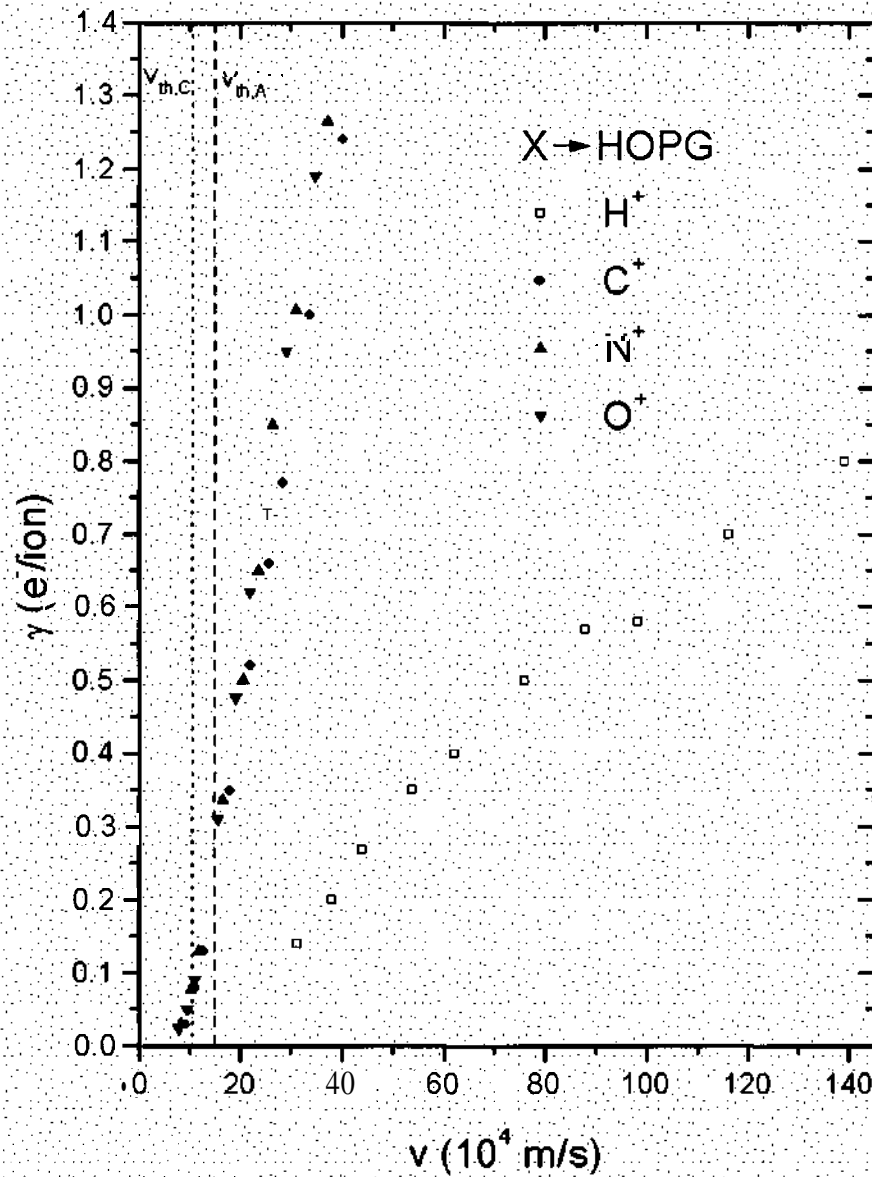*Fig. I.3.2.2: Total electron yields vs. impact velocity v for impact of H^+, C^+, N^+, and O^+ on HOPG. The threshold velocity for binary collision (eq. 1.1, see chap. I 1) $v_{th,A}$ is marked by the dashed line. The threshold velocities $v_{th,C}$ forMO promotion for C-, N-, O-projectiles are marked by a single dotted line, because their values are close to each other.[27]*

I.3.3 Interpretation of experimental results

Lörincik et al. presented in ref. [27] a few qualitative arguments on the relevance of the three KE models mentioned in the introduction. In case of eKE (see chapter I 1) we have estimated using eq. (1.1) that in the keV range of impact energies of C^+, N^+, O^+ projectiles the emission spectrum must be very narrow and electrons with maximum energies around 1 eV can be emitted. It is, however, reasonable to assume that the real spectrum is much broader as is the case e.g., for 4-5 keV Ar^+ on carbon [62]. Therefore, this mechanism cannot account for the experimental data not only in the subthreshold region but also in the "keV" region above $v_{th,A}$ (approximately for $v < 25 \times 10^4$ m/s). Only for impact of protons, electrons can be theoretically excited as high as ≈ 40 eV above the vacuum level and therefore this mechanism may be relevant here.

The mechanism electron promotion followed by Auger emission (EPAE, see also chap. I 1) manifests itself in the KE-spectra as atomic-like peaks or band-like bumps. Usually these features are much narrower than the continuous part of the spectra and therefore their contribution to the total electron yield is in most cases small. Compared to EPAE the mechanism electron promotion followed by molecular autoionization (EPMA, see also chap. I 1) may produce broad continuous spectra. There are two important conditions for an efficient electron emission proceeding via this mechanism:

(i)   the quasimolecular level must be promoted sufficiently high and

(ii)   this level promotion must be fast, i.e., the slope of the promoted diabatic level must be high.

Condition (ii) assures that the promoted level still keeps its "identity" (semilocalized character) when crossing the Fermi and/or vacuum level and decays into the continuum of states far above the vacuum level. This usually happens when the level is promoted from the energy below the bottom of the valence band to the energies above the vacuum level. Such promotion must happen within a short distance of the order of 10^{-1} a.u. Condition (ii) is not fulfilled for all four systems for keV-range of impact energies.

The mechanism sKE does not have any impact velocity threshold therefore it is well applicable in the so-called subthreshold region. In the previous text we presented qualitative arguments that this mechanism may be the most relevant mechanism also in the near-

threshold region above the classical threshold, which is for most projectiles the keV-impact range. Therefore this model can be used for the explanation of most experimental data.

For convenience experimental data shown in fig. I.3.2.1 were replotted in fig. I.3.3.1 in dependence on the inverse impact velocity. The theoretical results based on eq. (1.4) are represented by solid lines. The input parameters and fitting results are summarized in tab. 3.2. The fits according to model sKE are satisfactory for all four collision systems. For comparison we have plotted in fig. I.3.3.1 (by open symbols and dotted lines) also the dependencies of total electron yields for perpendicular impact of H^+, C^+, N^+, and O^+ projectiles on clean polycrystalline gold [26]. These data for gold were also interpreted within sKE mechanism and the agreement with experiment is good. The fitting results are summarized in the second part of tab. 3.2. There are several trends in the microscopical parameters ξ and a from eq. (1.2):

(1) the parameter $\xi \sim 2$ for C^+, N^+, O^+ projectiles for both HOPG and Au, for H^+ projectiles ξ is slightly higher than 2 for HOPG and much higher than 2 for Au,

(2) the parameters a are for HOPG target larger than those for gold and at the same time the values of a are almost the same (HOPG) or only slightly changing (gold) for C^+, N^+, O^+ projectiles, for H^+ a is lower than for the other projectiles.

System	$\rho^2 V^2$	ξ	a [a.u.]
C - HOPG	2.1	2.1	2.2
N - HOPG	2.3	2.2	2.2
O - HOPG	2.5	2.0	2.2
H - HOPG	0.5	2.4	1.6
C - gold	3.3	2.3	1.35
N - gold	3.8	2.1	1.55
O - gold	4.4	1.9	1.7
H - gold	0.5	7.0	0.75

Tab. 3.2:   Results of the fitting of theory to the experiment [27].
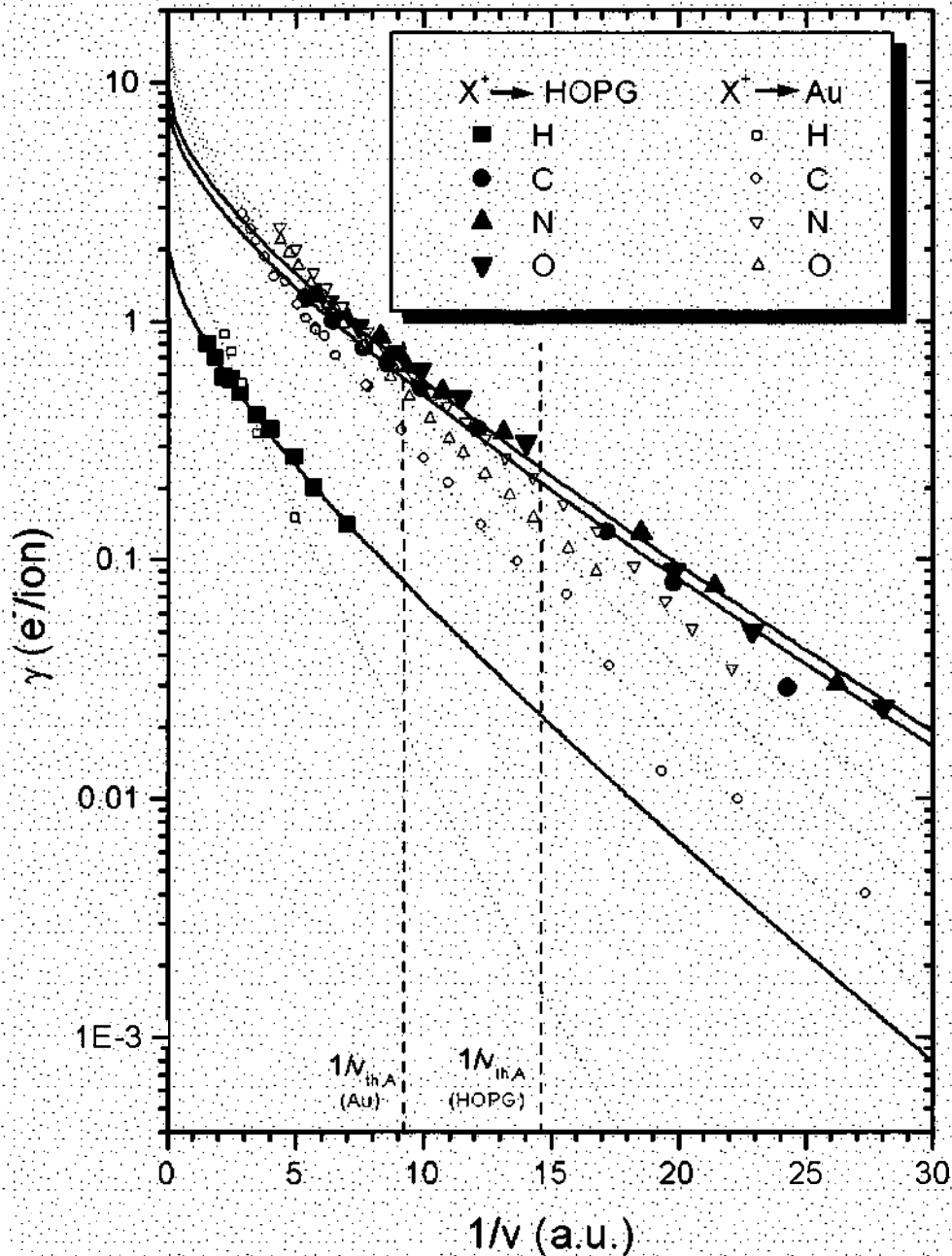
Fig I.3.3.1: Total yields γ for the collision systems H^+-, C^+-, N^+-, and O^+- on HOPG (full symbols) replotted from fig. I.3.2.2 for dependence on the inverse impact velocity. The solid lines are the result of calculations based on eq. (1.4) with the parameters described in the text. For comparison the KE data for gold and the fits based on equation (1.4) are also inserted in the figure (dotted lines). The vertical dashed lines define the subthreshold velocity regions for the eKE mechanism [27].

For proton projectiles, which are already quite fast for keV-impact energies, eKE model becomes more and more significant with increasing velocity. This means that for the proton impact the values for the parameters ξ may be overestimated. Therefore the larger values of parameter ξ for H^+ seems to be in agreement with the expectation that sufficiently far above the threshold eKE may be an equally- or more relevant mechanism than sKE. Given the interpretation of ξ as a correcting factor to the uncertainties of the theory expressed by eq. (1.3) it is surprising that the spread of the values of this parameter for various projectiles (except for H) and targets is so small.

Little or no dependence of the a parameter for the C^+, N^+, O^+ projectiles seems to correlate with the small difference of atomic numbers and masses of the three projectiles. Larger a for HOPG seems to correlate with the higher Fermi energy, i.e. the higher the Fermi energy the faster the decay (the larger the a) of the Fermi-electron wave functions into the vacuum. In case of proton projectiles one can assume that the α-parameter may be slightly underestimated for the same reason as the ξ-parameter might be overestimated.

I.3.4   Conclusions

Experimental data for KE yields have been measured for perpendicular impact of H^+, C^+, N^+, and O^+ projectile ions on HOPG with kinetic energies from a few 100 eV up to 10 keV, and were interpreted within one-electron non-adiabatic theories for KE. At low velocities ($<10^{-1}$ a.u.) the main contribution to the KE yield can be attributed to the sKE mechanism (the so-called surface-assisted KE). The contribution of other mechanisms like eKE (collisions of the projectile with free target electrons) and pKE (promotional KE) should become more important only at higher velocities.

Comparison of KE data for HOPG and gold shows a systematically lower slope for the KE yield dependence on the inverse impact velocity in the case of HOPG (characterized for the sKE mechanism by the parameter a), which is tentatively explained as being due to the difference in the Fermi energies of the targets. In order to check the correctness of the here presented conclusions it would be useful to conduct similar KE yield measurements also for other well-defined target surfaces.

I.4 "Molecular projectile effects" and "isotope effect" for KE

Abstract

Graphite tiles or carbon-coated structures are largely used as wall- or divertor materials in magnetically confined fusion devices. Laboratory work on plasma-wall interaction has so far focused on physical and chemical sputtering yields for such materials. Much less is known on the kinetic and potential electron emission due to ion impact on graphite surfaces, despite the fact that this emission can influence the potential distribution in the plasma sheath and, consequently, the intensity of plasma-wall-interaction. We have investigated electron emission for impact of fusion relevant projectile ions like H^+, H_2^+, H_3^+, D^+, D_2^+, D_3^+, C^{q+}, N^{q+} and O^{q+} on various carbon surfaces. The experiments were performed in the eV - to keV impact energy region typical for fusion edge plasma conditions, by measuring the currents of impinging ions and emitted electrons. As target surfaces, highly oriented pyrolytic graphite (HOPG) samples as well as graphite tiles from the Tokamak experiment TORE supra in CEA Cadarache/France have been used. Results are compared to electron emission data obtained for metal surfaces. This comparative measurements allow to study the influence of different target properties (like Fermi energy and conductivity) on electron transport and therefore on the kinetic electron emission yield. Furthermore the role of these properties for potential electron emission can be better understood.

I.4.1   Introduction

Graphite tiles and carbon coatings are widely used for protecting and conditioning first wall-
and divertor structures in present-day magnetic fusion devices. Because of their close contact
with the energetic boundary plasma these materials become strongly ablated by physical and
chemical sputtering and arcing [63]. This is also highly relevant for plasma impurity
production and depends, among various other influences, on the sheat voltage between the
boundary plasma and the first wall material which decreases with increasing particle-induced
electron emission from the first-wall surface. For an estimate on the importance of this
influence, we have determined total yields y for kinetic electron emission (KE) by impact of
fusion-relevant projectile ions H^+, H_2^+, H_3^+, D^+, D_2^+, D_3^+ (impact energy varied from the
respective KE threshold up to 10 keV) on atomically clean surfaces of highly-oriented
pyrolytic graphite (HOPG) [27, 59]. Experimental methods for these measurements have been
described in chap. I 2.1, i.e. 7 was obtained by measuring the currents of impinging ions and
emitted electrons. Similar KE yield measurements have been performed for graphite tiles
which are utilized for limiter protection in the TORE supra tokamak experiment at CEA
Cadarache, France. These tiles consist of carbon fiber sheets embedded in graphite. Along
these sheets (direction pointing toward the plasma, socalled "HC" side) the tiles feature
considerably higher heat conductivity than perpendicular to the sheets (socalled "LC" side).
Our 7 measurements have shown that there are, as expected, two HC directions with equal
values for 7 and one LC direction perpendicular to them (see chap. I 3).

We now compare total KE yields measured along HC- and LC orientations with obtained 7
data for HOPG, by concentrating on atomic and molecular hydrogen and deuterium projectile
ions. We have used the same methods as with HOPG [59] for preparing the surfaces of
graphite tiles in UHV. Clean surfaces of graphite feature the work functions W_ϕ (5.0 eV). We
therefore expect for both target species with the here applied projectile ions a negligible
influence of potential emission [25], as proven by well defined KE thresholds $v_{th,A}$ [26, 27],
see eq. (1.1) in chapter I 1.

In the following the socalled "molecular effects" for KE will be discussed, i.e. different KE
yields per atomic mass unit for equally fast trimer-, dimer- and monomer ions. Such
molecular effects for KE have been studied by numerous groups (cf. [5, 52] and refs. therein).
For example, if comparably slow (<1 a.u. = 25 keV/amu) hydrogen ions and -atoms impinge
on clean gold [64] and HOPG [59], molecular ions cause smaller KE yields per nucleon than
equally fast protons, which was explained by a relatively stronger electron shielding of the

protons in the molecular ions. Very recently, similar "negative molecular effects" have also been found for impact of medium energy (0.3 - 2 MeV) ions on clean gold [65].

I.4.2 Presentation of measured total electron yields

Fig. I.4.2.1 compares KE yields 7 vs. impact velocity v measured for impact of H^+, H_2^+ and H_3^+ on clean HOPG with equivalent data for impact of D^+, D_2^+ and D_3^+. Within combined experimental errors (see below) no systematically different KE yields ("isotope effects") have been found for equally fast hydrogen- and deuterium ions. The data points have been least-squares fitted to second-order polynomials for later evaluation of molecular effects (see below). Total experimental errors of these data depend on the absolute values of achievable projectile ion currents as well as on the KE yields themselves (larger relative fluctuations for smaller ion currents at low impact energy), which also decrease for lower impact energy. For H^+ projectiles this resulted in total errors for 7 of ± 60 % at 250 eV, ± 20 % at 1 keV, ± 13 % at 4 keV and ± 10 % at 10 keV impact energy. Since at given ion velocity the achievable ion currents as well as the KE yields increase with the number of projectile nucleons (cf. figs. 4.2.1 and 4.2.2), for H_2^+ and H_3^+ the total experimental errors of 7 are considerably smaller than for the equally fast H^+ ions.

Fig. I.4.2.2 shows measured KE yields vs. impact velocity v for impact of H^+, H_2^+ and H_3^+ on atomically clean surfaces of graphite tiles oriented in the HC- (a) and in the LC- (b) direction. Again, second-order polynomials have been least-squares fitted to the data points.

Data shown in figs. 4.2.1 and have been listed in tab. 4.1. Comparison of these data sets shows the following qualitative trends.

(a)   KE yields for HOPG are at any given impact velocity somewhat larger than for HC carbon tiles and somewhat smaller than for LC carbon tiles.

(b)   KE threshold velocities are similar for HC- and LC carbon tiles as for HOPG and not far away from the theoretical value of v_{th} predicted by eq. (1.1).
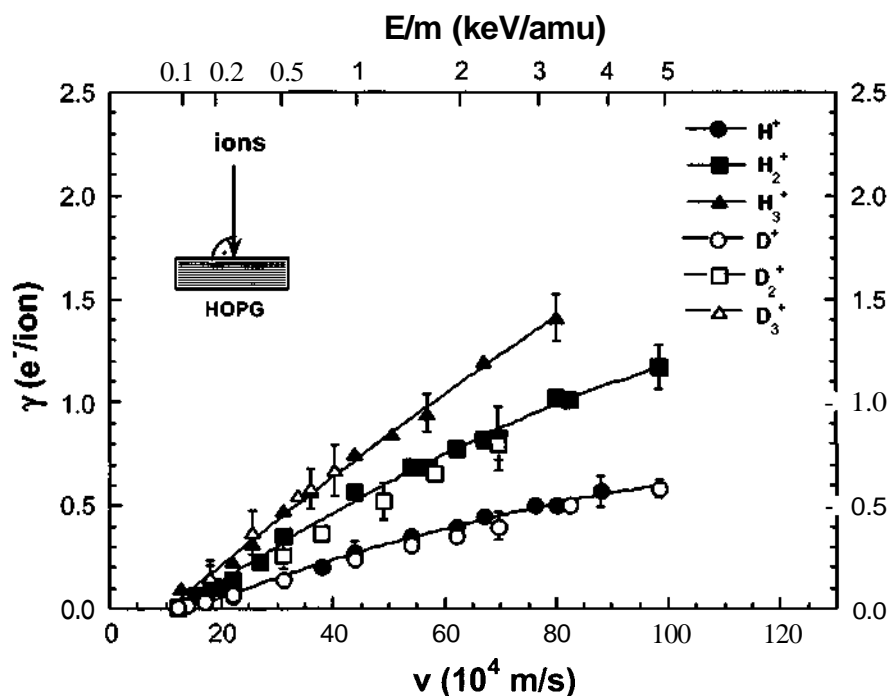
Fig. I.4.2.1: Total yields for electron emission from atomically clean HOPG (highly oriented
pyrolytic graphite, orientation with respect to ion incidence as indicated), for impact of H^+,
H_2^+, H_3^+, D^+, D_2^+ and D_3^+ at impact energies from below KE threshold up to 5 keV/amu [59].
The curves are least-squares second-order polynomial fits to the data points, for which
typical total error bars have been indicated (for further discussion cf. text) [52].

For discussing possible molecular projectile effects we have compared in tab. 4.1 the KE
yields per nucleon for all three ion species at two different impact velocities. These *y* data
taken from respective values of the fitting curves were used to calculate the ratios shown on
the right hand side of tab. 4.2. Significant deviation of these ratios from unity points to
molecular projectile effects, which are clearly seen for the HC carbon tile surface, but within
the experimental errors neither for the HOPG- nor the LC carbon tile surface.
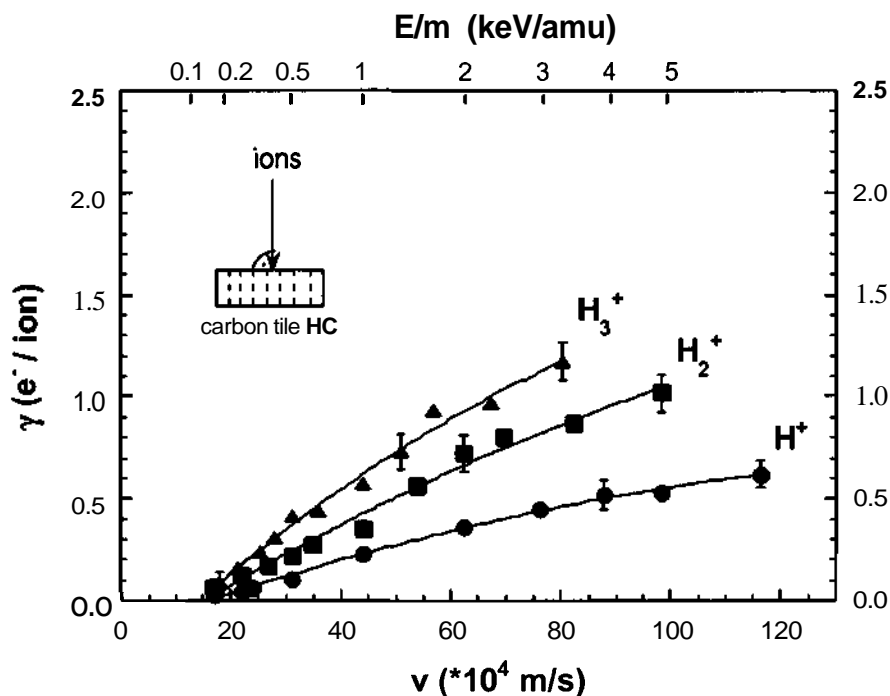
Fig. I.4.2.2 (a): Total electron yields for atomically clean surface of carbon-fiber enforced graphite ("HC" - high heat conduction orientated fiber fabrics with respect to ion incidence as indicated), for impact of H^+, H_2^+, H_3^+ from below KE threshold up to 5 keV/amu. Fit curves obtained as for fig. 4.1.1 [52].
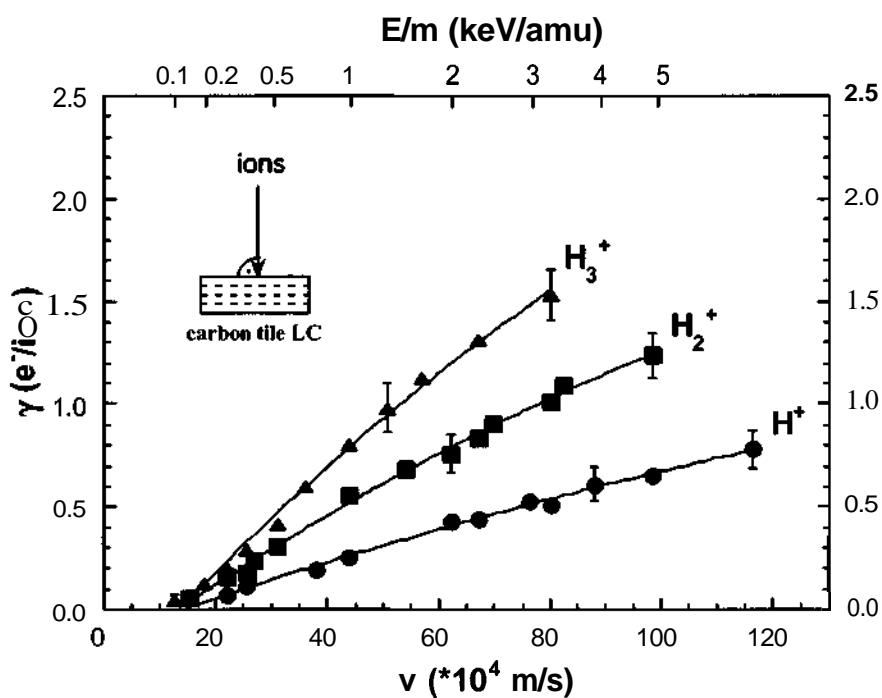

Fig. I.4.2.2 (b): Same as for fig. I.4.4.2(a), but for low heat conduction orientated carbon fibers ("LC") as indicated [52].

E (keV)	γ (e⁻/ion) HOPG					
	H^+	H_2^+	H_3^+	D^+	D_2^+	D_3^+
0.15	0.06	0.007	-	0.01	-	-
0.20	-	-	-	0.02	-	-
0.25	0.07	0.06	0.10	-	-	-
0.30	-	-	-	0.03	-	-
0.40	-	0.11	-	-	-	-
0.50	0.14	0.14	0.13	0.07	-	-
0.75	0.20	0.25	0.23	-	-	-
1.00	0.27	0.35	0.32	0.14	-	0.15
1.50	0.35	-	0.48	-	-	-
2.00	0.40	0.56	0.56	0.24	0.26	0.37
2.33	0.45	-	-	-	-	-
3.33	0.49	0.68	-	-	-	-
3.00	0.51	0.70	0.75	0.31	0.36	-
3.50	-	-	-	-	-	0.55
4.00	0.57	0.78	0.84	0.35	-	0.58
4.66	-	0.81	-	-	-	-
5.00	0.58	0.82	0.94	0.40	0.52	0.67
6.66	-	1.00	-	-	-	-
7.00	-	1.02	1.20	0.50	0.65	-
10.0	-	1.17	1.41	0.580	0.79	-

Table 4.1a: Measured total KE yields for impact of H^+, H_2^+, H_3^+, D^+, D_2^+ and D_3^+ on atomically clean surfaces ofHOPG [59, 66].

E (keV)	Y(e⁻/ion) HC			Y(e⁻/ion) LC		
	H^+	H_2^+	H_3^+	H^+	H_2^+	H_3^+
0.15	0.04	-	-	-	-	-
0.25	0.03	-	-	0.07	-	0.04
0.30	0.06	0.07	-	-	0.06	-
0.33	-	-	-	0.11	-	-
0.50	0.11	0.13	0.09	-	0.16	0.12
0.66	-	-	-	-	0.18	-
0.75	-	0.17	0.16	0.2	0.24	0.20
1.00	0.23	0.22	0.26	0.26	0.31	0.29
1.20	-	0.28	0.31	-	-	-
1.50	-	-	0.41	-	-	0.41
2.00	0.36	0.35	0.44	0.43	0.56	0.60
2.33	-	-	-	0.44	-	-
3.00	0.45	0.56	0.57	0.53	0.69	0.80
3.33	-	-	-	0.51	-	-
4.00	0.52	0.72	0.73	0.61	0.76	0.98
4.66	-	-	-	-	0.48	-
5.00	0.53	0.81	0.93	0.65	0.91	1.13
6.66	-	-	-	-	1.01	-
7.00	0.62	0.87	0.97	0.78	1.09	1.31
10.0	-	1.17	1.17	-	1.24	1.53

Table 4.1.1b: Measured total KE yields for impact of H^+, H_2^+ and H_3^+ on LC- and HC fiber-enforced graphite.

HOPG

v (10^5 m/s)	γ (H^+)	γ (H_2^+)	γ (H_3^+)	y (H_2^+)/2γ (H^+)	y (H_3^+)/3γ (H^+)
4.0	0.23	0.45	0.64	0.98±0.25	0.93±0.2
8.0	0.50	0.94	1.39	0.99±0.17	0.93±0.2

Carbon tile (HC)

v (10 m/s)	γ (H^+)	γ (H_2^+)	γ (H_3^+)	γ (H_2^+)/2γ (H^+)	γ (H_3^+)/3γ (H^+)
4.0	0.19	0.36	0.54	0.92±0.2	0.93+0.2
8.0	0.46	0.85	1.16	0.92±0.12	0.84+0.1

Carbon tile (LC)

v (10 m/s)	γ (H^+)	γ (H_2^+)	γ (H_3^+)	y (H_2^+)/2γ (H^+)	γ (H_3^+)/3γ (H^+)
4.0	0.23	0.45	0.69	0.98±0.22	1.00+0.2
8.0	0.54	1.09	1.53	1.05±0.15	0.94+0.1

Table 4.2: *Experimental KE yield data characterizing possible molecular effects for impact of H^+, H_2^+ and H_3^+ on atomically clean surfaces of HOPG and carbon fiber enforced graphite tiles.*

Although we did not perform measurements with fast neutral hydrogen atoms on graphite, we can evaluate a hypothetical H°-yield under the assumption that the relation for equally fast ions

$$\gamma(H_n^+) = \gamma(H^+) + (n-1)\,\gamma(H^0) \tag{4.1}$$

holds for graphite in the same way as for the Au target [55, 59], and therefore we should obtain

$$\gamma(H^0) = (\gamma(H_n^+) - \gamma(H^+))\,/\,(n-1) \tag{4.2}$$

Values for $\gamma(H^0)$ derived in this way are shown in fig. I.4.2.3, 4.2.5 and 4.2.7 together with measured yields (in electrons per proton) for the various hydrogen ions as a function of the number of projectile screening electrons for HOPG and carbon tiles. Within the combined error bars ($\pm 10\ \%$) the $y(H°)$ values calculated according to eq. (4.1) from data for protons and H_2^+ agree with values derived from yields for protons and H_3^+, respectively. This agreement gives confidence that eq. (4.2) can also be applied to molecular hydrogen ions on graphite (as in the case of Au). As a result we find that hydrogen atoms liberate about 10% less electrons than equally fast protons.

Figs. 4.2.4, 4.2.6 and 4.2.8 show the ratios of the electron emission yields for H_3^+ (blue dots) and H_2^+ (green dots) and the yields for protons at same impact velocity for impact on clean HOPG and carbon tiles. In the absence of a molecular effect this ratios should be equal to $3\,\gamma(H_3^+)$ and $2\,\gamma(H_2^+)$, respectively.
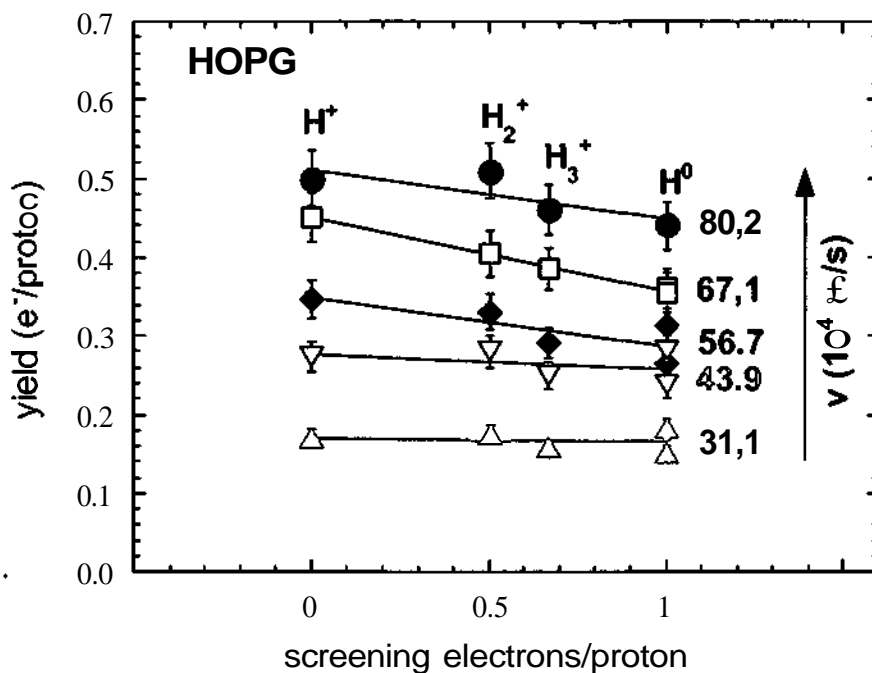
Fig. I.4.2.3: Measured electron yields per proton for impact of atomic and molecular hydrogen projectiles on clean HOPG plotted as a function of the number of screening electrons per proton at different projectile velocities. Yields for hydrogen atoms H^0 were derived from data for impact of protons and H_2^+ or protons and H_3^+, respectively by using eq. (4.1).
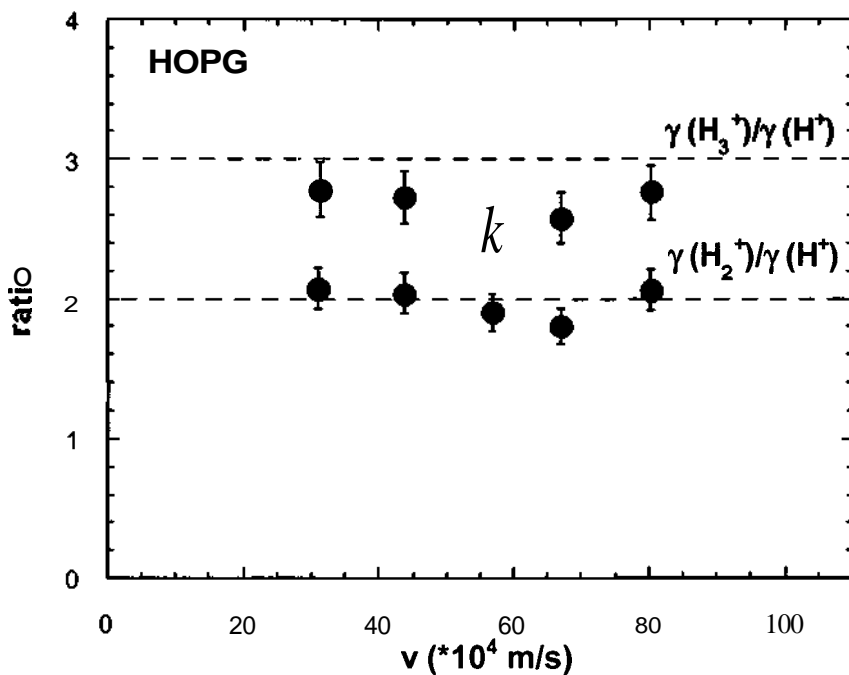

Fig. I.4.2.4: Ratios of the electron emission yields for H_3^+ (blue dots) and H_2^+ (green dots) and the yields for protons at same impact velocity for impact on clean HOPG. In the absence of a molecular effect this ratios should be equal to 3 H_3^+ and 2 H_2^+, respectively.
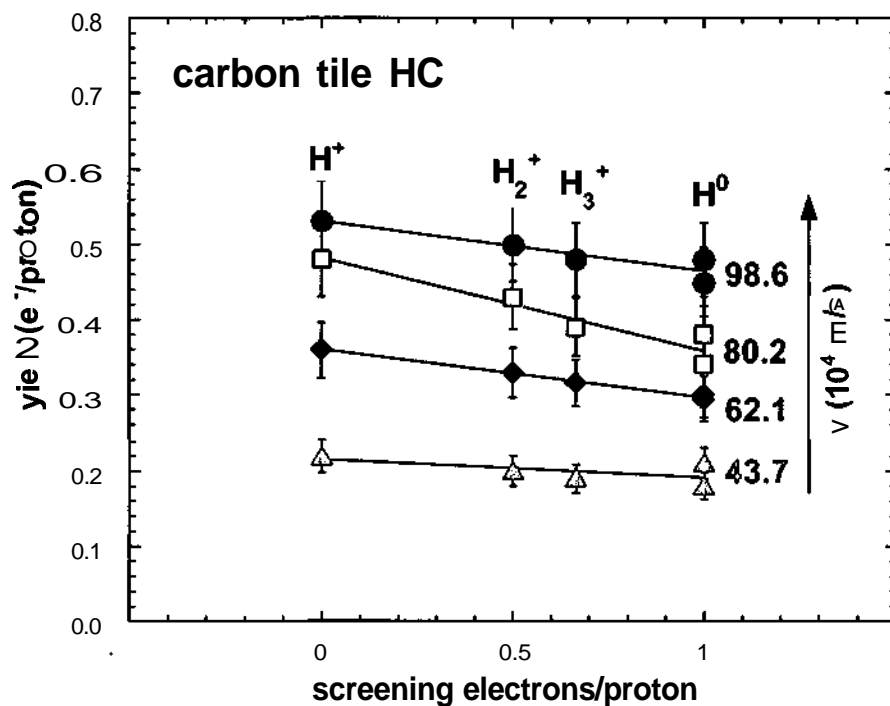
Fig. I.4.2.5: Measured electron yields per proton for impact of atomic and molecular hydrogen projectiles on clean carbon tile HC-direction plotted as a function of the number of screening electrons per proton at different projectile velocities.

Fig. I.4.2.6: Ratios of the electron emission yields for H_3^+ (blue dots) and H_2^+ (green dots) and the yields for protons at same impact velocity for impact on clean carbon tile (HC).

Fig. *I.4.2.7*: *Measured electron yields per proton for impact of atomic and molecular hydrogen projectiles on clean carbon tile LC-direction plotted as a function of the number of screening electrons per proton at different projectile velocities.*
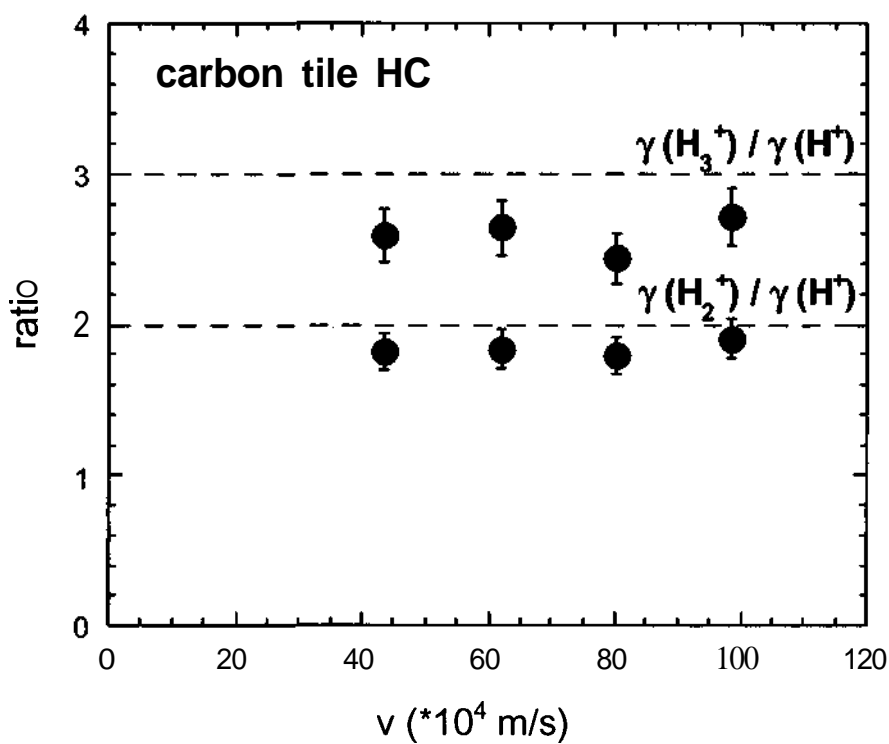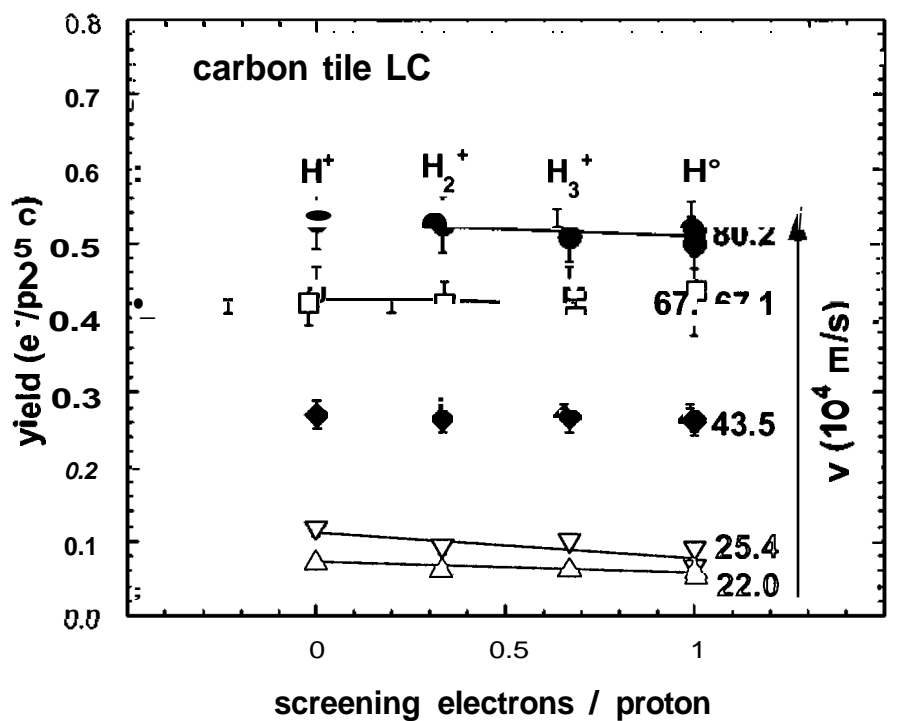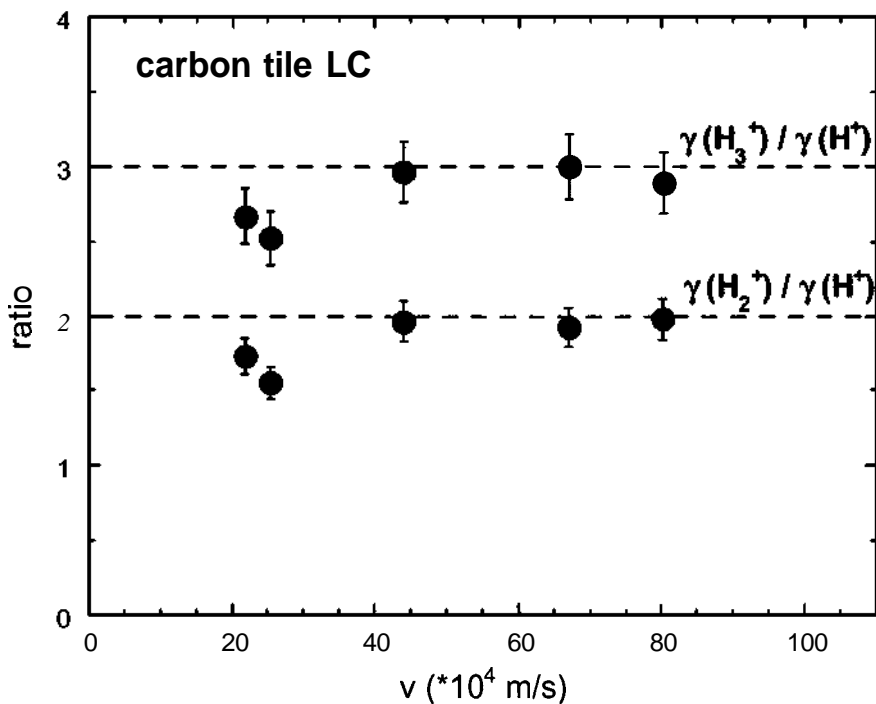

Fig. *I.4.2.6*: *Ratios of the electron emission yields for H_3^+ (blue dots) and H_2^+ (green dots) and the yields for protons at same impact velocity for impact on clean carbon tile (LC).*

I.4.3   Molecular projectile effects for KE yields

I.4.3.1   Calculations of electronic stopping for hydrogen monomer- and dimer atoms

Molecular effects for KE yields 7 are now discussed with the help of another closely related quantity, namely the corresponding electronic projectile energy loss S. As a rough first approximation, the KE yield can be assumed as linearly proportional to this energy loss: $7 = A \times S$. The proportionality constant A depends on the specific projectile-target combination. Deviations from this proportionality are typically of the order of 10% and depend on the specific systems under study [67]. In many cases the electronic excitations of metals can be theoretically described by the excitation spectrum of a free electron gas with its electron density no or mean one-electron radius r_s defined as $r_s = [3/(4\pi n_0)]^{1/3}$. For projectiles with velocity v smaller than the Fermi velocity VF in the particular medium, the perturbation introduced by an incident particle in the electron gas is too strong to be obtained in linear reponse theory and non-perturbative approaches are therefore required. The electronic energy loss S of atomic H- and molecular H_2 projectiles in a free electron gas was calculated in ref. [68], using the scattering formalism in which the energy deposited by the projectile in the medium is obtained through the scattering of the Fermi electrons off the projectile screened potential.

The effective one-electron scattering potential was calculated self-consistently using Density Functional Theory. Results of ref. [68] show that the electronic energy loss S of H_2 molecules in a free electron gas is smaller than twice the energy loss of atomic H projectiles: $S(H_2)/2S(H) < 1$ for the whole range of metallic electron densities (socalled "vicinage effect"). The electrons in the H2 molecule are more deeply bound as compared to the case of atomic H projectiles and hence they are more effective in screening the proton potential. Complex phenomena of multiple scattering of the medium electrons at the two centers of the molecule are added up as well.

The theoretical results of ref. [68] can be used to explain experimental KE yields for atomic and molecular hydrogen projectiles, using some further approximations [66]:

(i)   The collected electrons are emitted from the first few layers of the surface so that the molecule internuclear distance can be assumed as constant,

(ii)   The neutralization of the projectiles is very fast,

(iii)   The proportionality constant A is the same for H and H2.

Under these assumptions, the theoretical ratio S(H2) / 2 S(H) becomes equal to the ratio of KE yields y(H2) / 2 γ(H). Measured values of y(H2) / 2 y(H) < 1 for systems under study (i.e. molecular projectile effects) would then just be a consequence of the vicinage effect in the electronic projectile energy loss.

I.4.3.2   Comparison with present experimental results and data for other target surfaces

The calculated vicinage effect is illustrated in fig. I.4.3.1, in which we have plotted the theoretical value of the ratio S(H2) / 2 S(H) as a function of the electronic density parameter r_s. Diez Muino et al. [66] compared the results to experimental ratios $\gamma(H_2)$ / 2 y(H) for a number of targets. Effective r_s values used to plot this data were taken from experimental values of the respective plasmon peak energies as measured with electron energy loss spectroscopy. Besides the measured y data from the present work, experimental KE yields from ref. [69] were included. Fig. I.4.3.1 shows a similar trend for the calculated values of S(H2) / 2 S(H) as for the corresponding KE yield ratios which is a remarkable result, taking into account the important approximations used for this comparison: Electrons emitted after dissociation of the molecule would reduce the molecular effect for the KE yield. Our calculation assumes that the H2 molecule keeps a constant internuclear distance and hence its result can be considered as a lower boundary for the ratio S(H2) / 2 S(H).
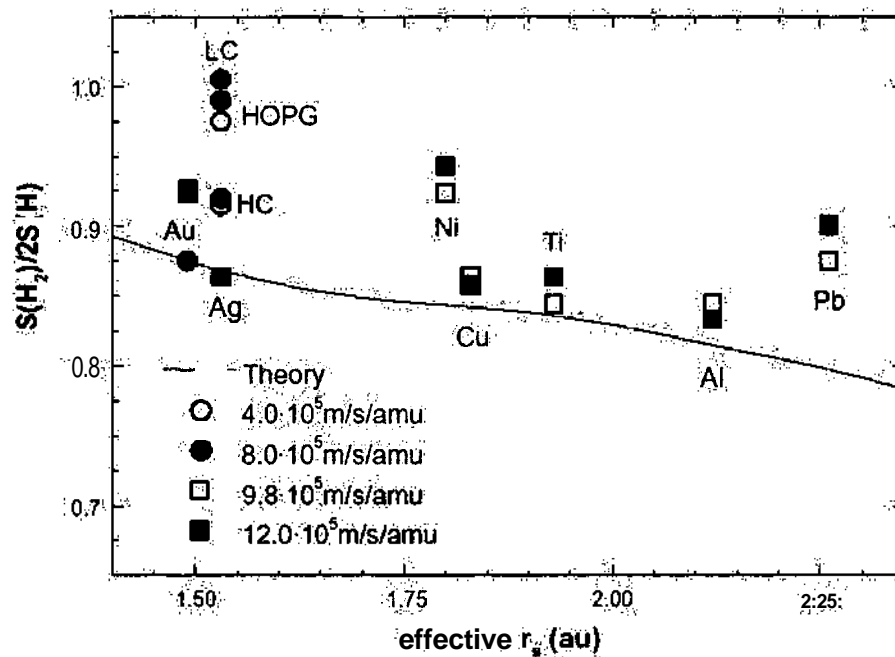
Fig. 4.3.1: Ratios between electronic energy loss of H₂ and twice the energy loss of H S(H₂) / 2S(H), as a function of the effective electron density parameter r_s (in units of the Bohr radius a_0) [66]. Solid line is the theoretical result. The circles are the experimental values (ratios of total KE yields) of this work [open (solid) symbols correspond to projectile velocities of 4x10(8x10⁵) m/s]. The experimental data for clean gold are taken from ref. [55, 59]. The squares are experimental data taken from ref. [69] [open (solid) symbols correspond to projectile energies of 5 keV/amu (7.5 keV/amu)].

I.4.4   Summary and conclusions

In the present work we have presented measured KE yields for impact of atomic and molecular hydrogen ions (impact energy < 10 keV) on carbon-fiber enforced graphite with two different fiber orientations - high (HC) - and low heat conductivity (LC) - and on highly-oriented pyrolytic graphite (HOPG).

We found KE yields for HOPG at given impact velocity to be somewhat larger than for HC carbon tiles and somewhat smaller than for LC carbon tiles. Measured KE threshold velocities v_{th} are similar for HC- and LC carbon tiles as for HOPG, in fair agreement with a theoretical value of v_{th} predicted from a simple free-electron gas model for graphite. Comparison of our measured KE yields for atomic and molecular hydrogen projectile ions shows almost no molecular effects (i.e. smaller yields per projectile nucleon for the molecular ions) for both HOPG and LC graphite and only weak molecular effects for HC graphite. On the other hand, calculation of atomic and molecular projectile stopping in free-electron gas targets with appropriate density yields molecular effects for graphite and a number of metal targets which become slightly more important with decreasing target density ("vicinage effect"). If a close relation between the projectile stopping and the KE yield is assumed, a similar tendency should be given for molecular projectile effects in KE, which indeed has been found from experiments.

I.5 Influence of Electron Emission on the Plasma Sheath Potential

I.5.1 Introduction

Our experimental studies have concentrated on basic physical aspects like the underlying electron emission mechanisms, etc. However, electron emission might also play an important role for plasma-wall interaction by influencing the boundary plasma (e.g. via the sheath potential) and the intensity of plasma-wall interaction accordingly. Basically, a fairly large yield of emitted electrons is needed to reduce the sheath potential. This in turn reduces the impact energy of ions and consequently the ion flux to the surface and the related sputtering yield.

However, a quantitative treatment suffers from the complexity and intimate interactions of all processes involved. In chapter I 5.2 the available literature is reviewed and some simple estimates on the relevance of our investigations for plasma wall interaction in fusion devices is presented. For a more quantitative simulation a collaboration with the theory group of Prof. S. Kuhn at Univ. Innsbruck has been started [52, 60]. First results of these simulations are described in chapter I 5.3.

I.5.2 Simple estimates

I.5.2.1 Electron induced electron emission:

The role of electron (re-)emission and its influence on the plasma sheath potential have been treated by various authors [37, 38, 70-74]. The normalized sheath potential ψ_s in the presence of (electron induced) electron emission is given by [36, 60]

$$\psi_s = \frac{eV_s}{kT_e} = -\frac{1}{2}\ln\left\{\frac{2\pi \cdot m_e \cdot (1 + T_e / T_i)}{m_i \cdot (1 - \gamma)^2}\right\}$$ (5.1)

where mi, m_e, Ti and T_e are the ion and electron masses and temperatures, respectively and Y denotes the secondary emission yield (see fig. I.5.2.1).
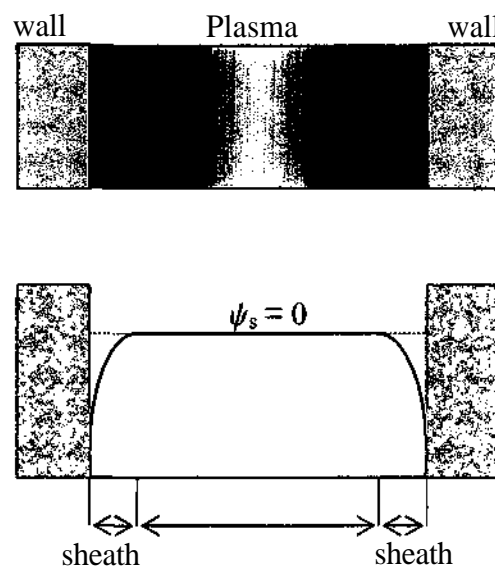

Fig. I.5.2.1: The plasma potential ψ_s forms sheaths near the walls.

In the absence of space charge the sheath potential for a pure hydrogen plasma drops to zero at around y = 0.92 [70, 71], a value typically reached for 200 - 300 eV electrons on graphite surfaces at incidence angles > 60° with respect to the surface normal [71]. However, in the scrape-off layer (SOL) plasma of toroidal fusion devices with magnetic divertors, magnetic field lines usually connect to the target plates at grazing incidence. The electron gyromotion around the grazingly incident magnetic field lines tend to suppress electron emission [72]. The relevance of this effect depends on the strength of the electric field across the plasma sheath that accelerates the emitted electrons away from the target surface. This situation calls for more detailed simulation calculations.

I.5.2.2   Singly charged ion induced electron emission:

As seen from the data presented in chap. I 3.1, electron emission induced by impact of singly charged ions on carbon targets only starts at an impact energy of about 50 eV/amu. At typical sheath potentials of 200 V the total electron yield even for the light hydrogen ions is still rather small (typ. 0.2 electrons/ion) compared to the electron induced emission yield. Singly-charged ion-induced electron emission is therefore usually neglected in plasma simulation codes. However, ion-induced kinetic electron emission exhibits an impact angle 0 dependence of approximately $\gamma(\Theta) \sim \gamma_0 \times \cos^{-1}(\Theta)$ [5], which means that under more grazing angles of incidence the yields become much larger. Again, a more definite answer for the role of ion-induced electron emission can only be gained from simulation calculations.

I.5.2.3   Multiply charged ion induced electron emission:

So far only preliminary results have been obtained with multiply charged ions. Fig. I.5.2.2 , fig. I.5.2.3 and fig. I.5.2.4 show measured total electron yields y induced by impact of C^+, C^{2+}, C^{4+} , C^{5+}, N^+, N^{3+}, O^+ and O^{2+} ions on carbon tiles (C_L only) as well as on HOPG. The electron yield strongly increases with projectile charge state which can be attributed to potential electron emission (PE) [15]. Since PE has no impact energy threshold [13], electrons can be emitted already at impact energies of a few eV only.

The electron yield for multiply charged ions (MCIs) strongly increases with projectile charge state q of the ion [15]. Moreover, the predominant potential electron emission has no impact energy threshold, which means that a considerable number of electrons can be emitted even at the lowest impact energies. Furthermore, MCIs due to their higher charge are accelerated by the sheath potential to higher impact energies $(q \times V_S)$ as compared to singly charged ions (several keV instead of several 100 eV), which adds to the electron emission yield due to an increasing importance of kinetic electron emission (see fig. I.5.2.2). To exert an influence on the sheath structure, the flux of electrons emitted due to MCIs has to be a substantial fraction of the total number of emitted electrons. According to an estimate presented by K. Lackner and J. Schweinzer 1996 [75] under the assumption of a maximum $Z_{eff} = 2$, a potential role of MCI-induced electron emission can be expected if $\gamma \approx Z$. This condition is actually met if one considers our results presented in fig. I.5.2.2.
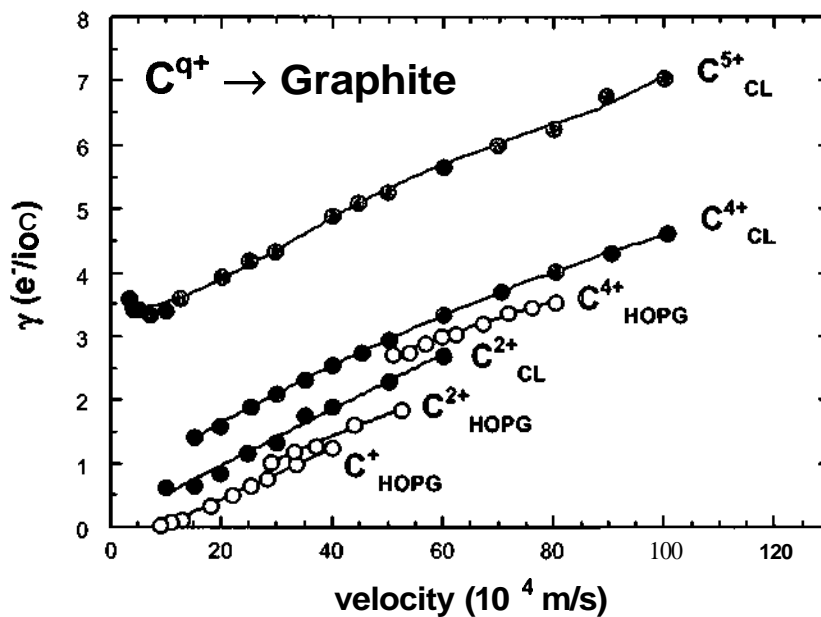

Fig. I.5.2.2: Total electron yields vs. impact velocity v for impact of C^+, C^{2+}, C^{4+} and C^{5+} ions on carbon tiles (C_L only) and HOPG [60].
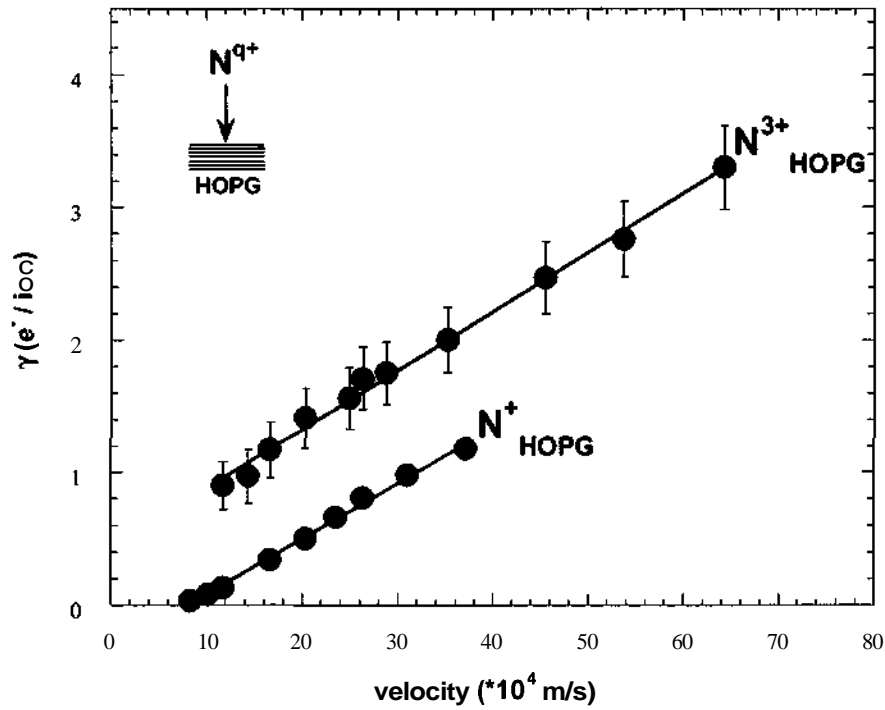
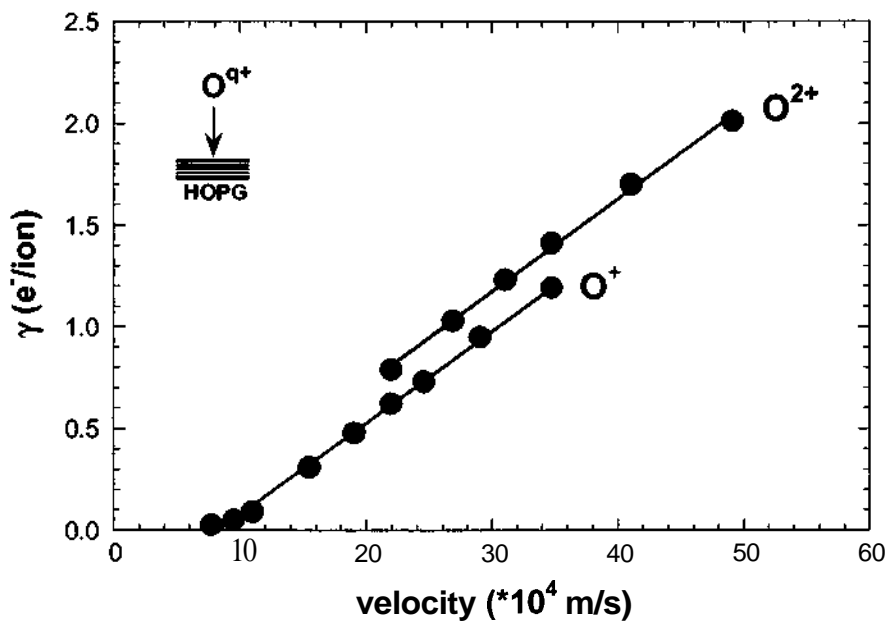*Fig. I.5.2.3: Total electron yields vs. impact velocity v forimpact of N^+, N^+ ions on HOPG.*

Fig. I.5.2.4: Total electron yields vs. impact velocity v forimpact of O^+, O^+ ions on HOPG.

I.5.3   PIC simulations

In order to estimate the effect of electron- and ion-induced electron emission from a plasma facing surface on the plasma sheath potential in a more quantitative manner, a collaboration with the theory group of Prof. S. Kuhn at Univ. Innsbruck has been initiated. The investigations were carried out using the slightly modified ES ID-code (Bounded Electrostatic 1 Dimensional Code) called BIT1 (Berkeley-Innbruck-Tbilisi) [76].

The angle between magnetic field lines and the surface-normal could be chosen arbitrarily. Runs for rather oblique incident magnetic field lines show that secondary electron emission has a larger influence on the sheath potential than singly charged hydrogen ion-induced electron emission. At steeper impact angle of the magnetic field lines the effect of electron emission on the sheath potential increased significantly.

However, the simulated plasma only consisted of electrons and singly-charged hydrogen-ions without any impurity ions. First runs with the inclusion of model impurity ions show a pronounced influence on the sheath potential. Further investigation and simulations are necessary to clarify the role of multiply charged ion species on the sheath potential.

I.6 Ion-induced KE from HOPG surfaces of different conductivities

Abstract

In this chapter we present total electron yields determined by current measurements for normal and under 45 degree impact of C^+, N^+, O^+, Ar^+ and Xe^+ ($3 < E < 10\,keV$) on clean highly-oriented pyrolytic graphite (HOPG). HOPG features layered carbon sheets, which exhibit large differences in electrical and thermal conductivity parallel and perpendicular to the layers. Since electron transport in a conductor is related to thermal conductivity, we expected to see a pronounced target-orientation dependent electron emission. Indeed measured yields form the high conductivity side of HOPG showed an enhancement of up to 40% yields over for the low conductivity side. However, further measurements at different impact angles related the observed yield enhancement variously to differences in surface roughness of the two targets.

I.6.1   Introduction

Electron emission from solid surfaces by impact of energetic ions is a well investigated phenomenon [5, 13, 58]. One generally distinguishes between two mechanisms for ion-induced electron emission. Kinetic emission (KE) is caused by the kinetic energy of the impinging projectile ions and involves a certain impact velocity threshold. In potential emission (PE) the emitted electrons originates from neutralization and deexcitation processes. PE can only take place when the total ion recombination energy surpasses twice the surface work function W_ϕ. In recent studies for atomically clean gold surface [25] some contributions to the total electron emission yield could be disentangled. The domain of exclusive PE can be investigated with very slow ions in higher charge states [22, 23]. Coincidence measurements between emitted electrons and projectiles scattered under grazing angles from a monocrystalline surface can separate PE and KE contributions [24]. Exclusive KE mechanisms have been studied at the KE velocity threshold for various singly charged ions on polycrystalline Au [25] and for energetic neutral atoms grazingly incident on LiF(OOl) [77, 78]. Earlier investigations with atomically clean polycrystalline gold [46] and HOPG [59] clarified the role of electronic target properties for the KE mechanisms, like electron promotion into continuum in projectile collisions with individual target atoms [35, 58] and induced a new "surface-assisted KE" mechanism [26]. Recent calculation showed indeed that surface-assisted KE can explain both the energy dependence and magnitude of the observed electron yields quite well [27].

Most studies on kinetic electron emission have so far focused on the primary mechanism of generating excited electrons within the target surface. However, before their escape into vacuum, electrons produced in this way have to diffuse towards the surface [4, 5] and therefore the electron transport can have a significant influence on the resulting total electron yield. For example, as it is commonly assumed that the mean free path of low energy electrons is larger for insulators than for metals, also their escape depth and thus the total electron yield should be larger [5]. Because of quite different mechanisms causing KE from insolating and conducting surfaces, it is however difficult to separate the role of electron transport from the primary excitation mechanism.

Highly oriented pyrolytic graphite (HOPG) is a standard target used in surface physics, easy to clean and handle. It consists of well defined layered carbon sheets which exhibit large differences in electrical and thermal conductivity parallel to the layers (large) as compared to

the perpendicular direction (low), see also chapter I 2.3. Since electron transport in a conductor is related to conductivity, we expected to find electron emission depending on the orientation of the layers with respect to the surface. In this way we hoped to study the role of electron transport in KE isolated from the primary excitation mechanism, which we expected to be independent from the target orientation (see discussion).

This chapter describes our quest to find evidence for such orientation dependent effects in KE.

I.6.2   Experimental Setup

We have measured electron emission yields induced singly charged C^+, N^+, O^+, Ar^+ and Xe^+ ions (impact energy between 3 and 10 keV) on clean HOPG of two different orientations. The HOPG target (tectra [51], size: 12x12x8 mm) has a thermal and electrical conductivity (see tab. 2.1) which are considerably higher along the graphite layers (so called "HC" side) than perpendicular to them (so called "LC" side) [51, 52]. In our measurements we have compared total KE yields for HC and LC orientation of the HOPG target (see chap. I 2.3 and I 2.4).

An ECR ion source [48] has been used to produce the projectile ions (chap. I 2.2). Experimental methods for KE measurements were the same as in our earlier investigations with atomically clean polycrystalline gold [46] and HOPG [59, 60], i.e. the total electron yield Y was obtained from currents of impinging ions and emitted electrons (see chapter I 2.1). In a first series of experiments the ion impact took place normal to the surface and then in further measurements under $0 = 45°$ impact angle.

Both targets were prepared by cleaving the surface with an adhesive tape just before the targets are introduced into vacuum. Measurements were carried out under ultra-high-vacuum (UHV) conditions (typ. 10^{-10} mbar). Before taking data, the HOPG targets were sputter-cleaned by impact of 5 keV Ar^{2+} ions.

Total experimental errors for our yields depend on the absolute value of projectile ion currents as well as on the KE yields themselves which decrease for lower impact energy. Total errors were estimated to about $\pm$ 13 % at 4 keV and $\pm$ 10 % at 10 keV impact energy [66].

I.6.3   Experimental Results and Discussion

Figs. 6.3.1 - 6.3.5 show our measured electron emission yields γ vs. ion impact velocity v for normal impact of C^+, N^+, O^+, Ar^+ and Xe^+ on atomically clean surfaces of HOPG oriented in the HC- and in the LC-direction, see respectively insert. All measured yields increase practically linearly with projectile velocity v. If one extrapolates this trend to zero yield the resulting intersection with the velocity axis ("apparent threshold velocity") is located around 8×10^4 m/s for C^+, N^+ and O^+ ions. The threshold velocity of the heavier projectiles Ar^+ and Xe^+ is somewhat smaller (around 6×10^4 m/s). In all cases within our experimental errors this threshold velocity was independent of the target orientation.

We expect a negligible influence of potential emission for a HOPG target with the here applied singly charged projectile ions [25], an assumption supported by the rather well defined KE thresholds [26, 27]. The KE threshold projectile velocity v_{th} for binary encounters of projectile ions with a quasi-free electron gas target is given by eq. (1.1) in chapter I. I [26]. For a clean graphite surface the work function is of the orders of $W_\phi = 5$ eV and the Fermi-energy is about $E_F = 21.3$ eV [79]. This results in a threshold velocity of $v_{th} = 1.52 \times 10^5$ m/s. The measured v_{th} values are somewhat lower than predicted by eq. (1.1). This disagreement between calculated and measured v_{th} values probably results from the real band structure of HOPG which deviates from the quasi-free electron metal case assumed in eq. (1.1), and from possible additional KE mechanisms as discussed in chapter I 3.2.

The total electron emission yield for 5 keV C^+ (fig. I.6.3.1) is 1.08 ($\pm$ 13 %) for HC-HOPG and 0.77 ($\pm$ 13 %) for LC-HOPG (increase of 40 %, see fig. I.6.3.6). The electron yield for HC-HOPG induced by O^+ ($E_{kin} = 10$ keV) is also 44 % higher than for LC-HOPG (fig. I.6.3.3). For N^+ ($E_{kin} = 10$ keV) (fig. I.6.3.2) there is a difference of 26 % between the two target orientations. Interestingly, for Ar^+ and Xe^+ we measure a smaller yield difference between HC- and LC-HOPG (e.g. at 5 keV 6 % for Ar^+ and 22% for Xe^+, see figs. 6.3.4 and 6.3.5).

In Fig. I.6.3.6 we have plotted the ratio of measured electron yields between HC- and LC-orientation vs. impact velocity v for normal ion impact.
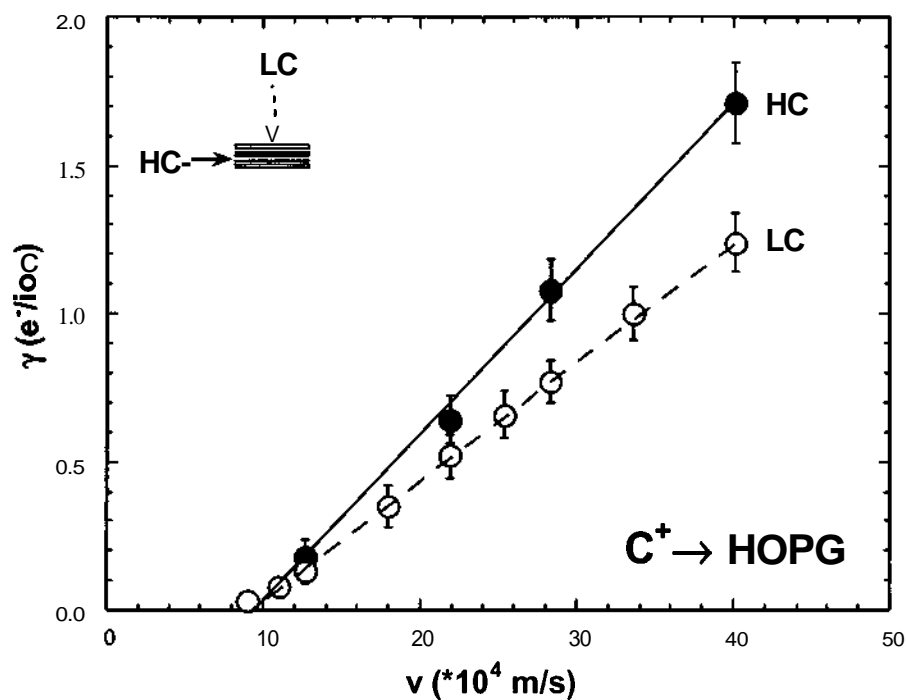
Fig. I.6.3.1: *Total electron yields for impact of* C^+ *on HC-HOPG (full circles) and LC – HOPG (open circles) vs. impact velocity v.*
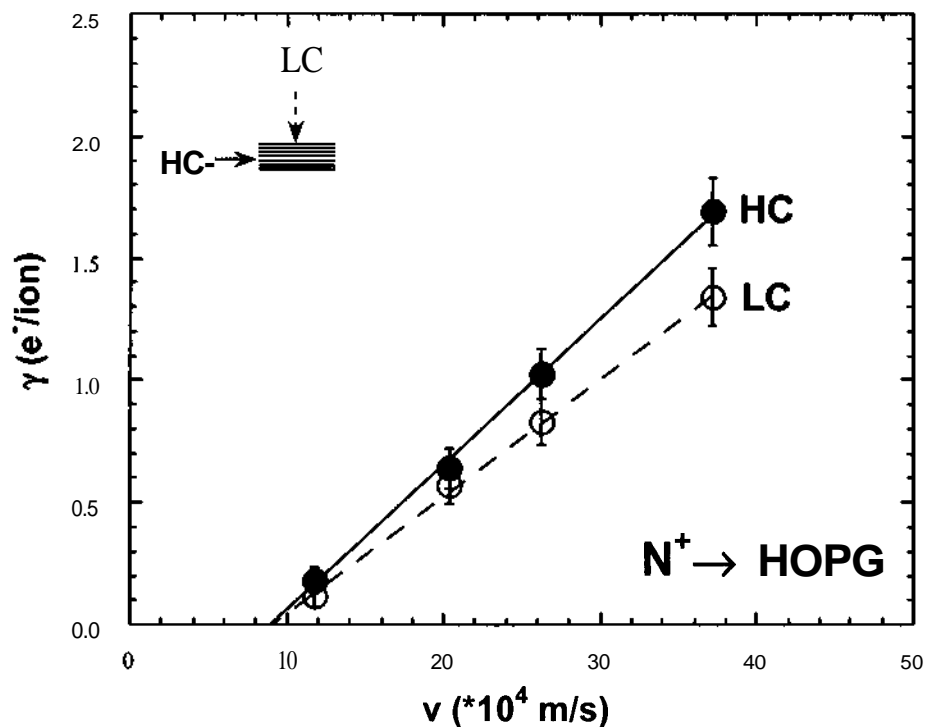

Fig. I.6.3.2: *Total electron yields for impact of* N^+ *on HC – HOPG (full circles) and LC – HOPG (open circles) vs. impact velocity v.*

Fig. I.6.3.3: Total electron yields for impact of O^+ on HC - HOPG (full circles) and LC -- HOPG (open circles) vs. impact velocity v.

Fig. I.6.3.4: Total electron yields for impact of Ar^+ on HC - HOPG (full circles) and LC-- HOPG (open circles) vs. impact velocity v.
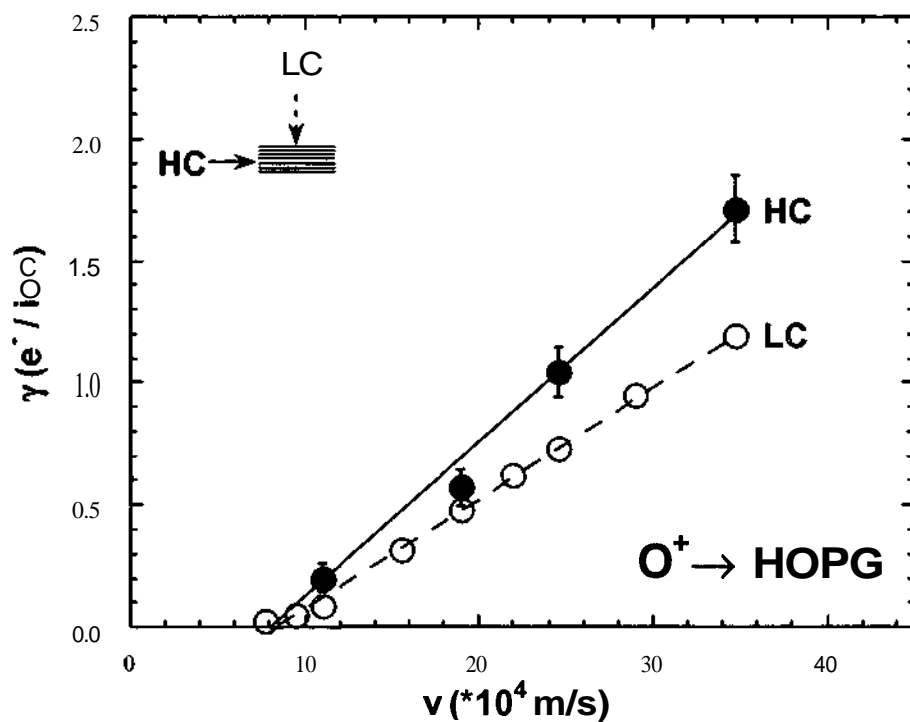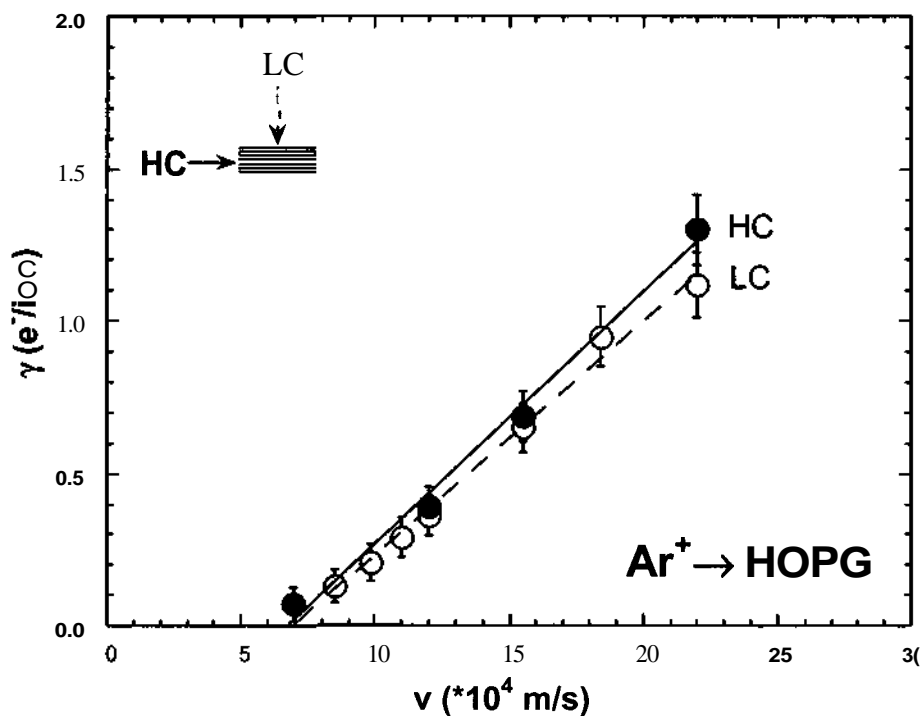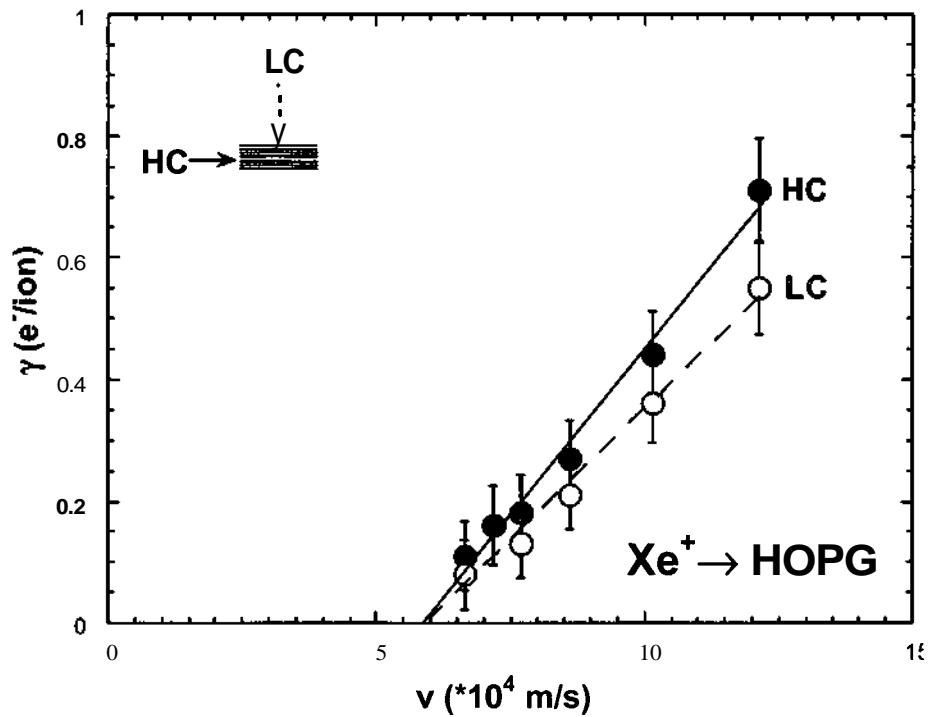
Fig. I.6.3.5: Total electron yields for impact of Xe^+ on HC – HOPG (full circles) and LC – HOPG (open circles) vs. impact velocity v.

In summary, this comparison shows the following qualitative trends:

(a) KE threshold velocities are practically the same for HC- and LC-HOPG.

(b) At any impact velocity the KE yields are higher for HC-HOPG than for LC-HOPG.

(c) For heavier projectiles the KE yields are less increased than for light ions

All these observations would be consistent with the behaviour of two targets (HC and LC-HOPG) which only differ in their electron transport characteristics:

(a) The identical threshold velocity points to identical primary excitation mechanism(s) (minimum energy necessary to excite electrons above the vacuum level)

(b) For the HC orientation the electron transport towards the surface is increased so that electrons originating from deeper layers will still be able to reach the surface, which results in a higher emission yield.

(c) At a few keV impact energy the heavier projectiles are stopped closer to the surface than lighter ones (e.g., according to TRIM calculations [10] 3 keV Ar+ ions have a range of 48 nm in carbon compared to 81 nm for 3 keV C^+ ions), resulting in a less pronounced influence of electron transport on the measured yield.

But before making these conclusions, let us consider some other possibilities for the observed yield differences.

For example, some channeling effect for ions travelling parallel to the graphite layers (HC orientation) could result in a different ion penetration depth. If this is the case, however, we would expect a smaller electron emission yield for HC than for LC case, in contrast to our observations.

Considering the roughness of the target surface, it may have an important influence on the total electron emission. For a perfectly flat surface one would expect that changing from normal ion impact ($0 = 0°$ with respect to nominal normal impact) to an inclined impact direction considerably increases the total electron emission yield (according to [5] roughly by $\cos^{-1}(\Theta)$). At a "nominal" normal incidence y is expected to be much higher on a rough surface (i.e. some statistical distribution of impact angles $0 > 0$) than on a perfectly flat one. To check this point we have also measured the electron emission yield from HC-HOPG and LC-HOPG by ions impinging under $0 = 45°$.

Fig. I.6.3.7 show the ratios of $\gamma_{45°}$ (nominal ion impact angle 45°) to $\gamma_\perp$ (nominal normal impact) for LC-HOPG induced by C^+, N^+, O^+ and Ar^+. For C^+ and O^+ a ratio close to $\cos^{-1}(45°) = 1.41$ is obtained. For the other ions the increase from normal to 45° impact is about 20%.

In fig. I.6.3.8 we show the ratios $\gamma_{45°}/\gamma_\perp$ for HC-HOPG bombarded by C^+, N^+, O^+ and Ar^+ ions. Values between 0.96 and 1.16 indicate that the HC oriented surface is comparably

rough, while the LC surface is almost flat. Inspection with a light-optical microscope (fig. I.6.3.9a,b and fig. I.6.3.10a,b) and electron microscope (fig. 6.3.9c and 6.3.10c) supported this conclusion. Cleaving with an adhesive tape, although known to produce nicely flat surfaces for LC-HOPG (fig. I.6.3.9a-c), obviously leaves an HC-HOPG (fig. I.6.3.10a-c) surface quite rough.

We therefore have to conclude that the surface roughness of HC-HOPG could have masked a possible electron transport dependence of the measured electron emission yields
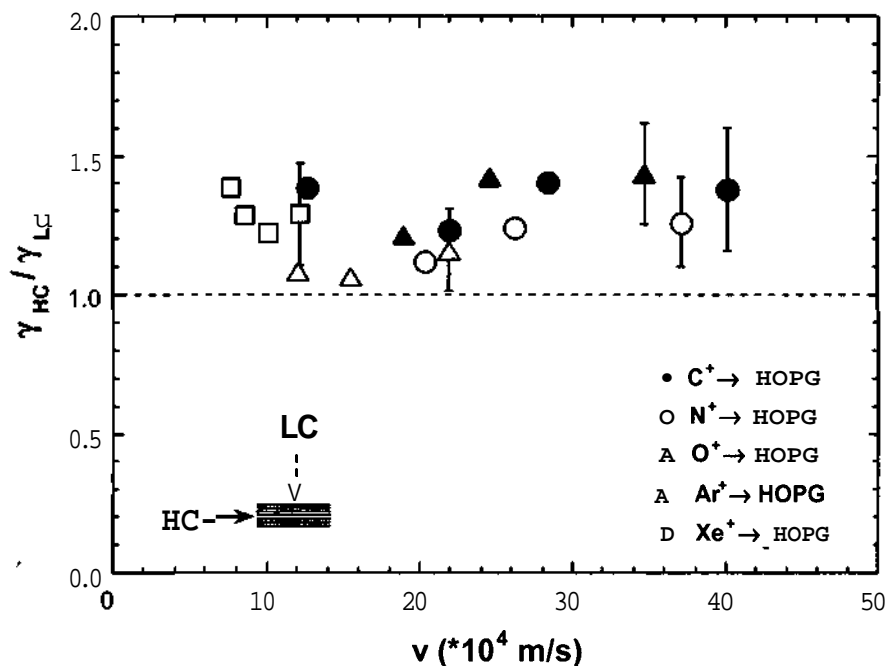
Fig. I.6.3.6: Ratio of the total electron emission from HC-HOPG to LC-HOPG vs. impact velocity v for normal impact of C^+ (filled circles), N^+ (open circles), O^+ (filled triangles), Ar^+ (open triangles) and Xe^+ (filled reversed triangles) ions.
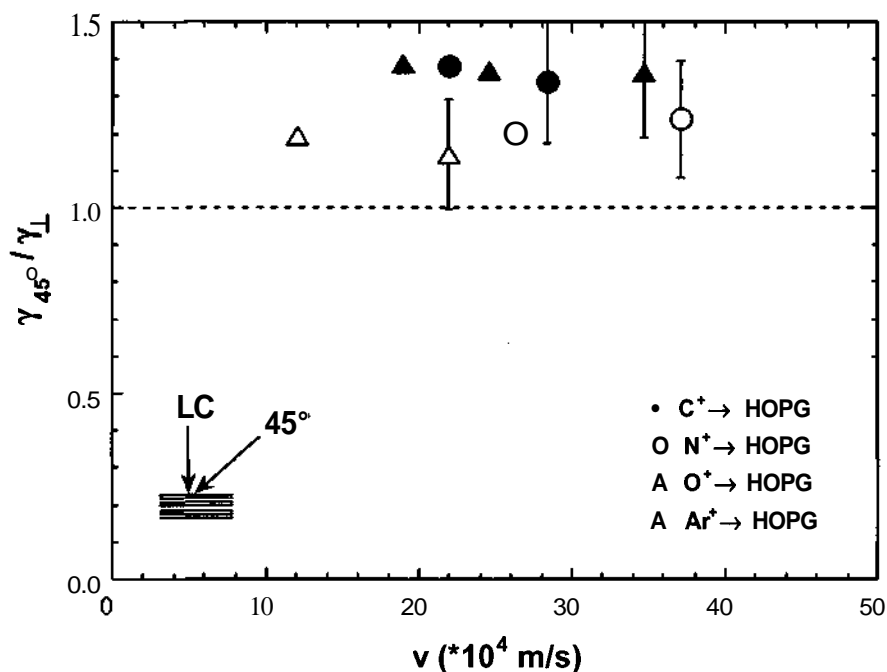

Fig. I.6.3.7: Ratio of $\gamma_{45°}$ (impact angle = 45°) to $\gamma_\perp$ (normal incidence) from LC-HOPG induced by C^+ (full circles), N^+ (open circles), O^+ (full triangles) and Ar^+ (open triangle).

Fig. I.6.3.8: Ratio of $\gamma_{45°}$ (Impact angle = 45°) to $\gamma_\perp$ (normal incidence) from HC-HOPG induced by C^+ (full circles), N^+ (open circles), O^+ (full triangles) and Ar^+ (open triangle).
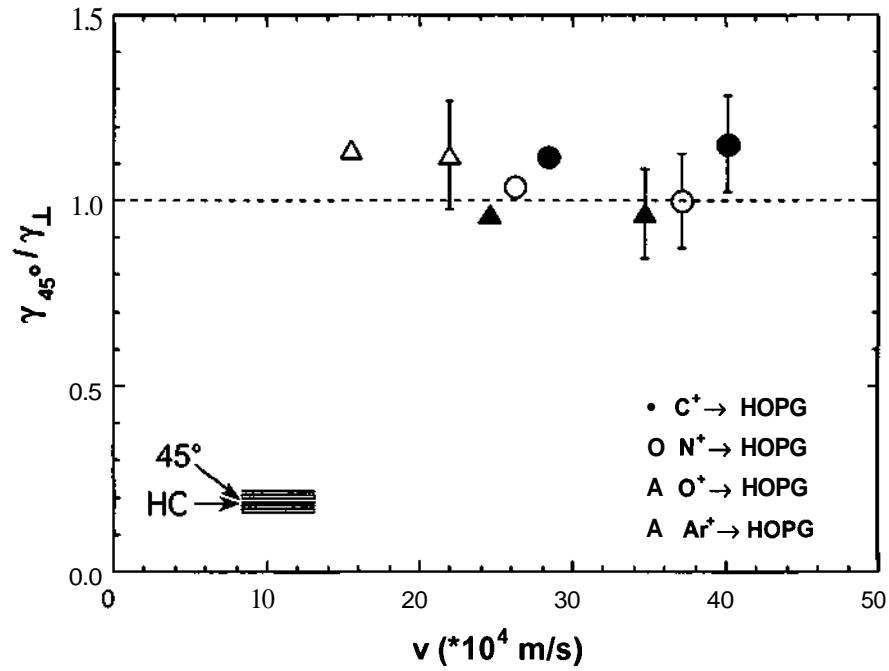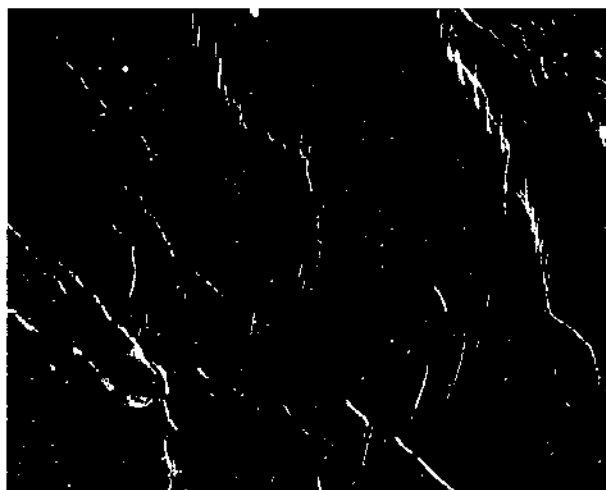
Fig. I.6.3.9a

Fig. 6.3.9b

Fig. I.6.3.9C

Fig. II.3.3.9: The LC-HOPG-surface used in our studies as seen by using a light-optical microscope (image size of 20x30 mm (a) and 1×2 mm (b)) as well as in an electron microscope (image size of 250x250 μm (c)).
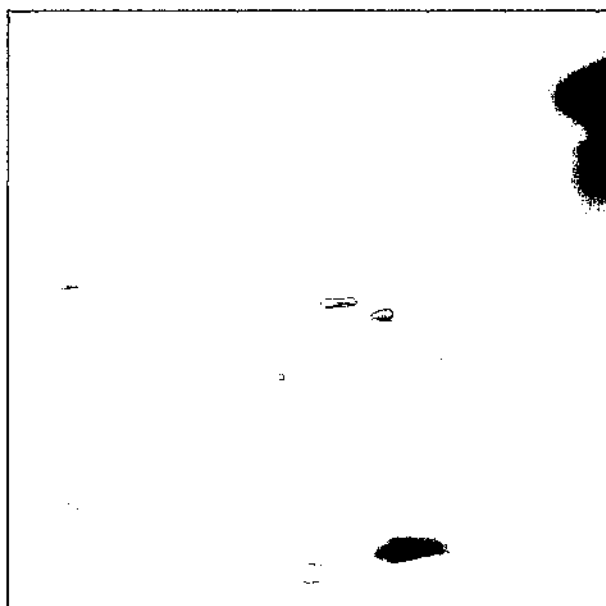
Fig. I.6.3.10a

Fig. I.6.3.10b

Fig. I.6.3.1Oc

Fig. I.6.3.10: The HC-HOPG-surface used in our studies as seen by using a light-optical microscope (image size of 20×30 mm (a) and 1×2 mm (b)) as well as in an electron microscope (image size of 250×250 μm (c)).
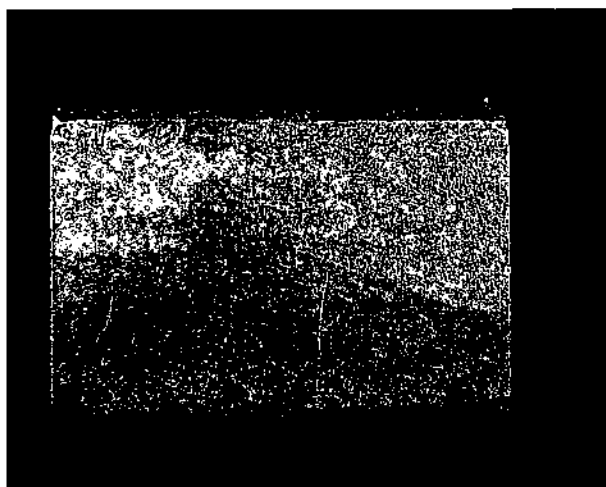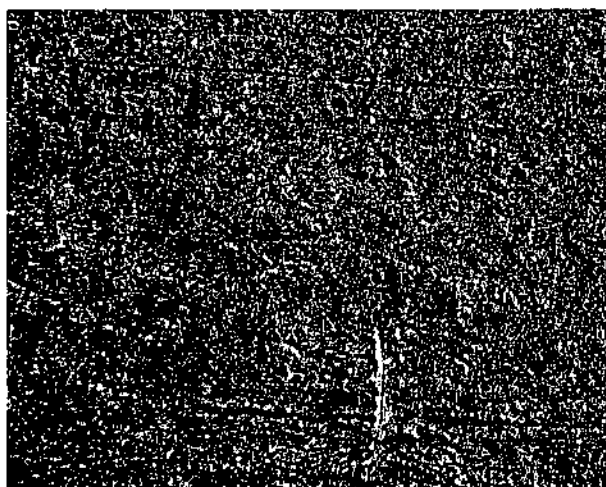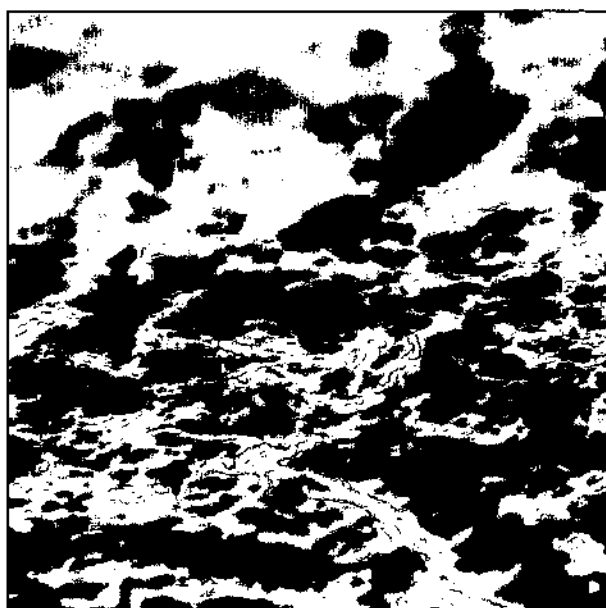
I.6.4   Summary

We have investigated total electron yields induced by impact of C^+, N^+, O^+, Ar^+ and Xe^+ ions ($E \leq 10$ keV) under normal and 45 degree incidence on clean highly-oriented pyrolytic graphite (HOPG) with two different orientations, one exhibiting high (HC) - and the other one low thermal and electrical conductivities (LC). We expected different KE yields for HC- and LC-orientation. Indeed, measured KE yields for the high conductivity side of HOPG were up to 40% larger than for the low conductivity side. To check the influence of roughness of the two surfaces we have also performed measurements for 45° impact angle. Results of these measurements indicate that the HC-HOPG oriented surface is comparably rough while the LC-HOPG surface is rather flat. A possible transport dependence of the measured electron emission yields is therefore largely out weighted by the different surface roughness.

PART II

AFM/STM search for slow MCI - produced nanodefects on surfaces

II.1 Introduction

First experimental work on charge-state dependent sputtering of insulators by HCI has been carried out in Tashkent/Uzhbekistan [80, 81], from which it was concluded that for impact of Ar^{q+} ions (q < 5) on silicon and alkali halide surfaces secondary ion yields increased rapidly both with the incident ion charge and for decreasing impact energy. Etching patterns on a KCl surface previously bombarded with equal fluxes of slow Ar^{q+} and Kr^{q+} ions were larger for higher q [82]. In ref. [83] it was claimed that for bombardment of Si with singly charged ions sputter yields are larger by more than a factor of two than with neutral projectiles of equal mass and energy. However, for 20 keV Ar^{q+} (q < 9) impact on a Si surface only the secondary ion yield increased noticeably with q, whereas the respective total sputter yields (dominated by ejection of neutral Si atoms) did not change with q [84]. This apparent contradiction to [83] was explained with a different conductance of the Si samples.

AFM (atomic force microscopy) on mica samples irradiated with low fluences of very highly charged ions (e.g. Xe^{44+} and U^{70+}) revealed single-ion induced blister-like defects, the size of which increased with the incident ion charge beyond a certain charge state "threshold" at around q = 30 [85]. These measurements have been performed at comparably high impact energies (several hundred keV), but were repeated later at somewhat lower kinetic energies (100 keV) [86] with the same results. For bombardment of SiO_2 with Xe^{q+} (q < 44) and Th^{q+} (q ≤ 70) at similar kinetic energy as in ref. [85] (see fig. II.1.1), TOF spectra of ejected positive and negative secondary ions were dominated by single-atomic species, but also molecular clusters could be observed [87]. Again, the yields increased in proportion to the incident ion charge above a "threshold" of about q = 25. Secondary ion yields were made absolute by taking into account the acceptence solid angle and efficiency of the applied TOF system, resulting in, e.g., total yields of 25±12 for positive and 5±2.5 for negative secondary ions from impact of Th^{70+}, respectively. These remarkably high values suggested that the total sputtering yields (i.e. including neutrals) must be significantly larger than the known kinetic sputtering yield of about 2.5 target particles for impact of 500 keV singly charged Th ions [87]. Further work performed under similar conditions but using a catcher foil technique for measuring the total sputtering yield showed that also GaAs- and UO_2 - surfaces are much more efficiently ablated by HCI like Th^{70+} than expected from the involved kinetic projectile energy [18].

A different set of results stems from HCl-induced proton sputtering from "dirty" (i.e. untreated, hydrocarbon-covered) surfaces. The proton sputtering yields show a remarkably strong dependence on ion charge q, ranging from $\sim q^3$ in the kinetic sputtering regime [88, 89] to $\sim q^5 - q^6$ in the pure potential sputtering regime [90, 91]. In addition, a relatively high yield of about one proton per incident highly charged ion (q = 20) was measured. An enhancement in secondary ion emission yield with primary ion charge state has recently even been claimed for thin "conducting" carbon foils [92]. However, the fact that in these experiments almost exclusively hydrocarbon ions, protons, and H- were detected, points to sputtering from an insulating hydrocarbon overlayer rather than from the conducting amorphous carbon foil.
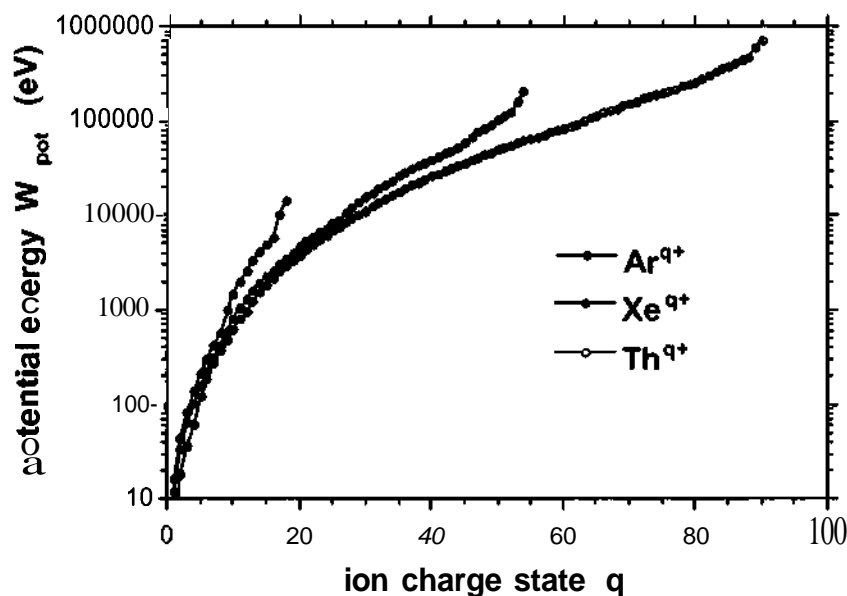

Fig. II.1.1: Total potential energy $W_{pot}(q)$ of multiply charged Ar^{q+}, Xe^{q+} and Th^{q+} ions vs. charge state q.

No firm conclusions can be drawn on the total sputter yield from such secondary ion emission measurements. On the other hand, accurate determination of the total sputter yields (including both neutral and ionized secondary particles) has been performed by means of a sensitive quartz crystal micro-balance technique developed at TU Wien [93, 94]. Measurements have been carried out for impact of Ar^{q+} (q < 14) and Xe^{q+} ions (q < 28) on various surfaces [20, 21, 95]. For conducting surfaces no q-dependent total sputter yield was observed (only kinetic sputtering [96, 97]), while for alkali halide and some other insulating surfaces a sizeable sputtering yield could be observed down to very low impact energies (≥ 5 x q eV) [20, 21, 95], which increased dramatically with the potential energy carried by the projectile, leading to neutral sputtering yields as high as several hundred target particles per single ion impact.

Within this theses systematic search was carried out for potential sputtering (PS) with atomically clean monocrystalline insulator targets which have been bombarded by low-energetic ions on the single impact level, by searching for resulting surface defects by means of AFM. The targets remained under UHV conditions during ion irradiation and subsequent AFM inspection. Interesting applications of PS as, e.g., nanostructuring of insulator surfaces, have been an important motivation for this study [98]. There have also been suspicions that earlier PS studies involving polycrystalline insulator films might have been influenced by some defects in these target samples.

II.2 Experimental Setup

The goal was to find nanodefects on freshly prepared surfaces of LiF(100), SiO2(0001) α-quartz, muscovite mica, sapphire c-plane $Al_2O_3(0001)$ and HOPG after their irradiation with low doses of slow singly and multiply charged ions. The ion bombardment was accompanied by low-energy electron flooding to compensate for surface charge-up which otherwise would have strongly inhibited the AFM observation. The applied electron gun produced very slow electrons (4 eV energy, 200 nA current, 2 cm distance to the sample).

In a first stage of this study we had used a NIER-type electron impact ion source with its turbomolecular pump directly attached to our UHV-AFM instrument [99]. However, in this arrangement inconveniently high AFM system noise was produced. We then changed to a transportable UHV vault (see chap. II 2.2) for target transfer, which is alternatingly coupled by UHV locks to the target irradiation chamber (see chap. II 2.1) and the AFM (see chap. II 2.3). This procedure kept target surfaces under permanent UHV conditions after their initial cleaning, thermal annealing and subsequent irradiation until completion of their AFM inspection, and also drastically reduced the disturbing AFM system noise. Singly- and multiply charged ions for target irradiation have been extracted from a 5 GHZ ECR ion source (see chap. I 2.2) [49], magnetically analyzed and guided via electrostatic lenses to the UHV irradiation chamber. The ions were decelerated in front of the target surface to their desired impact energy.

II.2.1   The Experiment AIDA

The irradiation experiment of the different target materials were carried out within the ultra-high vacuum (UHV) experiment AIDA (Anlage zur ioneninduzierten Desorptionsanalyse) at TU Wien [1].

The gas pressure in the ion-source is rather high (up to 10^{-5} mbar), UHV in the target area of AIDA can only be accomplished with several differentially pumped chambers spatially separated by small apertures. Assuming a vacuum pressure in the range of 10^{-6} mbar in the beam line after the ion source, the pressure in the pre-jar is of the order of 10^{-8} mbar and in the target chamber of AIDA the pressure is in the range of some 10^{-10} mbar.

connection
to ion beam

valve

bellow

einzellens

deflection plates

removable Faraday cup

pre-jar

insulating break

apertures

deflection plates

deceleration lens

electron gun

target / Faraday cup
on manipulator

Auger analyser

sputter gun

quadrupol analyser

window
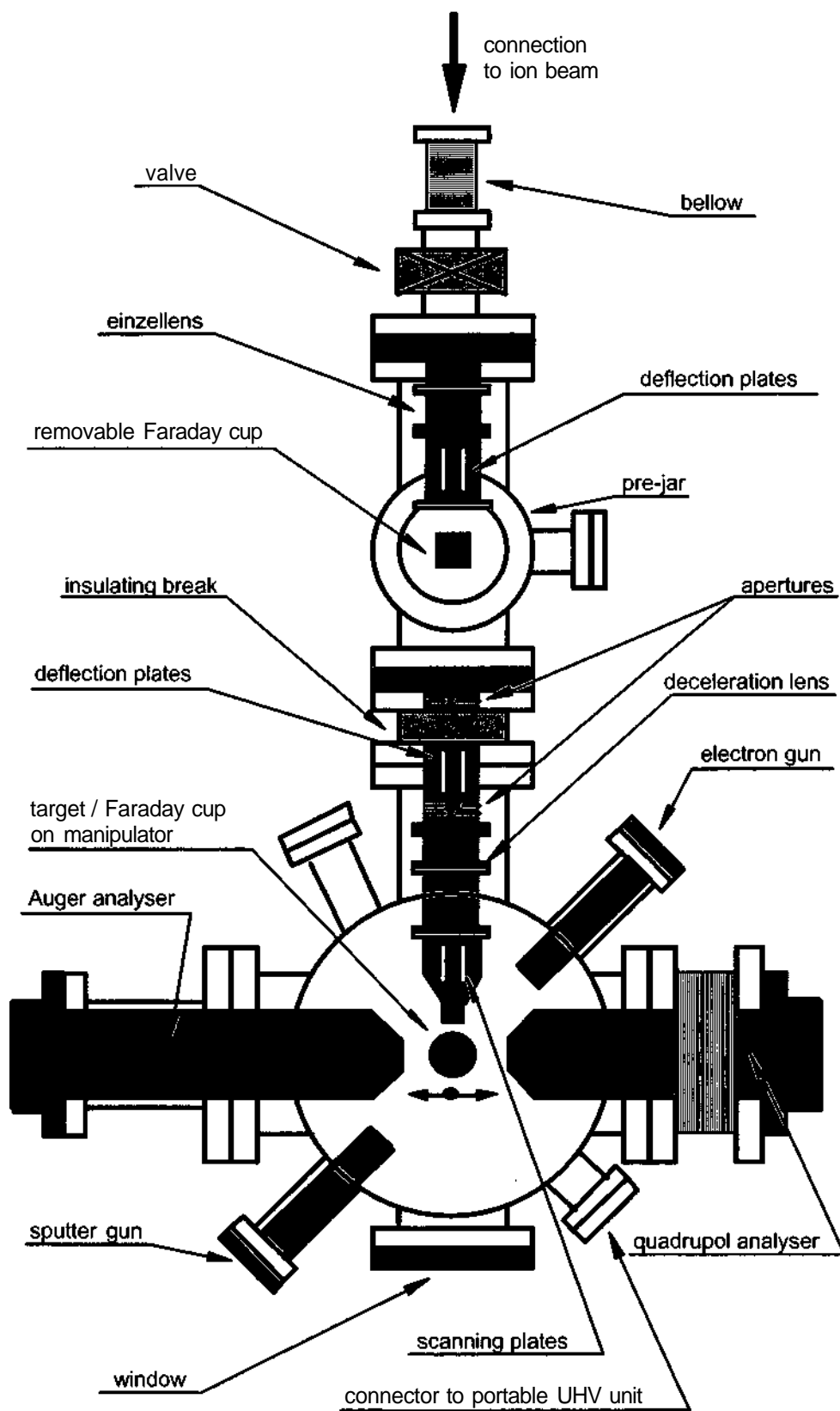
scanning plates

connector to portable UHV unit

Fig. II.2.1.1: The experimental setup AIDA.

Fig. II.2.1.1 shows the experimental setup for the irradiation experiments. An electron flood gun and an ion gun can be used for stand-alone experiments. Two lenses and two pairs of deflection plates transport, decelerate and direct the ion beam towards the target area. To ensure a homogenous ion irradiation of the whole target area (1 cm^2) the ion beam is scanned by means of electrostatic plates with a typical frequency of 1.4 kHz. Fig. II.2.1.2 shows a detailed sketch of the second lens system with deflection- and scanning plates. Four cylindrical lenses are used to decelerate the ion beam to the desired kinetic energy and to re-focus the decelerated ion beam.

Special attention was paid to correct current measurements of multiply charged ion beams. To minimise loss of secondary electrons from the Faraday-Cup (FC), we used a FC with a deep drilling and a small pinhole aperture (0.3 mm^2). Ion current test measurements with and without bias voltage supplied to the FC show no difference which assures correct ion current measurement.

The target holder is mounted on a UHV manipulator, which allows a displacement of the target in x-y-z direction and rotation by 360°. The target holder is equipped with a filament heating (up to 400 °C) and two thermocouples for temperature measurements.

To reach small impact energies the ion beam has to be decelerated. When using the experimental setup at the ion source (cf. sect. I 2.2) this is achieved by biasing the whole target chamber including electronics with the necessary deceleration voltage. An isolating break between the pre-jar and the target chamber provides the galvanic separation to the beam line.
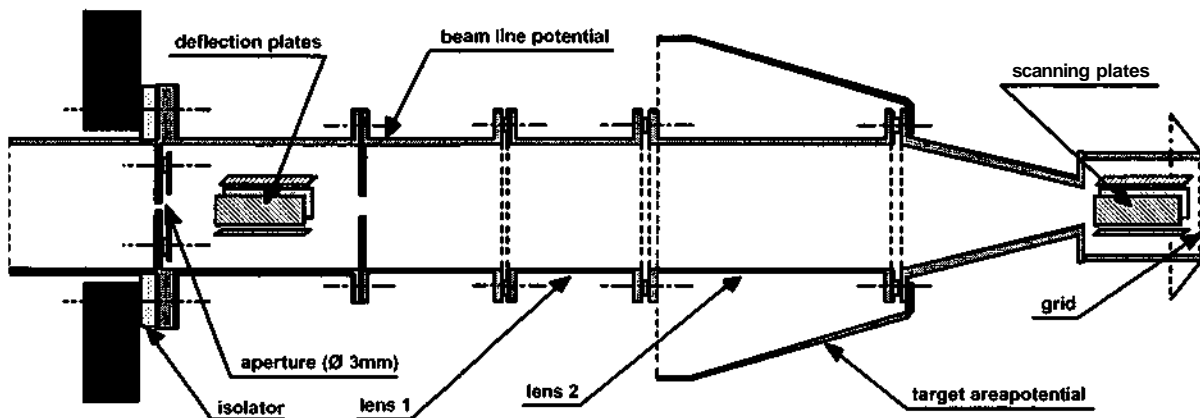

Fig. II.2.1.2: Sketch of the lens in front the target area.
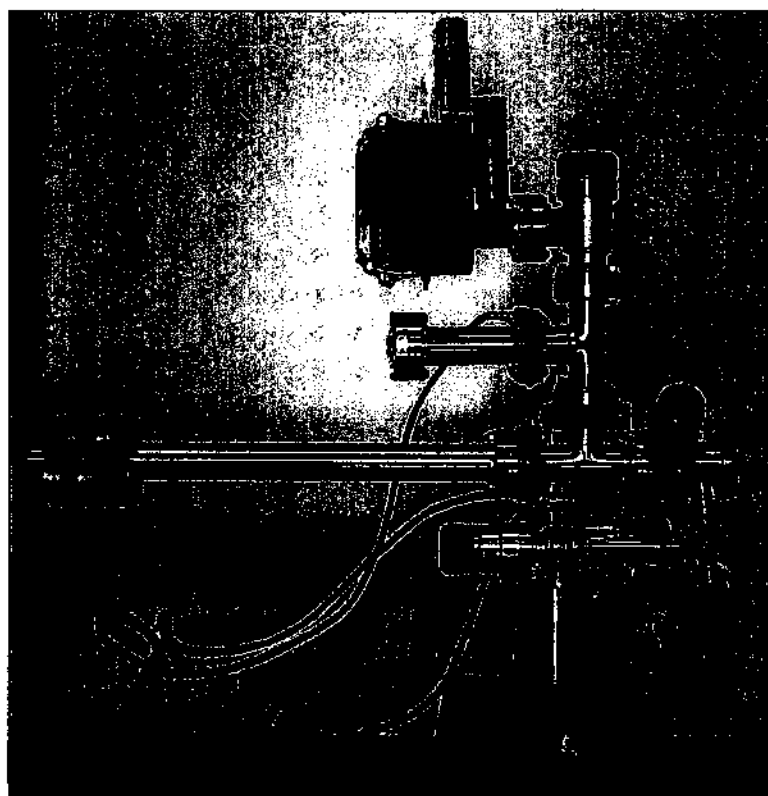
II.2.2   Transportable UHV Vault

This chapter describes in particular the transportable UHV vault, which was used to transport the samples from AIDA to the STM/AFM.

To assure clean surfaces we constructed a UHV suitcase for transportation of samples from AIDA to the STM/AFM in UHV. Fig. II.2.2.1 shows a schematic drawing and in fig. II.2.2.2 a photo of the transportable UHV Vault is presented. The connection to both AIDA (cf. fig II.2.2.1) and the STM/AFM is realized by a CF 35 connector flange. The transportable UHV vault is first connected to AIDA then evacuated by the turbo pump and baked for a day. When reaching UHV, the ion getter pump is switched on and the valve to the main chamber is opened for moving the sample into the target area. When the irradiation experiment has finished, the sample is manipulated back into the vacuum suitcase and the valves to the turbo pump and the main chamber are closed. The ion getter pump is connected to a portable Pb accumulator (13.7 V, 1.1 Ah), which operates the ion pump for at least two hours. After transport and connection to the STM/AFM facility, the small volume between the two valves has to be pumped by the turbo pump for one hour before the valves can be opened and the sample can be moved into the STM/AFM chamber for analysis.

The transportable UHV vault allows transportation of samples at vacuum pressures in the range of 5×10^{-9} mbar. A target holder for the different samples was constructed (see fig. II.2.2.3). The samples are mounted on a stainless steel plate by means of a steel welt. One side of the target plate was equipped with a handle for catching it with the wobble stick. Precise manipulation within the vacuum chamber is possible due to multidirectional movement of the manipulator of AIDA. The target holder itself is equipped with a filament heating to clean the surface of the HOPG samples before ion bombardment.
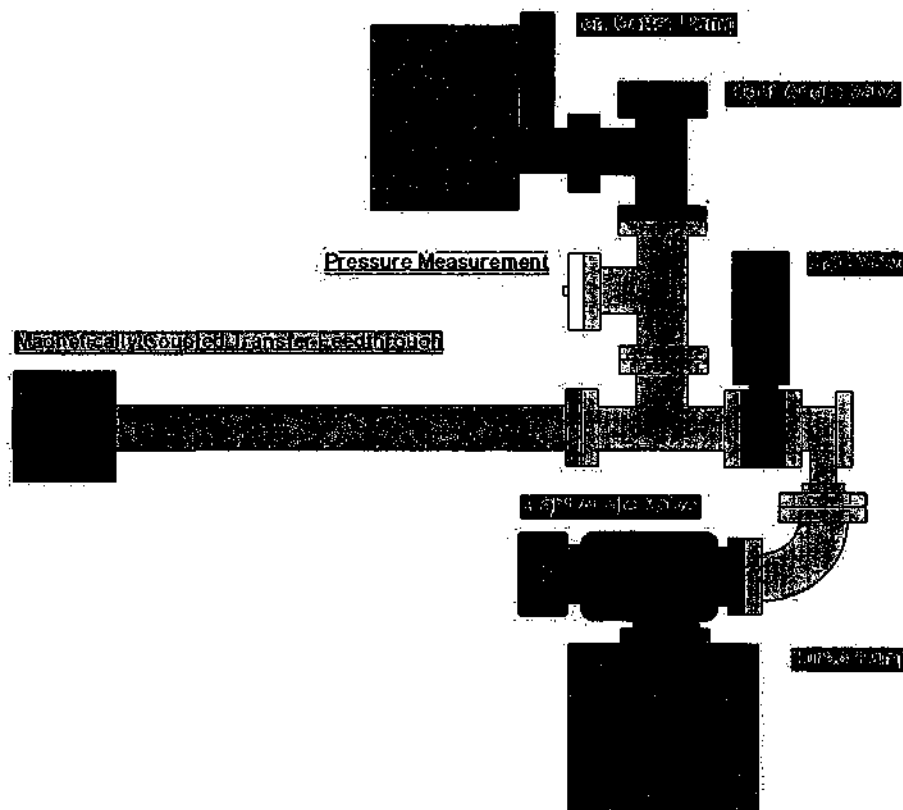
Fig. II.2.2.1: The UHV transfer station consists of an ion getter pump, a turbo pump, a gate valve and a magnetically coupled transfer feedthrough. It allows for sample, tip and cantilever transfer without braking the vacuum in the microscope chamber.

*Fig.II.2.2: Photo of the transportable UHV vault.*
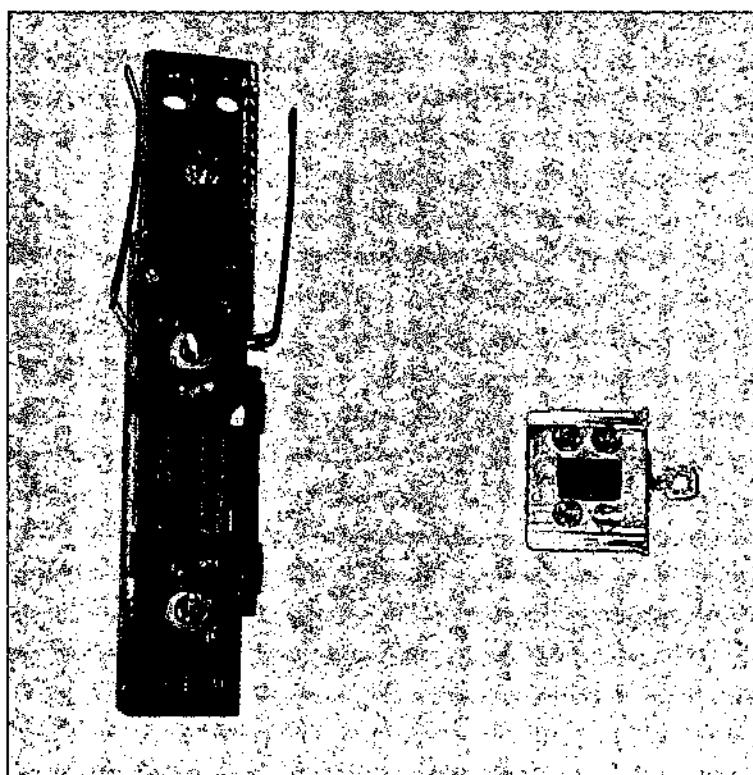
Fig. II.2.3: Photo of the target holder of the AIDA experiment (left side) and the HOPG target (right side).

II.2.3   STM/AFM Microscope

The scanning tunneling microscope (STM) was invented in 1981 by Gerd Binnig and Heinrich Rohrer at IBM Zurich. Five years later they were awarded the Nobel prize in physics for its invention. The STM was the first instrument to generate real-space images of surfaces with atomic resolution.

The STM uses a sharpened, conducting tip with a bias voltage applied between the tip and the sample (see fig. II.2.3.1). When the tip is brought within about 10 Å of the sample, electrons from the sample begin to "tunnel" through the 10 Å gap into the tip or vice versa, depending upon the sign of the bias voltage (see also fig. II.2.3.2). Resulting tunneling current varies with tip-to-sample spacing, and this signal is used to create a STM image. For tunneling to take place, both the sample and the tip must be conductors or semiconductors.
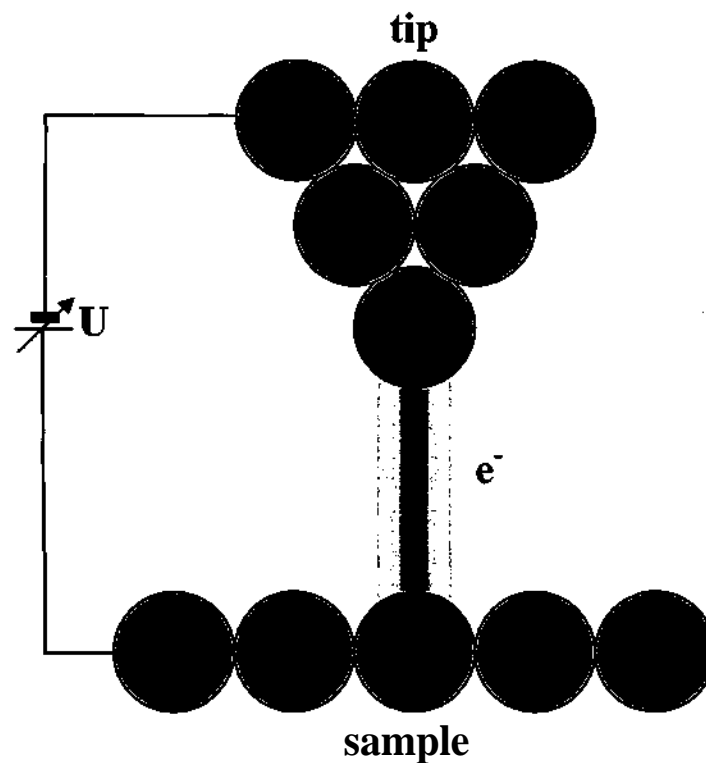
Fig. II.2.3.1: Electrons from the sample begin to "tunnel" through the gap into the tip or vice versa, depending upon the sign of the bias voltage.

Tersoff et al. [100] showed that the tunneling current is proportional to:

a)   the density of states (DOS) near the Fermi-edge

b)   the tunnelling voltage U between the STM tip and sample

c)   the tunnelling probability $e^{-2\kappa d}$

$$\kappa = \sqrt{\frac{2mW_\phi}{\hbar}}$$

d - distance between tip an sample
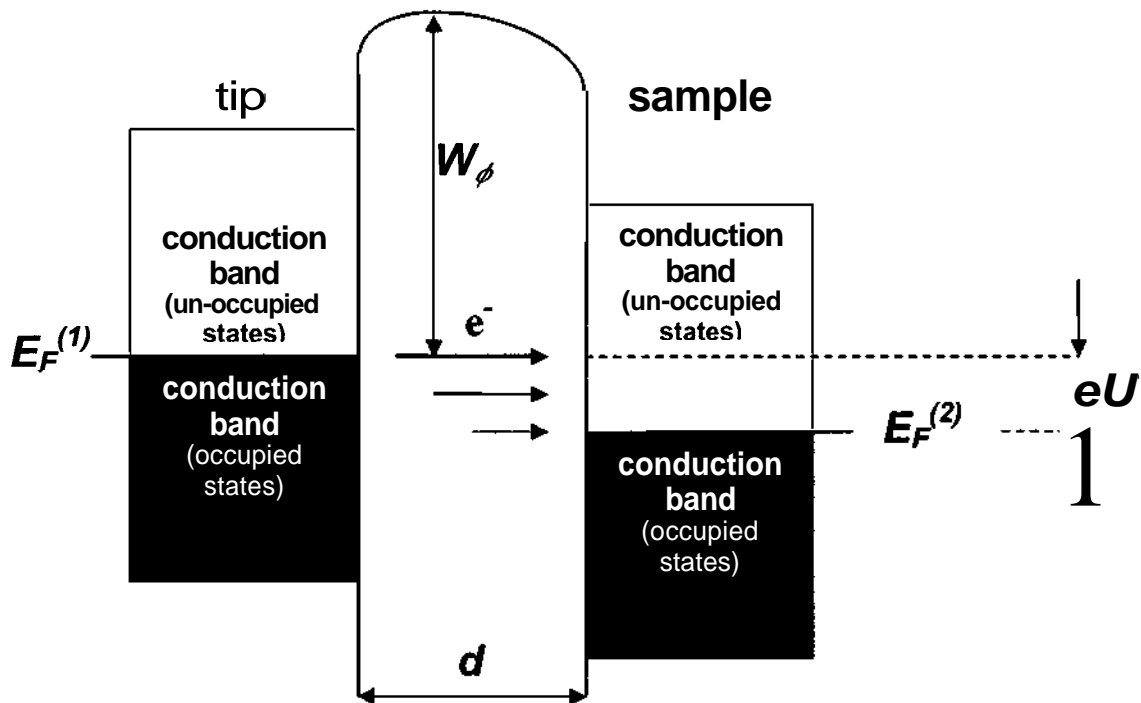
m - electron mass

W_ϕ -   work function

Fig. II.2.3.2: A positive sample voltage U causes an increased tunnelling current due to the shifted un-occupied states of the sample.

STMs can be designed to scan a sample in either of two modes: 1) *constant-height-mode*

                                                                  2) *constant-current-mode*

In *constant-height mode,* the tip travels in a horizontal plane above the sample and the tunneling current varies depending on topography and the local surface electronic properties of the sample. The tunneling current measured at each location on the sample surface is proportional to the surface density of states.

In *constant-current mode,* the STM uses feedback to keep the tunneling current constant by adjusting the height of the scanner at each measurement point. For example, when the system detects an increase in tunneling current, it adjusts the voltage applied to the piezoelectric scanner to increase the distance between the tip and the sample.

The atomic force microscope (AFM) probes the surface of a sample with a sharp tip, a couple of microns long and often less than 100 Å in diameter. The tip is located at the free end of a cantilever that is 100 to 20 urn long. Forces between the tip and the sample surface cause the cantilever to bend, or deflect. A detector measures the cantilever deflection as the tip is scanned over the sample, or the sample is scanned under the tip. The AFM detects the position of the cantilever with optical techniques. A laser beam bounces off the back of the cantilever onto a position-sensitive photodetector (PSPD). As the cantilever bends, the position of the laser beam on the detector shifts. The PSPD itself can measure displacements of light as small as 10 Å. The ratio of the path length between the cantilever and the detector to the length of the cantilever itself produces a mechanical amplification. As a result, the system can detect sub-angstrom vertical movement of the cantilever tip. The measured cantilever deflections allow a computer to generate a map of surface topography. AFMs can be used to study insulators and semiconductors as well as electrical conductors. Several forces typically contribute to the deflection of an AFM cantilever. The force most commonly associated with atomic force microscopy is an interatomic force called the van der Waals force. The dependence of the van der Waals force upon the distance between the tip and the sample is shown in fig. II.2.3.3.

The AFM can be used in two distance regimes: 1) *contact regime;*

                                                 2) *non-contact regime.*

In the *contact regime,* the cantilever is held less than a few angstroms from the sample surface, and the interatomic force between the cantilever and the sample is repulsive. In contact-AFM mode (repulsive mode), an AFM tip makes soft "physical contact" with the sample. The tip is attached to the end of a cantilever with a low spring constant, lower than the effective spring constant holding the atoms of the sample together. As the scanner gently traces the tip across the sample (or the sample under the tip), the contact force causes the cantilever to bend to accommodate changes in topography. The magnitude of the total force exerted on the sample is in the range of 10^{-8} N.

The AFM can operate in one of two modes: a) *constant-height mode*

b) *constant-force mode.*

In *constant-height mode,* the spatial variation of the cantilever deflection can be used directly to generate the topographic data set because the height of the scanner is fixed as it scans.

In *constant-force mode,* the deflection of the cantilever can be used as input to a feedback circuit that moves the scanner up and down in z, responding to the topography by keeping the cantilever deflection constant. In this case, the image is generated from the scanner's motion. With the cantilever deflection held constant, the total force applied to the sample is constant.
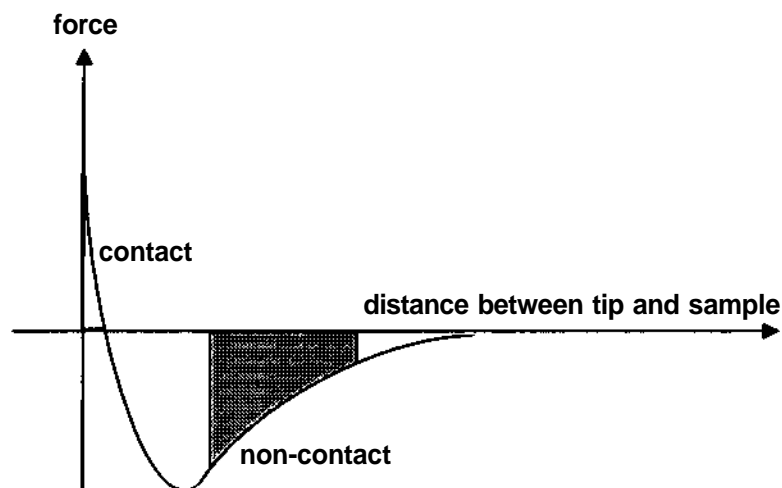

Fig. II.2.3.3: Interatomic force vs. distance curve

In the *non-contact regime,* the cantilever is held on the order of tens to hundreds of angstroms from the sample surface, and the interatomic force between the cantilever and sample is attractive (largely a result of the long-range van der Waals interactions). Non-contact AFM is a vibrating cantilever technique in which an AFM cantilever is vibrated near the surface of a sample. The spacing between the tip and the sample for non-contact AFM is on the order of tens to hundreds of angstroms. In non-contact mode, the system vibrates a stiff cantilever near its resonant frequency (100 to 400 kHz) with an amplitude of a few tens to hundreds of angstroms. Changes in the resonant frequency or vibration amplitude as the tip comes close to the sample surface can be detected. The resonant frequency of a cantilever varies as the square root of its spring constant. In addition, the spring constant of the cantilever varies with the force gradient experienced by the cantilever and the force gradient changes with tip-to-sample separation. Thus, changes in the resonant frequency of the cantilever can be used as a measure of changes in the force gradient, which reflect changes in the tip-to-sample spacing, or sample topography.

Like contact AFM, non-contact AFM can be used to measure the topography of insulators and semiconductors as well as electrical conductors. The total force between the tip and the sample in the non-contact regime is very low, generally about 10^{-12} N.

The specifications of our Omicron AFM/STM instrument:
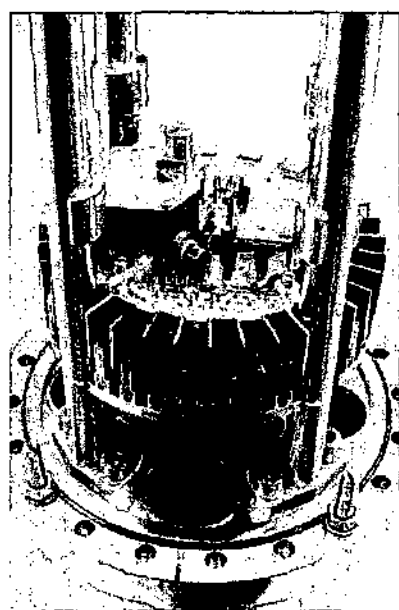
(1)	Contact and non-contact mode AFM, and STM lateral (friction) force detection
(2)	Electrostatic force imaging
(3)	Simultaneous AFM and STM detection
(4)	z-resolution: 0.01 nm
(5)	Force resolution: 3 pN
(6)	Frequency resolution: 0.5 Hz (frequency range 3 kHz - 1 MHz)
(7)	Resonance of spring suspension: ~ 1 Hz (eddy current damping)
(9)	vacuum achievable: 10^{-11} mbar range

II.2.4   Lithium Fluoride LiF (100)
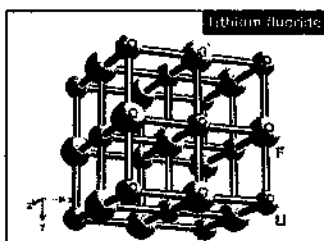
Lithium fluoride is a white crystalline solid with a melting point of 848°C, a boiling point of 1676°C and a density of 2640 kg/m^3. LiF has cubic structure (NaCl structure), the lattice parameter is 0.2008 nm at room temperature

Standard single crystal preparation technique:

atomically clean monocrystalline surfaces of LiF are produced by cleavage of (100) single crystals (TBL Kelpin, Germany) via our home-built "guillotine": an aluminum block which has a tunnel in the diameter of the single crystal. The single crystal is inserted into the tunnel, and through a cleft in the metal block, with the help of a hammer, a razor blade - mounted into a frame which prevents the blade to completely cut the crystal - is used to cleave the crystal. By using the guillotine we could drastically reduce the number of involuntarily broken crystals due to cleavage problems. After cleavage, LiF single crystals are CO_2 snow cleaned, transferred to the vacuum chamber and annealed at 400°C for three hours (fig. II.2.4.1). CO_2 snow cleaning is a very efficient way to remove micro- and nanometer sized debris from the single crystal surface. During Ar ion bombardment, an electron gun is used to compensate for surface charges (see also chapter II.2.1). The electron energy is chosen small enough not to cause any surface damage (about 5 eV). We obtain monoatomic terraces and atomic resolution in AFM contact mode.
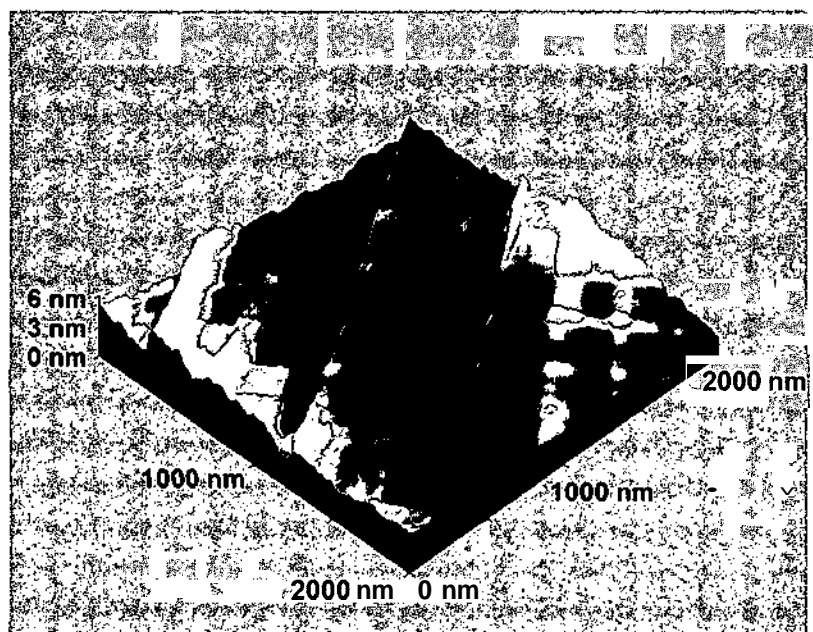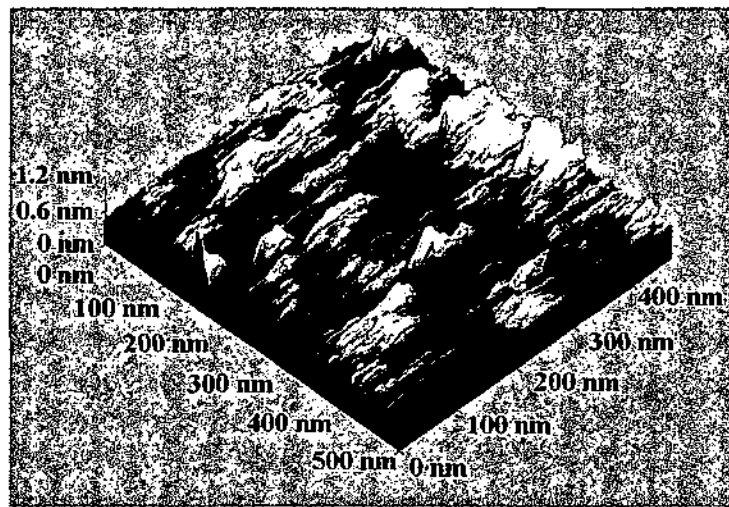

Fig. II.2.4.1:
LiF (700; single crystal surfaces with CO_2 snow cleaning right after cleavage.

II.2.5 SiO_2 (0001) α-Quartz

Standard crystal preparation technique:

Single SiO_2 (0001) α-quartz crystals (TBL Kelpin, Germany) are CO_2 snow cleaned and then annealed in UHV at 400 °C for three hours. This preparation technique yields flat crystal surfaces. AFM contact mode studies on 14 crystals prepared by the standard preparation technique revealed a root-means-square (rms) roughness of 0.16 ± 0.01 nm rms (fig. II.2.5.1).

Fig. II.2.5.1: Fflat SiO_2 (0001) single crystal surface after standard preparation technique: the surface roughness is 0.16 ± 0.01 nm rms. UHV AFM contact mode, imaging parameter height z.

II.2.6   Muscovite Mica ($KAl_2[AlSi_3]O_{10}(OH)_2$)

The muscovite mica structure consists of sheets of tetrahedra arranged in pairs, enclosing a sheet of edge-sharing octahedra. The apices of the tetrahedra connect to the octahedra of the central layer. Between each "sandwich" there are interlayer sites which can contain large cations. The coordination of the octahedra is completed by OH anions. The general formula of mica group minerals is $XY_{2-3}Z_4O_{10}(OH)_2$, with X denoting the interlayer site, Y denoting the octahedral sites and Z denoting the tetrahedral sites. In muscovite mica, $KAl_2[AlSi_3]O_{10}(OH)_2$, the octahedral sheet is made up of the dominantly trivalent cation Al, in which case one of the three sites is left vacant (dioctahedral mica). In true micas, like muscovite mica, Al substitutes for Si in the tetrahedra, and charge balance is maintained by K, Na, or more rarely Ca, in the interlayer site.
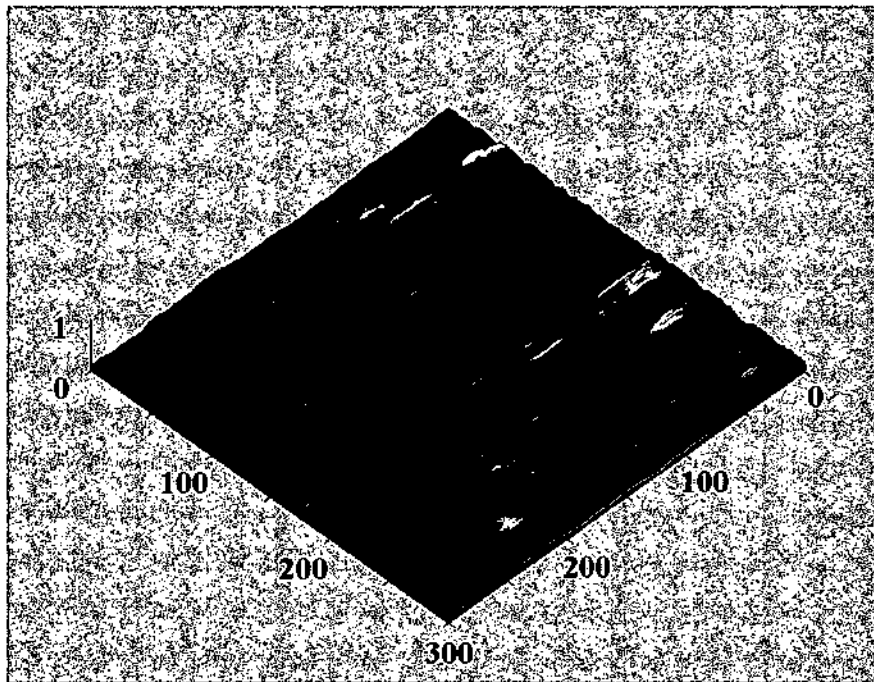
Standard crystal preparation technique:

Muscovite mica is prepared atomically flat by cleavage in air with adhesive tape. The sample is then transferred to UHV and annealed for three hours at $400\,^{\circ}$ C.

II.2.7   Sapphire c-plane Al_2O_3 (0001)

Standard crystal preparation technique:

Al_2O_3 (0001) c-plane single crystal surfaces (TBL Kelpin, Germany) are CO_2 snow cleaned and then annealed for three hours at 400 °C in UHV.

This preparation technique yields very flat crystal surfaces (fig. II.2.7.1). AFM contact mode studies on 14 samples prepared by the standard preparation technique revealed a root-mean-square roughness of 0.093 ± 0.06 run rms.

Fig. II.2.7.1: Very flat Al_2O_3 (0001) single crystal surface after standard preparation technique. UHV AFM contact mode investigations show that the root-mean-square roughness is less than 0.1 nm for all 14 samples investigated.

II.3 Presentation and discussion of MCI – produced nanodefects on different insulator surfaces

Abstract

An atomic force microscopy (AFM) was used to investigate single impacts of slow singly and multiply charged Ar ions on atomically clean insulator surfaces for LiF(100), SiO2(0001) α-quartz, muscovite mica and sapphire c-plane $Al_2O_3(0001)$ crystals. The target samples have been continuously kept under UHV conditions by transferring them in a transportable UHV vault from the vacuum chamber for ion bombardment to the AFM instrument. Slow ion bombardment was accompanied by low-energy electron flooding to compensate for possible target surface charge-up. For Al_2O_3 clear ion-charge dependent surface defects in lateral and vertical directions give evidence for potential sputtering, which until now has only been demonstrated with thin polycrystalline insulator films.

II.3.1   Results for different target materials

In the following our experience with AFM observations of different insulator target surfaces is described [98]. In all measurements the AFM contact mode (see chater II.2.3) has been employed, and sometimes also other AFM modes (non-contact, lateral-force) have been used. Where possible, our results are compared with similar work from other groups.

II.3.1.1 Results for LiF (100)

Nanoscale modifications of different alkalihalide surfaces (NaCl, KCl, KBr) induced by electronic transitions have been studied with AFM down to atomic resolution [101]. In our case we have used LiF(100) single crystals (TBL Kelpin, Neuhausen, Germany) which were cleaved in air, CO_2 snow cleaned (Applied Surface Technologies, New Providence, NJ, USA), transferred into the UHV irradiation chamber and annealed at 400 °C for three hours. With this crystal preparation techniques we could routinely image monoatomic terraces with atomic resolution in the AFM contact mode (see chapt. II.2.3). However, the complex structure of the LiF(100) surface resulting after slow ion bombardment made a correlation of possible ion induced nanodefects to ion doses and -charge states rather difficult. So far, we could not find significant changes in surface topography between the unbombarded LiF(100) surfaces and their bombardment with 100 eV Ar^{2+}, 400 eV Ar^{2+}, 250 eV Ar^{3+} and even 3 keV Ar^{7+}, respectively. For demonstration, fig. II.3.1.1 shows a LiF(100) surface after preparation and bombardment with Ar^{3+} ions with a dose of 10^{12} ions/cm^2 (i.e. about one ion per 10x10 nm^2 only). Bombardment with 100 eV Ar^{2+} ions with larger doses up to 5×10^{15} ions/cm^2 did not produce distinctive changes in surface topography. The investigations are continued by preparing flatter LiF(100) surfaces on which the ion induced defects can probably be diagnosed, which will be important for comparison with our earlier studies on PS involving polycrystalline LiF films [19].
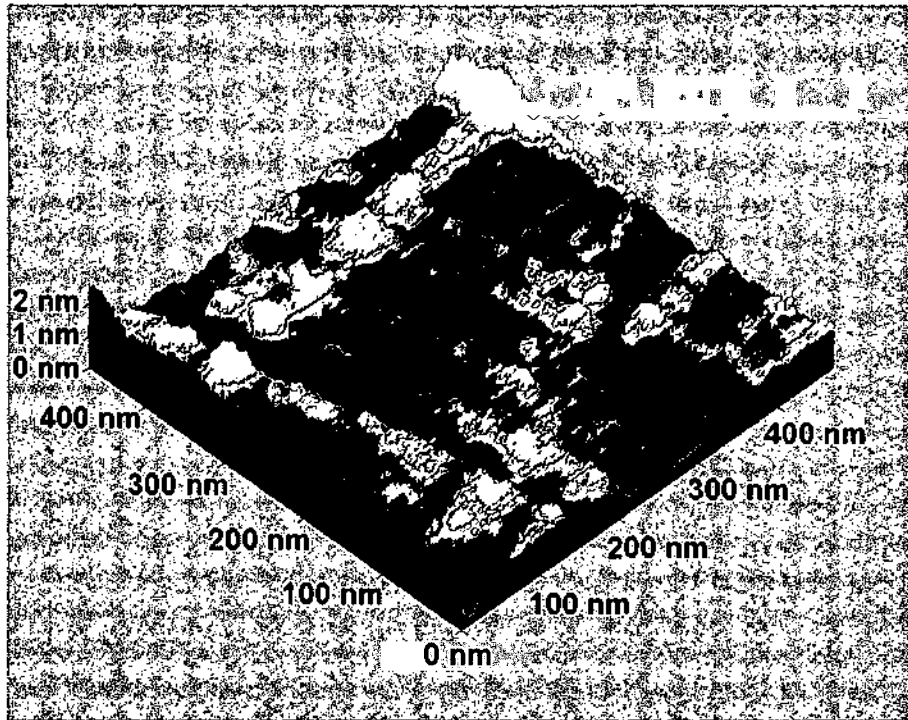
Fig. II.3.1.1: LiF(lOO) single-crystal surfaces after standard preparation (see text) and bombardment with 250 eV Ar^{3+} ions (480x480 nm^2, imaging parameter height z [98]).

II.3.1.2 Results for SiO_2 (0001)

Quartz is the only monocrystalline target surface for which the microbalance technique has been applied in order to demonstrate PS [102]. For the present work, polished SiO_2 (0001) α-quartz single crystals (TBL Kelpin, Neuhausen, Germany) were CO_2 snow cleaned and annealed in UHV at 400 °C for three hours. This procedure resulted in very flat crystal surfaces for which our AFM contact mode measurements on fourteen samples revealed a root-mean-squares (rms) roughness of 0.16 ± 0.01 nm, as a hopefully excellent start for our PS investigations. These quartz crystals were then bombarded with 1 keV Ar^+ ions. AFM imaging of resulting surface topography indeed clearly revealed ion induced nanostructures as shown in fig. II.3.1.2. The surface is covered with hillocks a few nanometers high. However, the density of these hillocks did not directly correspond to the applied ion doses: for a dosis of about one incident 1 keV Ar^+ ion per $10 \times 10 \, nm^2$, we observe only about 30 nanostructures on an area of $1000 \times 1000 \, nm^2$, which indicates that not every single ion has caused one nanodefect on the quartz surface. Probably several ion impacts are necessary to induce a

detectable surface modification: The ion dosis in all cases was 10^{12} ions/cm^2, equivalent to one incident ion per 10×10 nm^2. Probably individual ion tracks do not need to overlap to induce multiple ion induced nanostructures, but may cause defects on the insulator surface which increase the chance that impact of another ion in the near vicinity gives rise to an observable surface structure. The fact that surface modifications found after ion bombardment are observed as hillocks instead of craters is also not yet understood, but several possible explanations are conceivable: In AFM as for other scanning probe microscopy methods it is more straightforward to image elevated structures than craters. Even worse, narrow but highly elevated surface features in the vicinity of craters would completely mask the latter because of their convolution with the tip shape. So far, very few studies have been performed in this field, in particular for insulating surfaces. Several groups having applied AFM did report hillocks as surface modifications after bombardment with heavy ions, in some cases even for GeV impact energies. Audouard et al. [103] studied by AFM the surface of amorphous metals irradiated with swift heavy ions.
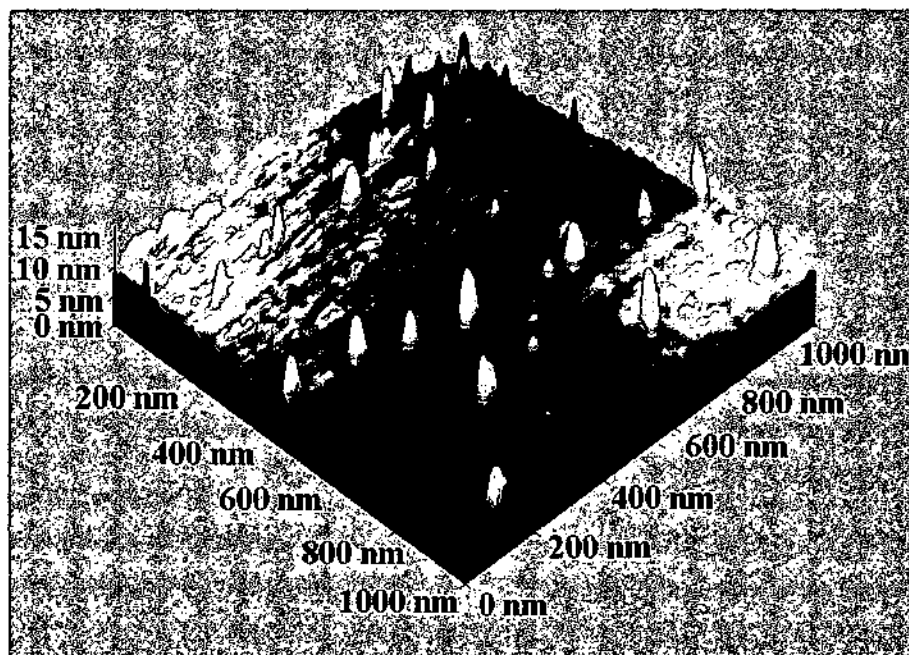

Fig. II.3.1.2: Polished SiO2(0001) α-quartz single crystal after CO$_2$ cleaning, annealing and bombardment with 1 keV Ar$^+$ ions (UHV AFM contact mode). Ion bombardment results in hillocks with a height of several nanometers [98].

The ion impacts apparently caused formation of hillocks for irradiation at 300 K if the ions provided sufficiently large electronic stopping (>55 keV/nm). On the other hand, irradiation at 80 K did not induce noticeable modifications of the metal surface. These results indicate that formation of hillocks which are flattened by the sample growth is essentially caused by the damage from electronic excitation in individual ion tracks. In another experiment the same group [104] studied with AFM modifications of the surface topography of amorphous metallic alloys. Irradiation with swift Pb- or U ions led to formation of hillocks surrounded by craters, whereas no visible surface modifications were observed after irradiation with Kr ions which caused less electronic stopping. In the view of these authors formation of hillocks can be ascribed to damage created in individual ion tracks, while craters would be linked to the occurrence of anisotropic growth. Both processes are induced by severe electronic excitation in the wake of incident ions.

II.3.1.3 Results for MICA

Muscovite mica is an aluminosilicate growing in sheets. Our mica samples which have been provided by Omicron Nanotechnology can be easily prepared to atomical flatness by cleavage in air with adhesive tape. The samples were then transferred to UHV and annealed for three hours at 400 °C. We could routinely obtain atomic resolution on these mica surfaces both in the AFM height- and the lateral force mode. Mica features large atomically flat terraces with small steps between them. In searching for nanodefect formation by singly- and multiply charged ions we bombarded these mica surface with 400 eV Ar^+, 500 eV Ar^+, Ar^{2+} and Ar^{7+}, 800 eV Ar^+ and Ar^{4+}, 1 keV Ar^+ and 1.2 keV Ar^+, respectively. After bombardment with the slowest ions (400 eV Ar^+, 500 eV Ar^+ and Ar^{2+}) no surface modifications were found in AFM contact- as well as non-contact modes. For bombardment by 800 eV Ar^+ and Ar^{4+} only very few nanodefects could be seen on the irradiated surfaces. We observed hillocks with a few nanometers high and about 50 nm in diameter. They appeared in very low densities on the surface and might not necessarily have been caused by the ion bombardment. Surface modifications could only be attributed unambiguously to ion bombardment for ≥1 keV Ar^+ ions. Fig. H.3.1.3 shows a mica surface after 1.2 keV Ar^+ ion bombardment where the density of observable surface nanodefects was already considerably larger than for 1 keV Ar^+ impacts administered with similar doses (1 keV Ar^+ ions induced about 10 nanodefects per 1000x1000 nm^2, whereas for 1.2 keV Ar^+ ions, the density of ion induced nanodefects was

about 200 per 1000x1000 nm^2). However, also for mica no clear dependence on the ion charge state could be found, so far. Several groups have performed AFM investigations of mica surfaces irradiated with highly charged ions. All these investigations were made on air under normal conditions.
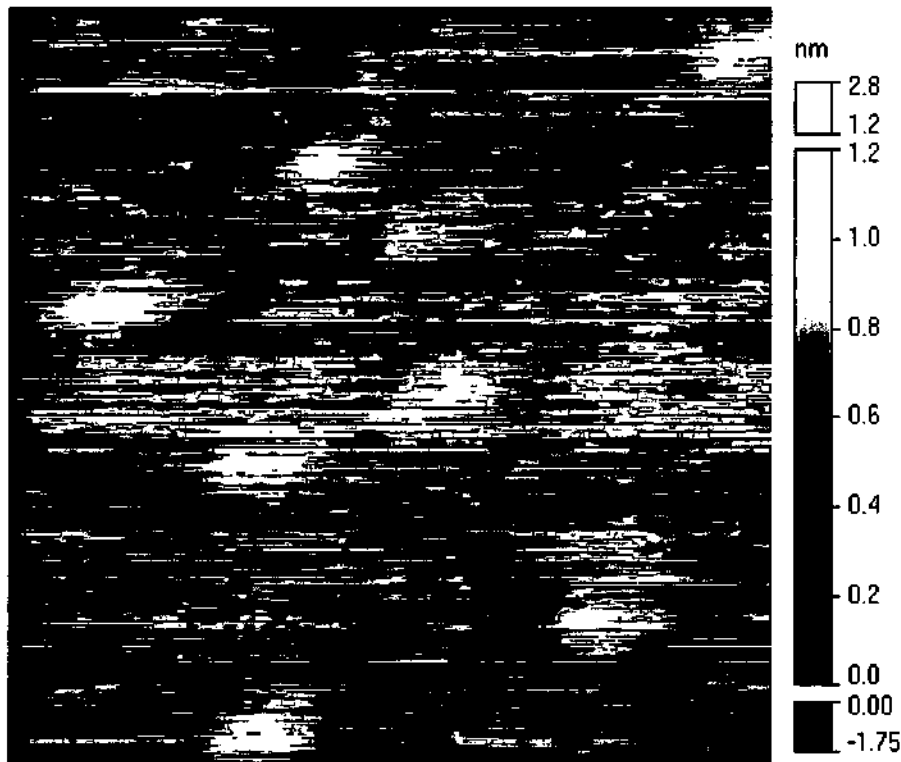
Fig. II.3.1.3: AFM scan of muscovite mica bombarded with 1.2 keV Ar$^+$ ions. Observed features are ion-induced topographic defects [98].

We believe that only under UHV conditions imposed throughout the procedures of irradiation and AFM for investigating ion induced nanodefects an indisputable assignment of the latter to MCI bombardment is possible. Anyhow, as a general result from these studies MCI impact on mica left bumps with about 1 nm height and 15 nm diameter. Parks et al. [105] showed that the size of these bumps was not strongly correlated to the kinetic ion energy. This work was later extended in order to demonstrate that the size of observed nanodefects was strongly correlated with the potential ion energy [86]. With 100 keV Xe^{q+} ions ($25 \leq q \leq 50$) impinging on mica, damage caused by single ion impacts was observed with AFM at ambient conditions, with the impact sites typically appearing as circular hillocks. In the view of these authors this hillock- rather than crater-like feature is caused by the highly anisotropically layered structure of mica.

II.3.1.4 Results for Al_2O_3 (0001)

Polished Al_2O_3 (0001) c-plane single crystals (TBL Kelpin, Neuhausen, Germany) have been CO_2 snow cleaned and annealed for three hours at 400 oC in UHV. This yielded as for SiO_2 very flat crystal surfaces. AFM contact mode studies on numerous samples prepared by this technique revealed a rms roughness of 0.09 ± 0.06 nm. Bombardment with Ar ions with different charge states and kinetic energy (500 eV Ar^+, Ar^{7+}, 1.2 keV Ar^+, Ar^{4+} and Ar^{7+}) resulted in hillock-like nanodefects seen in AFM contact mode (cf. figs. II.1.4a-e). The density of ion induced nanodefects did not directly correspond to the applied ion dose (5×10^{12} ions/cm^2) but was rather small, however reproducible: about 10 nanodefects per 1000x1000 nm^2 can be observed after bombardement in the energy range 500-1200 eV reported here. Such a direct correspondence has only been found in STM investigations of HOPG [106]. However, on the Al_2O_3 c-plane crystals we could show a clear correlation of slow ion induced defects with both kinetic energy and charge state of the projectile ions. We also found that the defects caused by slow ion impact could completely be removed by annealing the Al_2O_3 crystals at 450 °C for about five hours. 500 eV Ar^+ ion impact produced defects with about one nanometer heigth and some tens of nanometers width (fig. II.3.1.4a). One should keep in mind that with AFM the height of surface features can more accurately be measured than their lateral dimension. Defects produced by 500 eV Ar^{7+} ions were several nanometers high (see fig. II.3.1.4b) and had lateral dimensions of about 100 (!) nanometers. At higher kinetic ion energy differences of ion induced nanodefects became even more distinct. 1.2 keV Ar^+ induced defects were up to eight nm nanometers high and some ten nanometers wide (fig. II.3.1.4c). For impact of higher charged Ar^{4+} two different kinds of defects appeared on the surface (fig. II.3.1.4d) with similar heights of about two nm, but considerably different lateral extensions.

Some were nearly 200 nm wide, but smaller defects (only about 50 nm wide) were found as well. Finally, for impact of Ar^{7+} only one kind of defects was visible in the AFM images, measuring about 50 nm across and 2 nm in height (see fig. II.3.1.4e).

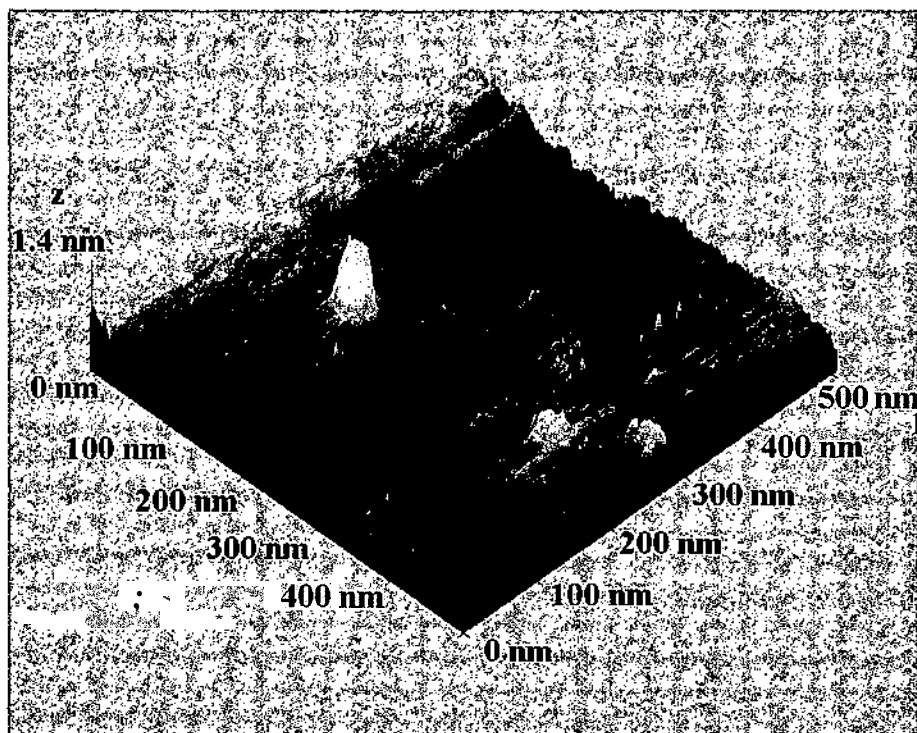*Fig. II.3.1.4a:* $Al_2O_3(0001)$ *single-crystal surface after annealing and bombardment with 500 eV* Ar^+ *ions [98].*

Fig. II.3.1.4b: $Al_2O_3(0001)$ *single-crystal surface after annealing and bombardment with 500 eV* Ar^{7+} *ions [98].*

Fig. II.3.1.4c: $Al_2O_3(0001)$ single-crystal surface after annealing and bombardment with 1.2 keV Ar^+ ions [98].
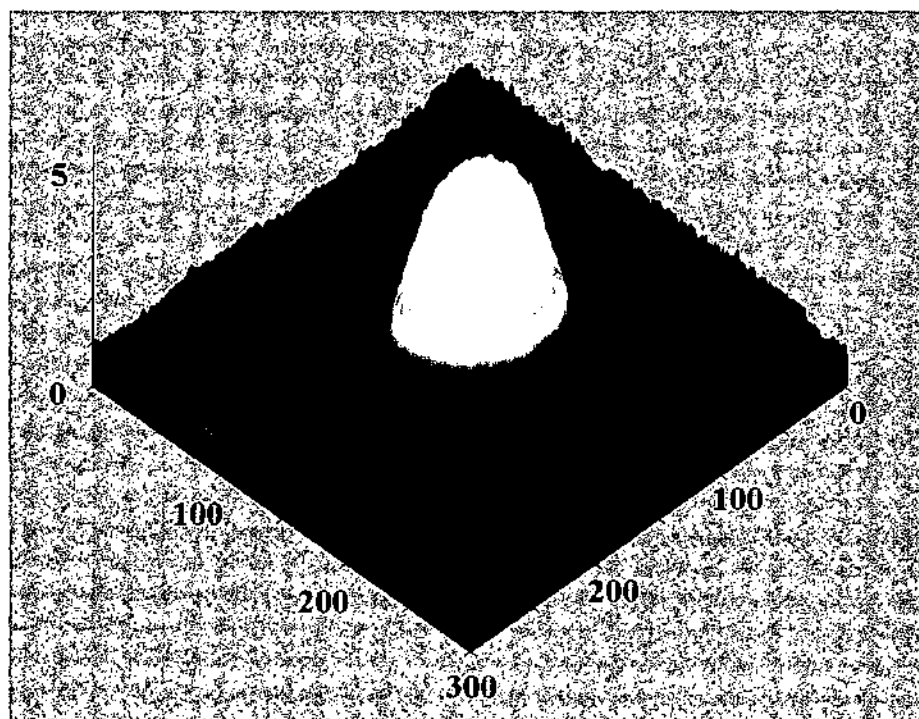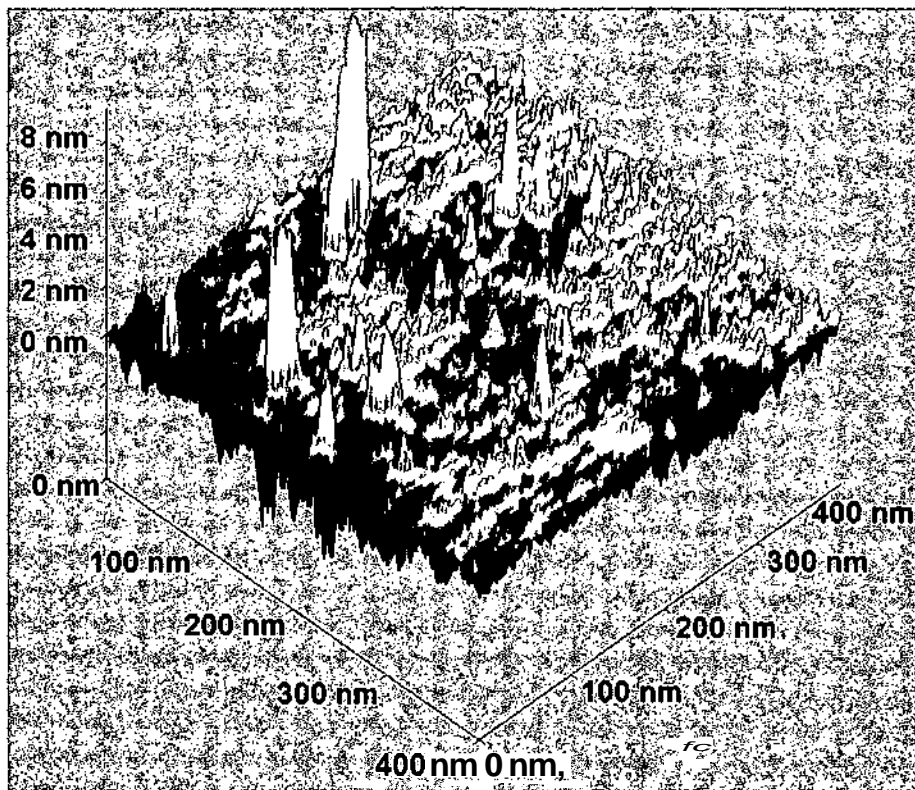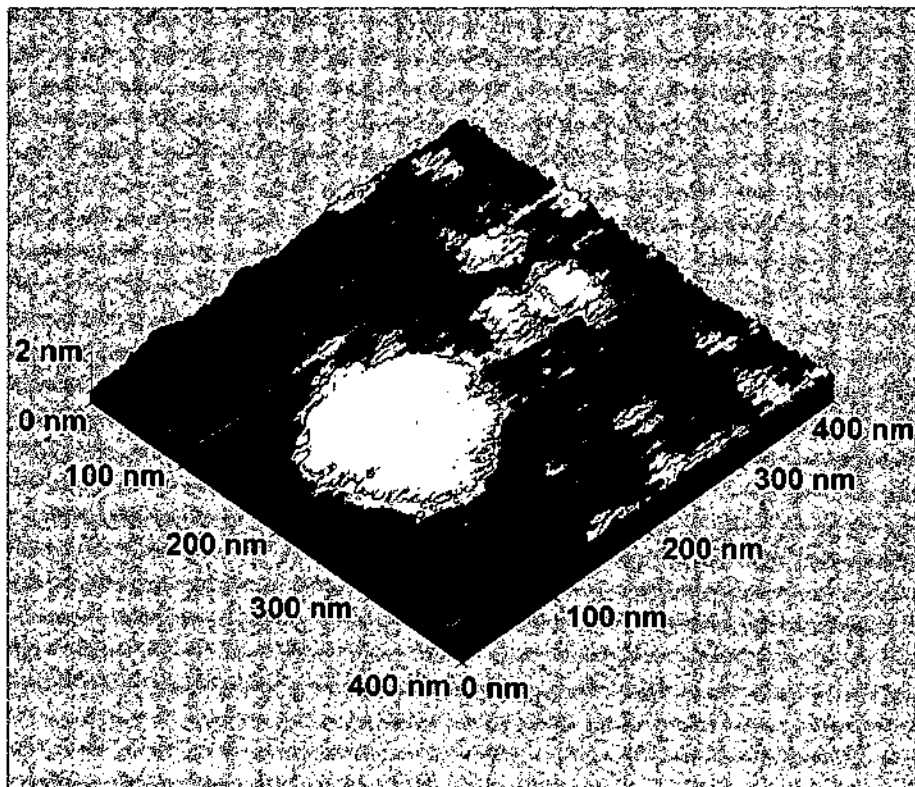

Fig. II.3.1.4d: $Al_2O_3(0001)$ single-crystal surface after annealing and bombardment with 1.2 keV Ar^{4+} ions [98].
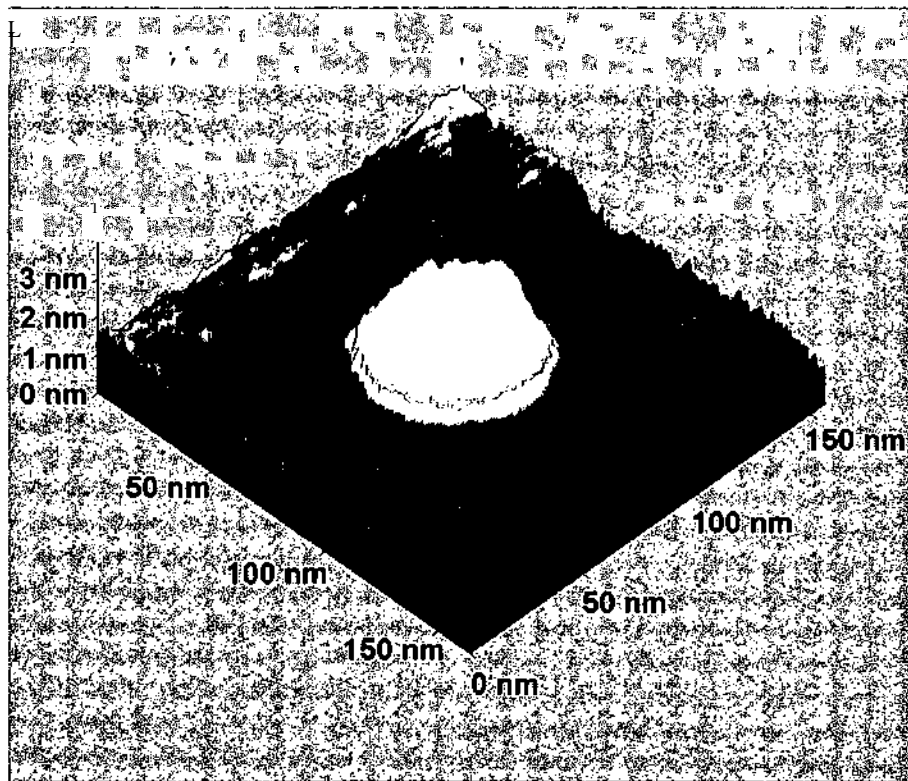
Fig. II.3.1.4e: $Al_2O_3(0001)$ single-crystal surface after annealing and bombardment with 1.2 keV Ar^{7+} ions [98].

II.3.2   Summary and conclusions

The second part of this thesis describes systematic efforts to find evidence for potential sputtering (PS) by means of AFM inspection of atomically clean monocrystalline insulator surfaces which have been bombarded by slow (typically < 1 keV) singly and multiply charged Ar^{q+} ions (up to $q = 7$). The study may be seen as an extension of earlier work by other groups who looked for similar effects. In contrast to the present work, however, they have shot much faster multiply charged ions on various gas-covered surfaces and inspected them by AFM in air [85, 105, 106], or made STM investigations of atomically clean HOPG surfaces bombarded by slow (150 eV) Ar^{q+} ions (up to $q = 9$ [106]) or much faster (several 100 keV) Xe^{q+} ions (up to $q = 44$ [107]) (see also chapt. II.4). AFM in UHV is probably indispensable for finding clear-cut evidence of PS related nanodefects induced by slow multicharged ions with a size clearly depending on the ion charge state. In this work Al_2O_3 has been identified as a good candidate for such PS induced nanostructuring, and for SiO_2 further research might lead to a similar conclusion. Both materials are of great relevance for applications in a rapidly emerging field combining microelectronics and nanotechnology.

Our studies on atomically clean insulator surfaces indicate that the potential sputtering effect - which has been found to be rather strong for thin films of the materials investigated here - might be more dependent on defect-mediation than so far assumed. For sure, we see potential energy dependent nanodefects generated on the single crystal surfaces, but their density is too low to prove that the potential sputtering effects in thin films and single crystals are of equal importance.

Our expectations concerning the use of potential sputtering on monocrystalline surfaces, e.g. for nanostructuring applications, which originated from our previous experience with thin films, have not been met so far. Further studies along these lines are thus highly desirable.

II.4 MCI - produced nanodefects on HOPG surface

Abstract

A systematic STM-/AFM investigations on nanoscopic defect production at atomically clean surfaces of highly-oriented pyrolytic graphite (HOPG) after bombardment by slow (impact energy < 1 keV) singly and multiply charged ions under strict UHV conditions is presented. Combined STM- and AFM studies show that on HOPG only "electronic" but no visible topographic defects are created by such ion bombardment. For HOPG a clear dependence of the defect size on the projectile ion charge is demonstrated.

II.4.1 Experimental methods

Observations of slow-ion induced nanodefects on different atomically clean target surfaces have been made under strict UHV conditions with a combined AFM/STM instrument (see chapter II 2.3). We have looked for nanodefects on freshly prepared surfaces of HOPG after irradiation with low doses of slow singly and multiply charged ions. The experimental setup was similar to chapter II.3.

HOPG is rather easy to prepare with surface terasses which extend over several hundreds of nm (see chapt. I 2.3). The HOPG samples were cleaved in air with adhesive tape and immediately put into the ultrahigh vacuum chamber (base pressure below 10^{-9} mbar). Before ion irradiation a sample was heated up to 300°C, but during the irradiation experiment kept at room temperature. STM images were taken at constant current mode with negative sample bias voltage in the range of some mV to Volts and tunneling currents of 1-10 nA. Electrochemically etched tungsten tips were used which provided excellent atomic resolution. Again, AFM data were taken in the contact mode.

II.4.2 Slow ion-induced surface defects on HOPG

Surface defects in highly oriented pyrolytic graphite (HOPG) produced by the impact of individual (singly charged) ions have already been investigated via STM/AFM by a number of groups (see refs. [108-115] and further references therein). However, only recently first results have been reported for impact of slow multiply charged ions and the effect of the projectile charge state (or potential energy) on the size of the produced nanodefects [106, 107]. Moreover, in most previous studies either STM in air was used or the irradiated samples were transported in air towards STM inspection after ion bombardment. If, e.g., chemical bonds at the surface are broken due to the ion impact, impurities could preferentially adsorb at these sites and thus change the topography of the surface (and the resulting STM image) during contact with air. Therefore, in our studies MCI bombardment has been followed by STM/AFM investigations without breaking the ultra high vacuum (see chapt. II.2.3). In this way possible influences from target surface exposure to air could be ruled out.

Fig. II.4.2.1 shows typical AFM- and STM scans of HOPG samples bombarded with 1200 eV Ar^+ ions. In the AFM scan no significant topographic changes can be detected. On the contrary, the STM image reveals a large number of individual nanosized defects as the result of the ion bombardment. Several hundred defects from different sample positions have been statistically analysed for each projectile type (Ar^+, Ar^{8+}, Ar^{9+}). Fig. II.4.2.2 shows the enlarged STM image of a typical defect on HOPG created by the impact of a single Ar^{9+} ion of 150 eV kinetic energy.

Figs. II.4.2.3 and II.4.2.4 show examples of STM 3D-images of a highly oriented pyrolitic graphite surface bombarded with 150 eV Ar^+ and Ar^{9+} ions, respectively. The images were taken from a 16-bit black-and-white graphics and processed by the SXM image program using a calculated shadow by illuminating the images from the left.

The only surface defects found in the STM images (figs. II.4.2.1 - II.4.2.4) are "protrusions" (hillocks) with a mean lateral size of 0.8 - 1.25 nm and an average equivalent height of 0.22 nm. They are randomly dispersed on the originally flat surface. Their area density is in good agreement with the applied ion dose, implying that nearly every single ion impact has caused one protrusion. A $\sqrt{3} \times \sqrt{3} R$ 30° surface reconstruction, as characteristic for interstitial defects in HOPG [114-116], surrounded by undisturbed surface parts is observed in the vicinity of most defects (see figs. II.4.2.3 – II.4.2.4).
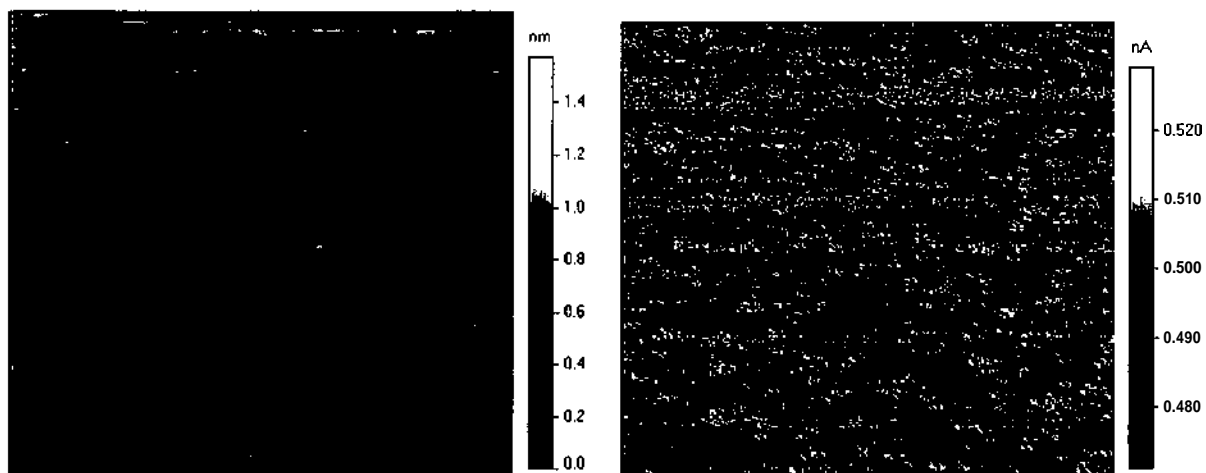
Fig. II.4.2.1: AFM- and STM (400×400nm) scans of HOPGbombarded with 1200 eV Ar⁺ ions. In the AFM scan no topographic changes can be detected (left side). Only the STM reveals the defects in the electronic structure (right side).
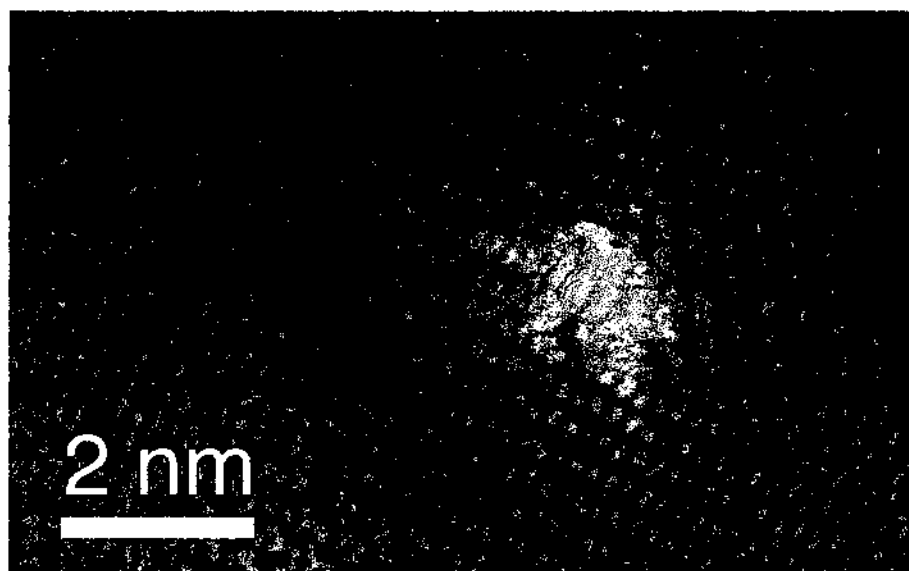
Fig. II.4.2.2: STM image of a defect produced by the impact of a single (150 eV) Ar⁹⁺ ion on HOPG.
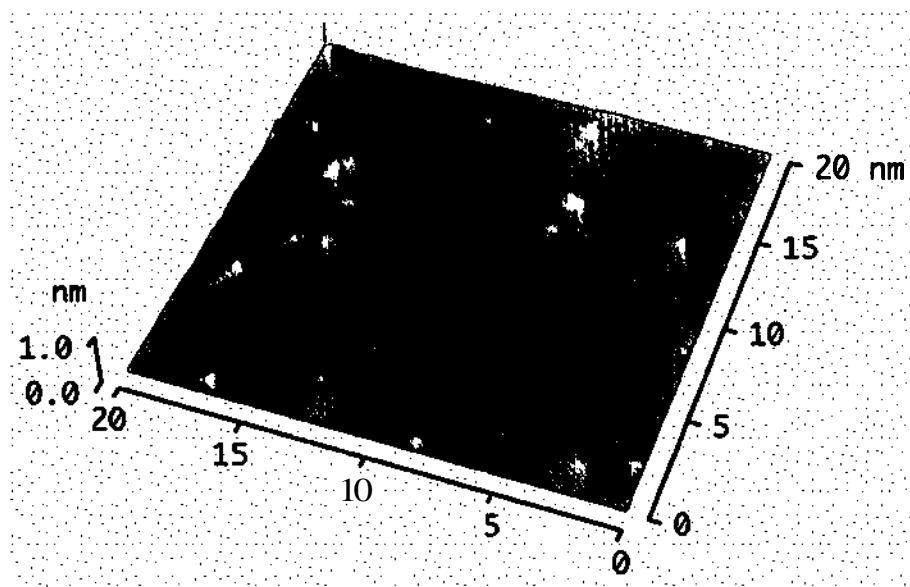
Fig. II.4.2.3: STM image of a HOPG surface bombarded by Ar^+ ions of 150 eV kinetic energy (tunneling current: 0.58 nA, bias voltage: 0.5 V)
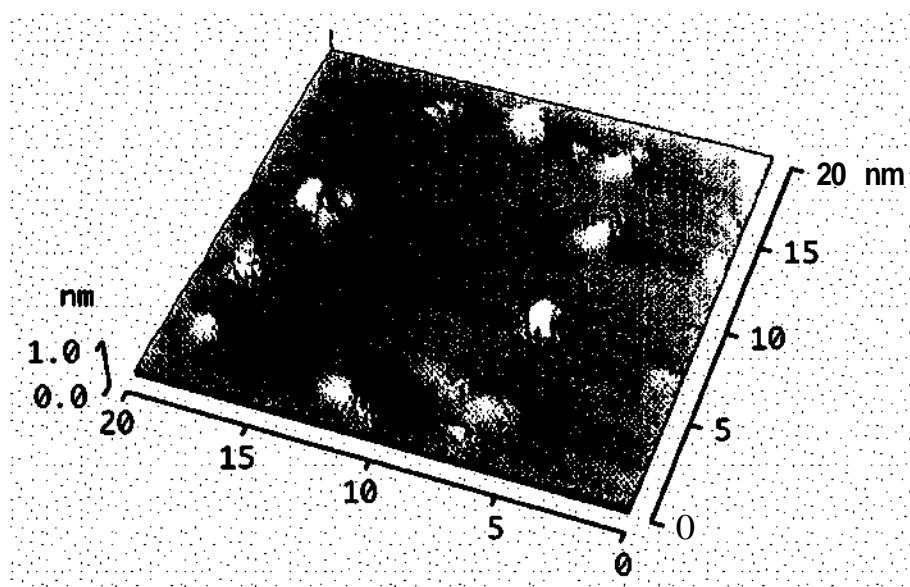

Fig. II.4.2.4: STM image of a HOPG surface bombarded by Ar^{9+} ions of 150 eV kinetic energy (tunneling current: 0.55 nA, bias voltage: 0.4 V)

Scans performed with our atomic force microscope (AFM) on the irradiated surface did not show any significant topological changes due to ion impact. Therefore we conclude that the defects observed are mainly due to changes in the electronic density of states of the surface.

Our findings for impact of singly charged ions are in good agreement with previous observations [111, 115]. As a remarkable result, however, we find that the measured mean diameter of the "hillocks" and to a somewhat lesser extent their height increase with projectile charge state (see fig. II.4.2.5). The corresponding statistical distribution of the evaluated damage height and the full width at half maximum (FWHM) due to Ar^+ and Ar^{9+} ion bombardment of the HOPG surface are shown in fig. II.4.2.6.
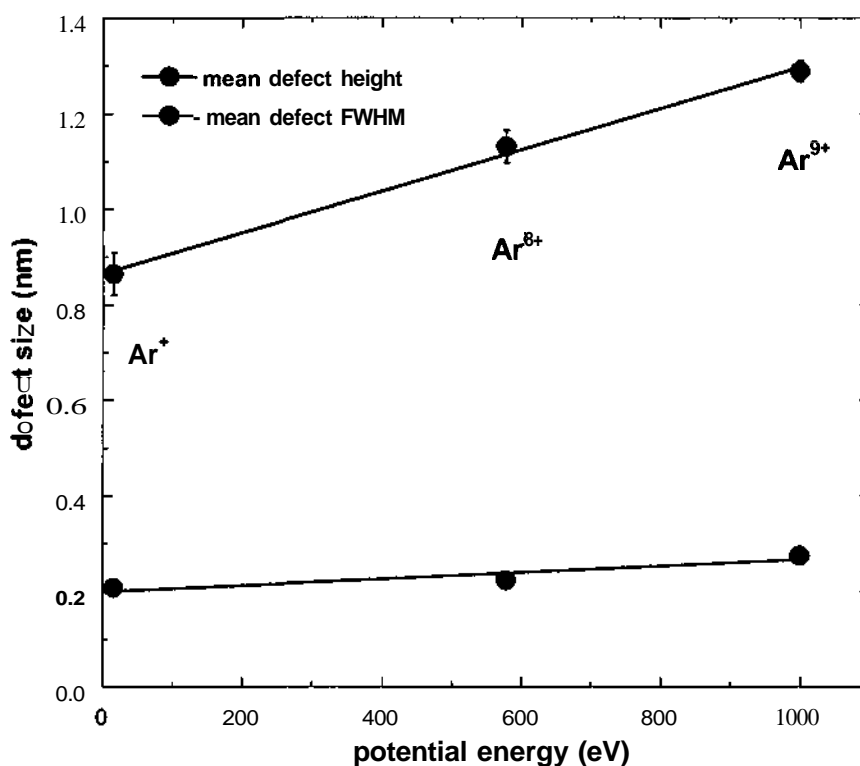
Fig. II.4.2.5: Mean height and width (FWHM) of defect structures produced by impact of 150 eV Ar^{q+} (q=1, 8, 9) ions on HOPG. For each projectile species data were obtained from different STM images by evaluating all visible defects.

In a careful STM study, Hahn and Kang [115] have shown that generally two kinds of defects in HOPG are created under low energy $(100 \, eV)$ Ar^+ bombardment, i.e. carbon vacancy defects (VD) and interstitial defects (ID) formed by trapping the projectile beneath the first carbon plane. Both types of defects are detected as protrusions in the STM topographic image. The dangling bonds at the VD site cause an enhancement of the local charge density-of-states (CDOS) near the Fermi energy, seen as a protrusion in the STM image [115].

Fig. II.4.2.6: Statistical distribution of damage height (a, b) and full width at half maximum (FWHM)(c, d) due to singly charged Ar ion impact (a, c) and Ar $^+$ *ion impact (b, d) on HOPG.*

The protrusion observed in the STM image at ID sites results form a small geometric deformation of the graphite basal plane due to the trapped projectile (not large enough to be visible in ou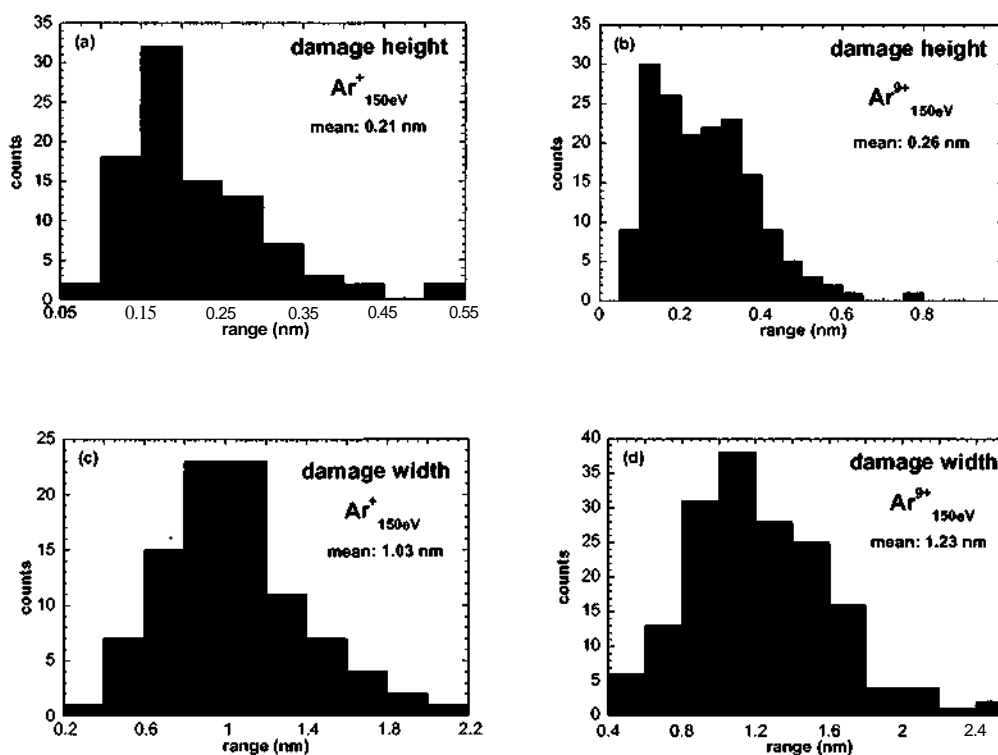r AFM scans) and an apparently larger electronic defect due to an increased CDOS. Only for IDs but not for VDs a $\sqrt{3} \times \sqrt{3}\ R\ 30°$ surface reconstruction was reported [115]. From this $\sqrt{3} \times \sqrt{3}\ R\ 30°$ superlattice structure also observed in our experiments (see fig. II.4.2.7) we therefore conclude that the majority of the "hillocks" observed are due to IDs or VDs created along with IDs. The strong increase of the lateral protrusion size with increasing charge state of the projectile ion is interpreted as a "pre-equilibrium" effect of the stopping of slow multiply charged ions in HOPG, as has so far only been observed for higher charge states [112]. Although slow MCI are converted already into neutral hollow atoms during their approach towards the surface, their captured electrons remain in highly exited states until surface impact, where they are gradually peeled off and replaced by conduction band electrons forming a partial screening cloud around the HCI [13, 15]. Before final deexcitation of the hollow atom can take place within the solid, reduced screening should result in a strongly increased energy loss of the projectiles. According to SRIM 2000 calculations [10] the mean range of 150 eV Ar projectiles in HOPG is about two monolayers. An increased stopping and straggling of the higher charged Ar projectiles would lead to IDs located closer to the surface, as well as to more VDs due to a higher momentum transfer to the carbon atoms of the first plane. Because of the extreme surface sensitivity of STM this pre-equilibrium effect in the stopping power is not masked by (equilibrium) bulk effects but apparently observable with unprecedented clearness. From these AFM data we see that the nanodefects produced by slow ion impact are of electronic rather than of topolographical nature.
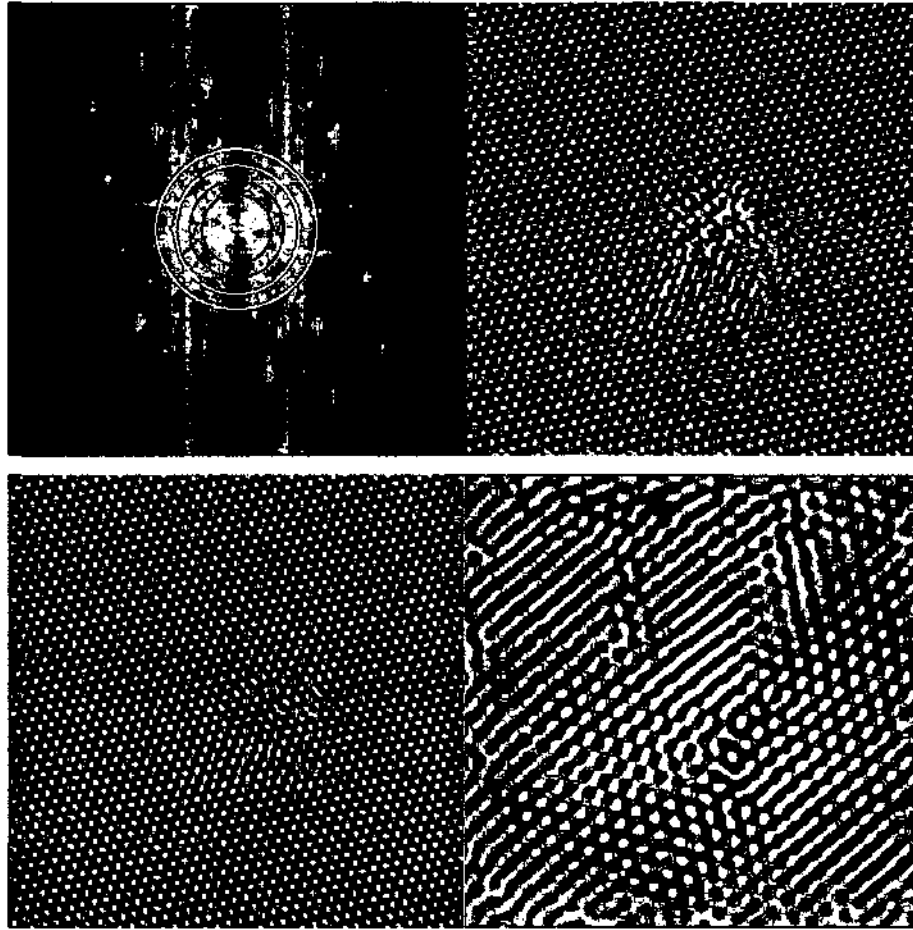
Fig. II.4.2.7: Fourier transform (top left) of a tunneling current image of a Ar$^+$ ion induced defect on HOPG (top right). Filtering and inverse Fast Fourier Transformation allow for separation of the contributions from the undisturbed crystal lattice (bottom left, reconstructed from frequencies within the white circles) and ion induced superstructure (bottom right, reconstructed from frequencies within the green circles), respectively. Top left and bottom tunneling current images 10x10 nm^2.

Bibliography

[1]   H. Gnaser, *Low-Energy Ion Irradiation of Solid Surfaces* (Springer Berlin, 1999).

[2]   M. V. R. Murty, Surf. Sci. 500, 523 (2002).

[3]   M. P. Villard, J.Phys.Theor.Appl. 3, 5 (1899).

[4]   M. Rosier and W. Brauer, in *Particle Induced Electron Emission I,* edited by G. Höhler (Springer, Berlin, 1991), Vol. 122.

[5]   D. Hasselkamp, in *Particle Induced Electron Emission II,* edited by G. Höhler (Springer, Heidelberg, 1992), Vol. 123, p. 1

[6]   F. Aumayr and HP. Winter, Comments At.Mol.Phys. 29, 275 (1994).

[7]   G. Lakits, F. Aumayr, M. Heim, and HP. Winter, Phys.Rev.A 42, 5780 (1990).

[8]   H. Eder, M. Vana, F. Aumayr, and HP. Winter, Rev. Sci. Instrum. 68, 165 (1997).

[9]   P. Sigmund, (Mat.Fys.Medd., Copenhagen, 1993), Vol. 43, p. 2.

[10]   J. F. Ziegler, J. P. Biersack, and U. Littmark, *The Stopping and Range of Ions in Matter* (Pergamon, New York, 1985).

[11]   G. Schiwietz, E. Luderer, G. Xiao, and P. L. Grande, Nucl. Instrum. Meth. Phys. Res. B 175 - 177, 1 (2001).

[12]   W. M. Arnoldbik, N. Tomozeiu, and F. HP. M. Habraken, Nucl. Instrum. Meth. Phys. Res. B 203, 151 (2003).

[13]   A. Arnau, F. Aumayr, P. M. Echenique, M. Grether, W. Heiland, J. Limburg, R. Morgenstern, P. Roncin, S. Schippers, R. Schuch, N. Stolterfoht, P. Varga, T. J. M. Zouros, and HP. Winter, Surf. Sci. Reports 229, 1 (1997).

[14] F. Aumayr, in *The Physics of Electronic and Atomic Collisions,* edited by L. J. Dubé, J. B. A. Mitchell, J. W. McConkey and C. E. Brion (American Institute of Physics (AIP Press), New York, 1995), Vol. 360, p. 631.

[15]   HP. Winter and F. Aumayr, J. Phys. B: At. Mol. Opt. Phys. 32, R39 (1999).

[16]   HP. Winter and F. Aumayr, Physica Scripta T92, 15 (2001).

[17]   HP. Winter and F. Aumayr, Euro. Phys. News 33, 215 (2002).

[18]   T. Schenkel, A. V. Hamza, A. V. Barnes, and D. H. Schneider, Progr. Surf. Sci. 61, 23 (1999).

[19]   F. Aumayr, J. Burgdörfer, P. Varga, and HP. Winter, Comments At.Mol.Phys. 34, 201 (1999).

[20]   T. Neidhart, F. Pichler, F. Aumayr, HP. Winter, M. Schmid, and P. Varga, Phys.Rev.Lett. 74, 5280 (1995).

[21]   M. Sporn, G. Libiseller, T. Neidhart, M. Schmid, F. Aumayr, HP. Winter, P. Varga, M. Grether, and N. Stolterfoht, Phys.Rev.Lett. 79, 945 (1997).

[22]   H. Kurz, K. Töglhofer, HP. Winter, F. Aumayr, and R. Mann, Phys.Rev.Lett. 69, 1140 (1992).

[23]   F. Aumayr, H. Kurz, D. Schneider, M. A. Briere, J. W. McDonald, C. E. Cunningham, and HP. Winter, Phys.Rev.Lett. 71, 1943 (1993).

[24]   C. Lemell, J. Stöckl, J. Burgdörfer, G. Betz, HP. Winter, and F. Aumayr, Phys.Rev.Lett. 81, 1965 (1998).

[25]   H. Eder, F. Aumayr, and HP. Winter, Nucl.Instrum.Meth.B 154, 185 (1999).

[26]   J. Lörincik, Z. Sroubek, H. Eder, F. Aumayr, and HP. Winter, Phys. Rev. B 62, 16116 (2000).

[27]   J. Lörincik, Z. Sroubek, S. Cernusca, A. Diem, HP. Winter, and F. Aumayr, Surf. Sci. 504, 59 (2002).

[28]   A. Shirley, Phys. Rev. B 5, 4709 (1972).

[29]   U. Fleck, H. Wann, and P. Ziesche, Phys. Status Solidi 61, 447 (1980).

[30]   P. M. Echenique, R. M. Nieminen, J. C. Ashley, and R. H. Ritchie, Phys. Rev. A 33, 897 (1986).

[31]   R. A. Baragiola, E. V. Alonso, and A. Olivia-Florio, Phys. Rev. B 19, 121 (1979).

[32]   G. Spierings, I. Urazgil`din, P. A. Zeijlmans van Emmichoven, and A. Niehaus, Phys.Rev.Lett. 74, 4543 (1995).

[33]   G. Falcone and Z. Šroubek, Nucl. Instrum. Meth. Phys. Res. B 58, 313 (1991).

[34]   G. Falcone and Z. Šroubek, Phys. Rev. B 39, 1999 (1989).

[35]   U. Fano and W. Lichten, Phys.Rev.Lett. 14, 627 (1965).

[36] P. C. Stangeby, in *Physics of Plasma Wall Interactions in Controlled Fusion,* edited by D. E. Post and R. Behrisch (Plenum, New York, 1986), p. 41.

[37]   W. O. Hofer, J. Vac. Sci. Technol. A 5, 2213 (1987).

[38]   K. Ohya, Nucl. Instrum.Meth. Phys. Res. B 153, 58 (1999).

[39]   J. Roth, K. Ertl, and C. Linsmeier, (J. Nucl. Mat, 2001), Vol. 290 - 293.

[40]   P. C. Stangeby and G. M. McCracken, Nucl. Fusion 30, 1225 (1990).

[41]   E. W. Thomas, (ORNL, 1985).

[42]   W. O. Hofer and J. Roth, *Physical Processes of the interaction of fusion plasmas with solids* (Academic Press, San Diego, 1996).

[43]   R. K. Janev, *Atomic and Molecular Processes in Fusion Edge Plasma* (Plenum, New York, 1995).

[44]   G. Lakits, F. Aumayr, and HP. Winter, Rev.Sci.Instrum. 60, 3151 (1989).

[45]   F. Aumayr, G. Lakits, and HP. Winter, Appl.Surf.Sci. 47, 139 (1991).

[46]   H. Eder, W. Messerschmidt, HP. Winter, and F. Aumayr, J. Appl. Phys. 87, 8198 (2000).

[47]   E. R. Cawthron, Aust. J. Phys. 24, 859 (1971).

[48]   M. Leimer, D. Wutte, J. Brandstötter, F. Aumayr, and HP. Winter, Rev.Sci.Instrum. 65, 1091 (1994).

[49]   M. Leitner, D. Wutte, J. Brandstötter, F. Aumayr, and HP. Winter, Rev.Sci.Instrum. 65, 1091 (1994).

[50]   F. A. Cotton and G. Wilkinson, *Anorganische Chemie* (Verlag Chemie GmbH, Weinheim, 1982).

[51]   http://www.tectra.de/hopg.htm.

[52]   A. Qayyum, W. Schustereder, C. Mair, P. Scheier, T. D. Märk, S. Cernusca, HP. Winter, and F. Aumayr, Journal of Nuclear Materials 313, 670 (2003).

[53]   L. N. Large and W. S. Whitlock, Proc. Phys. Soc. London 79, 148 (1962).

[54]   S. M. Ritzau and R. A. Baragiola, Phys. Rev. B 58, 2529 (1998).

[55]   G. Lakits, F. Aumayr, and HP. Winter, Europhys. Lett. 10, 679 (1989).

[56]   H. D. Hagstrum, Phys.Rev. 96, 325 (1954).

[57]   H. D. Hagstrum, Phys.Rev. 96, 336 (1954).

[58]   R. Baragiola, in *Chap. IV in Low energy Ion-Surface Interactions,* edited by J. W. Rabalais (Wiley, 1993).

[59]   S. Cernusca, A. Diem, HP. Winter, F. Aumayr, J. Lörincik, and Z. Sroubek, Nucl.Instrum.Meth.Phys.Res.B 193, 616 (2002).

[60]   S. Cernusca, HP. Winter, F. Aumayr, A. Qayyum, W. Schustereder, C. Mair, P. Scheier, and T. D. Märk, International Journal of Mass Spectrometry and Ion Processes 223, 21 (2003).

[61]   M. Barat and W. Lichten, Phys.Rev.A 6, 211 (1972).

[62]   J. Fine, J. Lörincik, T. D. Andreadis, K. Franzreb, and Z. Sroubek, Nucl. Instrum. Meth. B 122, 270 (1997).

[63]   G. Federici et al., Nucl. Fusion 41, 1967 (2001).

[64]   G. Lakits, F. Aumayr, and H. Winter, Europhys.Lett. 10, 679 (1989).

[65]   A. Itoh, T. Majima, F. Obata, Y. Hamamoto, and A. Yogo,
       Nucl.Instrum.Meth.Phys.Res.B **193,** 626 (2002).

[66]   S. Cernusca, HP. Winter, F. Aumayr, R. Díez Muiño, and J. I. Juaristi,
       Nucl.Instrum.Meth.Phys.Res. B 203, 1 (2003).

[67]   A. Dubus, N. Pauly, M. Rosier, H. Rothard, M. Beuve, M. Caron, B. Gervais, A.
       Clouvas, and C. Potiriadis, Nucl. Instrum. Meth. Phys. Res. B 193, 621 (2002).

[68]   R. Diez Muino and A. Salin, Phys. Rev. B 62, 5207 (2000).

[69]   P. C. Zalm and L. J. Beckers, Surf. Sci. 152, 135 (1985).

[70]   J. N. Brooks, J. Nucl. Mat. 93 - 94, 437 (1980).

[71]   J. M. Pedgley and G. M. McCracken, Plasma Phys. Contr. Fusion 35, 397 (1993).

[72]   S. Takamura, S. Mizoshita, and N. Ohnu, Phys. Plasmas 3, 4310 (1996).

[73]   W. X. Wang, M. Okamoto, N. Nakajima, S. Murakami, and N. Ohyabu, Nucl. Fusion
       37, 1145 (1997).

[74]   I. V. Tsvetkov and T. Tanabe, J. Nucl. Mat. 266 - 269, 714 (1999).

[75]   K. Lackner and J. Schweinzer, (private communication, 1996).

[76]   A. Diem, in *Diploma Thesis* (TU Wien, 2002).

[77]   J. Stöckl, HP. Winter, F. Aumayr, S. Lederer, A. Mertens, K. Maass, and H. Winter,
       Nucl.Instrum.Meth.B 193, 644 (2002).

[78]   A. Mertens, S. Lederer, K. Maass, H. Winter, J. Stöckl, HP. Winter, and F. Aumayr,
       Phys.Rev. B 65, 132410 (2002).

[79]   P. M. Echenique, R. M. Nieminen, J. C. Ashley, and R. H. Ritchie, Phys.Rev.A 33,
       897 (1986).

[80]   S. S. Radzhabov, R. R. Rakhimov, and P. Abdusalumav, Izv.Akad.Nauk SSSR
       Ser.Fiz. **40,** 2543 (1976).

[81]   S. N. Morozov, D. D. Gurich, and T. U. Arifov, Izv.Akad.Nauk SSSR Ser.Fiz. 43, 137
       (1979).

[82]   S. S. Radzhabov and R. R. Rakhimov, Izv.Akad.Nauk SSSR Ser.Fiz. **49,** 1812 (1985).

[83]   A. J. Eccles, J. A. van den Berg, A. Brown, and C. Vickerman, Appl.Phys.Lett. **49,**
       188 (1986).

[84]   S. T. de Zwart, T. Fried, D. O. Boerma, R. Hoekstra, A. G. Drentje, and A. L. Boers,
       Surf.Sci. 177, L939 (1986).

[85]   D. H. Schneider, M. A. Briere, J. McDonald, and J. Biersack, Rad.Eff.Def.Solids 127,
       113 (1993).

[86]   D. C. Parks, M. P. Stöckli, E. W. Bell, L. P. Ratliff, R. W. Schmieder, F. G. Serpa, and J. D. Gillaspy, Nucl. Instrum. Meth. Phys. Res. B 134, 46 (1998).

[87]   D. H. Schneider and M. A. Briere, Physica Scripta 53, 228 (1996).

[88]   S. Della-Negra, J. Depauw, H. Joret, V. Le-Beyec, and E. A. Schweikert, Phys.Rev.Lett. 60, 948 (1988).

[89]   I. Bitenskii, E. Parilis, S. Della-Negra, and Y. LeBeyec, Nucl. Instrum. Meth. Phys. Res. B 72, 380 (1992).

[90]   N. Kakutani, T. Azuma, Y. Yamazaki, K. Komaki, and K. Kuroki, Jap. J. Appl. Phys. 34, 580 (1995).

[91]   K. Mochiji, N. Itabashi, S. Yamamoto, I. Ichiai, and K. Okuno, Jap. J. Appl. Phys. 33, 7108 (1994).

[92]   T. Schenkel, M. A. Briere, H. Schmidt-Böcking, K. Bethge, and D. H. Schneider, Phys. Rev. Lett. 78, 2481 (1997).

[93]   T. Neidhart, Z. Toth, M. Hochhold, M. Schmid, and P. Varga, Nucl.Instrum.Meth.Phys.Res.B 90, 496 (1994).

[94]   G. Hayderer, M. Schmid, P. Varga, HP. Winter, and F. Aumayr, Rev.Sci.Instrum. 70, 3696 (1999).

[95]   G. Hayderer, S. Cernusca, M. Schmid, P. Varga, H. Winter, F. Aumayr, D. Niemann, V. Hoffmann, N. Stolterfoht, C. Lemell, L. Wirtz, and J. Burgdörfer, Phys.Rev.Lett. 86, 3530 (2001).

[96]   P. Varga, T. Neidhart, M. Sporn, G. Libiseller, M. Schmid, F. Aumayr, and HP. Winter, Physica Scripta T73, 307 (1997).

[97]   G. Hayderer, S. Cernusca, V. Hoffmann, D. Niemann, N. Stolterfoht, M. Schmid, P. Varga, H. Winter, and F. Aumayr, Nucl. Instrum. Meth. Phys. Res. B 182, 143 (2001).

[98]   I. C. Gebeshuber, S. Cernusca, F. Aumayr, and HP. Winter, Nucl.Instrum.Meth.B 205, 751 (2003).

[99] UHV-AFM/STM, in *O MICRON Nanotechnology GmbH,* Germany.

[100]   J. Tersoff and D. R. Hamann, Phys.Rev.Lett. 50, 1998 (1983).

[101]   M. Szymonski, J. Kolodziej, B. Such, P. Piatkowski, P. Struski, P. Czuba, and F. Krok, Progress in Surface Science 67, 123 (2001).

[102]   M. Sporn, G. Libiseller, T. Neidhart, M. Schmid, F. Aumayr, HP. Winter, P. Varga, M. Grether, and N. Stolterfoht, Phys.Rev.Lett. 79, 945 (1997).

[103]   A. Audouard, R. Mamy, M. Toulemonde, G. Szenes, and L. Thome, Nucl. Inst. Meth. Phys. Res. B 146, 217 (1998).

[104]   A. Audouard, R. Mamy, M. Toulemonde, G. Szenes, and L. Thome, Europhys. Lett. **40,** 527 (1997).

[105]   D. C. Parks, R. Bastasz, R. W. Schmieder, and M. Stoeckli, J. Vac. Sci. Technol. B 13, 941 (1995).

[106]   G. Hayderer, S. Cernusca, M. Schmid, P. Varga, H. Winter, and F. Aumayr, Physica Scripta T 92, 156 (2001).

[107]   R. Minniti, L. P. Ratliff, and J. D. Gillaspy, Physica Scripta T 92, 22 (2001).

[108]   L. Porte, C. H. de Villeneuve, and M. Phaner, J.Vac.Sci.Technol. B 9, 1064 (1991).

[109]   R. Coregater, A. Claverie, A. Chahboun, V. Landry, F. Ajustron, and J. Beauvillain, Surf.Sci. 262, 208 (1992).

[110]   H. X. You, N. M. D. Brown, and K. F. Al-Assadi, Surf. Sci. 279, 189 (1992).

[111]   K. Mochiji, S. Yamamoto, H. Shimizu, S. Ohtani, T. Seguchi, and N. Kobayashi, J.Appl.Phys. 82, 6037 (1997).

[112]   K. P. Reimann, W. Boise, U. Geyer, and K. P. Lieb, Europhys. Lett. **30,** 463 (1995).

[113]   S. Habenicht, W. Boise, H. Feldermann, U. Geyer, H. Hofsäss, K. P. Lieb, and F. Roccaforte, Europhys. Lett. 50, 209 (2000).

[l 14]   R. Hahn, K. Kang, S. Song, and J. Jeon, Phys. Rev. B 53, 1725 (1996).

[115]   R. Hahn and K. Kang, Phys. Rev. B 60, 6007 (1999).

[l 16]   A. V. Krasheninnikov and F. Eisin, Surf. Sci. **454-456,** 519 (2000).

Danksagung

An dieser Stelle möchte ich mich herzlich bei Herrn Prof. Dr. F. Aumayr für die ausgezeichnete wissenschaftliche und fachliche Betreuung meiner Arbeit bedanken. Durch das ausgezeichnete Arbeitsklima und die inspirierenden Diskussionen war es leicht, auch schwierige technische Probleme zu lösen. Außerdem war es mir möglich, durch die Teilnahme an internationalen Konferenzen und Kooperationen meinen physikalischen Horizont stark zu erweitern.

Auch dem Institutsvorstand Herrn Prof. Dr. HP. Winter möchte ich für die Unterstützung und reges Interesse an meinen Messungen danken.

Für die gute Zusammenarbeit am AFM/STM danke ich Frau Dr. I. Gebeshuber.

Natürlich bedanke ich mich auch bei Herrn DI J. Stöckl sowie Herrn DI E. Galutschek für die freundschaftliche Hilfe im Laboralltag.

Meinen Eltern danke ich, dass Sie mich zu jeder Zeit moralisch und auch finanziell bei meinem Studium unterstützt haben.

Meiner Freundin B. Bodner danke ich für die Bereitschaft, mich durch mein Studium in Wien zu begleiten und für ihren Rat bei Textverarbeitungsfragen.

Lebenslauf

Geboren am 12.01.1972 in Innsbruck, Tirol

ledig

Ausbildung:

Sept. 1978 – Juni 1982:	Volksschule Innsbruck-Allerheiligen
Sept. 1982 – Juni 1986:	Bundesgymnasium und Bundesrealgymnasium, Innsbruck
Sept. 1986 – Juni 1991:	Höhere Technische Bundes-Lehr- und Versuchsanstallt, Fachrichtung Elektrotechnik, Innsbruck
Okt. 1991 – März 1992:	Grundwehrdienst im österr. Bundesheer
Okt. 1992 - Mai 2000:	Studium der Technischen Physik an der TU-Wien
Mai 2003 - Juni 2003	Doktorratsstudium an der TU-Wien